43453

NAME OF AUTHOR/NOM DE L'AUTEUR _____ BOIS KOUTSI

TITLE OF THESIS/TITRE DE LA THÈSE _____ SCATTERED RADIATION FROM BEAM MODIFYING

DEVICES USED WITH MEGAVOLTAGE THERAPY

BEAMS

UNIVERSITY/UNIVERSITÉ _____ University of Alberta

DEGREE FOR WHICH THESIS WAS PRESENTED/
GRADE POUR LEQUEL CETTE THÈSE FUT PRÉSENTÉE _____ M. Sc

YEAR THIS DEGREE CONFERRED/ANNÉE D'OBTENTION DE CE GRADE _____ Fall, 1979

NAME OF SUPERVISOR/NOM DU DIRECTEUR DE THÈSE _____ Dr J W Scrimger

Permission is hereby granted to the NATIONAL LIBRARY OF CANADA to microfilm this thesis and to lend or sell copies of the film.

The author reserves other publication rights, and neither the thesis nor extensive extracts from it may be printed or otherwise reproduced without the author's written permission.

L'autorisation est, par la présente, accordée à la BIBLIOTHÈQUE NATIONALE DU CANADA de microfilmer cette thèse et de prêter ou de vendre des exemplaires du film.

L'auteur se réserve les autres droits de publication; ni la thèse ni de longs extraits de celle-ci ne doivent être imprimés ou autrement reproduits sans l'autorisation écrite de l'auteur.

DATED/DATÉ _____ April 27th 1979 _____ SIGNED/SIGNÉ _____

PERMANENT ADDRESS/RÉSIDENCE FIXE _____ Glenora 17, Kypseli

Athens (811)

Greece

NOTICE

AVIS

The quality of this microfiche is heavily dependent upon the quality of the original thesis submitted for microfilming. Every effort has been made to ensure the highest quality of reproduction possible

If pages are missing, contact the university which granted the degree

Some pages may have indistinct print especially if the original pages were typed with a poor typewriter ribbon or if the university sent us a poor photocopy

Previously copyrighted materials (journal articles, published tests, etc) are not filmed

Reproduction in full or in part of this film is governed by the Canadian Copyright Act. R S C 1970 c C-30 Please read the authorization forms which accompany this thesis

La qualité de cette microfiche dépend grandement de la qualité de la thèse soumise au microfilmage. Nous avons tout fait pour assurer une qualité supérieure de reproduction

S'il manque des pages, veuillez communiquer avec l'université qui a conféré le grade

La qualité d'impression de certaines pages peut laisser à désirer, surtout si les pages originales ont été dactylographiées à l'aide d'un ruban usé ou si l'université nous a fait parvenir une photocopie de mauvaise qualité

Les documents qui font déjà l'objet d'un droit d'auteur (articles de revue, examens publiés, etc) ne sont pas microfilmés

La reproduction, même partielle, de ce microfilm est soumise à la Loi canadienne sur le droit d'auteur, SRC 1970, c C-30 Veuillez prendre connaissance des formules d'autorisation qui accompagnent cette thèse

THIS DISSERTATION
HAS BEEN MICROFILMED
EXACTLY AS RECEIVED

LA THÈSE A ÉTÉ
MICROFILMÉE TELLE QUE
NOUS L'AVONS REÇUE

THE UNIVERSITY OF ALBERTA

SCATTERED RADIATION FROM BEAM MODIFYING DEVICES

USED WITH MEGAVOLTAGE THERAPY BEAMS

BY

© ZOI KOLITSI

A THESIS

SUBMITTED TO THE FACULTY OF GRADUATE STUDIES AND RESEARCH

IN PARTIAL FULFILLMENT OF THE REQUIREMENTS FOR THE DEGREE

OF MASTER OF SCIENCE

IN

DEPARTMENT OF PHYSICS

EDMONTON, ALBERTA

FALL, 1979

THE UNIVERSITY OF ALBERTA

FACULTY OF GRADUATE STUDIES AND RESEARCH

The undersigned certify that they have read, and recommend to the Faculty of Graduate Studies and Research, for acceptance, a thesis entitled. .SCATTERED. RADIATION. FROM. BEAM. . . MODIFYING. DEVICES. USED. WITH. MEGAVOLTAGE. THERAPY. BEAMS. . . . .

submitted by . . . . . . ZOI KOLITSI . . . .

in partial fulfilment of the requirements for the degree of

Master of Science.

. . . .
Supervisor

. . . .

. . . .

. . . .

Date . . April. 24,. 1979

ΑΦΙΕΡΩΜΕΝΗ ΣΤΟΝ ΠΑΤΕΡΑ ΚΑΙ ΣΤΗΝ ΜΗΤΕΡΑ

ΓΙΑ ΤΗΝ ΑΣΤΕΙΡΕΥΤΗ ΑΓΑΠΗ ΤΟΥΣ

iv

ABSTRACT

The magnitude and distribution of scattered radiation from megavoltage therapy beams were investigated. Specifically, scatterers were placed in the beam at variable distance from a tissue equivalent phantom and radiation was monitored in the vicinity of the field edges.

Experiments were performed using low and high atomic number scatterers and the distribution of the scattered radiation was obtained for a large number of experimental geometries. The effective energy of the scattered radiation was also determined by depth dose measurements in the phantom. This investigation was conducted using the beams from 8 MV and 6 MV linear accelerators and a Cobalt-60 unit.

The intensity distribution of scatter varied with the distance of the scatterer from the plane of measurement (retraction distance) and, to a lesser extent, with the atomic number of the scattering material. It was also found to be a sensitive function of the field size and the position of scattering slab within the beam relative to the field edge. The effective energy of the scattered radiation was found to depend on the energy spectrum of the beam.

AKNOWLEDGEMENTS

I would like to thank all the staff of the Medical Physics
Department at the W.W. Cross Cancer Institute for their great amount
of assistance during the course of this work. Especially, I would
like to thank my supervisor, Dr. J.W. Scrimger, for his excellent
guidance and for the many stimulating discussions which have been
a source of constant encouragement to me; also Dr. S.R. Usiskin and
R. Barnett for their help with many aspects of this work.

I wish to express my gratitude to Dr. R. Hooper for generously
donating his time and knowledge reading this thesis and for his
valuable suggestions.

I would also like to thank everyone involved in the final
preparation of this thesis, especially, Mr. Karl Leisner for his
graphic work and the photography and Mrs. Isabel Goodfellow for her
excellent job typing this text.

Finally I thank all the people I interacted with during my stay
in Edmonton; especially R. Bihari, N. Fanjoy, K. Pine and D. Short
for their friendship and constant support.

TABLE OF CONTENTS

x

LIST OF TABLES

LIST OF FIGURES

CHAPTER I

INTRODUCTION

It has been known since the early 1900's that ionizing radiation interacts with biological tissue to produce chemical changes, Briefly stated, ionizing radiation alters the molecular structure and, at the cellular level, can cause direct cell death, chromosomal mutations or impair DNA synthesis and the reproductive ability of the cell. Research following the development of improved x-ray tubes, capable of producing beams up to 300 kV, established the fact that ionizing radiation can be employed in the clinical management of cancer and initiated the field of Radiotherapy.

Radiotherapy involves the delivery of a precisely controlled and monitored dose of radiation to a well defined volume of tissue. It is evident that the successful treatment of cancer by radiation incorporates a skillful balance between the maximum probability of cure and the minimum probability of radiation induced complications. Clinical experience demonstrates that a very narrow margin, as low as $\pm 10\%$, exists between doses that completely destroy the tumor without excessively damaging intervening structures (Linac Code of Practice, 1975). Therefore a high degree of precision in the administration of the radiation dose is required and accurate knowledge of the radiation dose distribution must be obtained, prior to initiating treatments. This knowledge is based on physical information concerning the beam, including its absorption and

1

scattering characteristics in tissue.

Conventional external beam radiotherapy employs two types of radiation: photon beams and energetic electron beams. The photon beams are either Cesium-137 or Cobalt-60 gamma rays, or x-rays generated in x-ray tubes and high energy accelerators during the deceleration of energetic electrons on an x-ray target. The type and energy of radiation to be used depends on the location of the tumour within the patient and the absorption characteristics of the radiation beam.

Figure 1.1 illustrates central axis depth-dose distributions in water for photon beams at a variety of energies. The maximum relative ionization occurs at some depth below the surface, followed by a plateau over a range of a few millimeters and a slow fall-off region. The depth of maximum ionization increases with photon energy, while the dose to the surface is reduced. These properties of the photon beams are particularly important in radiotherapy. Higher energy photons facilitate the delivery of high dose to deep situated tumours with considerable sparing of superficial tissue. There is of course a limit to the energy that can be clinically used, determined by the magnitude of the exit dose which also increases with energy. Photon beams of energies up to 35 MV have found applications in Radiation Therapy.

Classification of x-ray beams in terms of energy is somewhat arbitrary. Superficial x-ray beams are produced in x-ray tubes at operating voltages of 60 kV to 130 kV. Orthovoltage beams are generated at voltage of 140kV to 400 kV (Stanton, 1969). Both
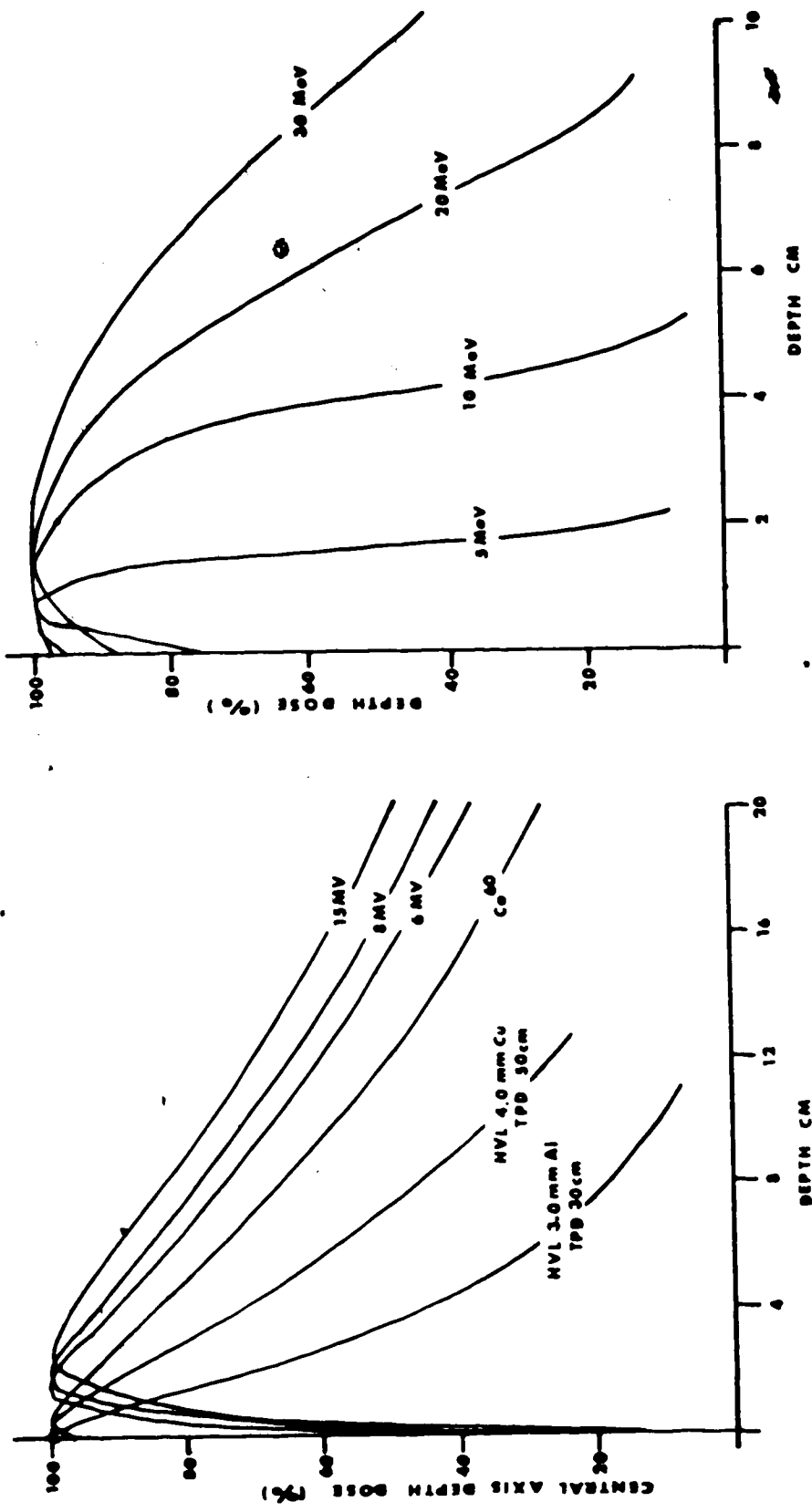
FIGURE 1.1. (a) Central axis depth-dose distributions for photons in water. (b) Penetration pattern of electrons in water.

(Brit. J. Radiol., suppl.11, 1972)

3

superficial and orthovoltage x-rays are used for the treatment of tumours located on the skin or at very shallow depths. Deeper tumours are treated using megavoltage (commonly referred to as supervoltage) beams at effective energies of around 1 MeV and above, including the Cesium-137 and Cobalt-60 gamma rays. Megavoltage radiations are furthermore classified in terms of their energies as follows:

- A low energy x-ray beam is defined to lie in the range of 2-6 MV. At a nominal energy of 2 MV the depth dose characteristics are similar to Cobalt-60 gamma rays, while a 6 MV beam produces a depth dose distribution with a depth of maximum absorbed dose of about 1.5 cm.

- Medium energy x-ray beams of energy 7-10 MV provide additional penetratability and flexibility in the choice of the technique to precisely irradiate tumours at any depth with large sparing of surrounding tissue.

- High energy x-ray beams are useful in cases where uniform depth distribution throughout a thick section of the body would be advantageous. About 25-30 MV is usually considered to be the maximum useful x-ray energy (U.S. HEW, 1976).

Electron beams, on the other hand, are useful in treating superficial tumours, while sparing the underlying tissue beyond their range. As seen in figure 1.1 electrons have a smaller penetration depth compared to photons of the same energy. This penetration depth increases with energy. Lower energy electrons deposit most of their energy in a well defined volume within their maximum range in the

absorber; at higher energies, their range is not well defined and the gradient of the dose-fall-off region is reduced. Electron applications in radiotherapy are quite specific and the useful energy is determined by the type of disease to be treated.

All teletherapy beams consist of an umbra, with uniform intensity distribution, a penumbra, where the primary radiation intensity falls rapidly from its value along the central beam axis to zero, and a region around the beam where only scattered radiation exists (figure 1.2). The presence of scattered radiation beyond the irradiated volume has been well established. In the case of photon beams this radiation arises during interactions of the primary beam with the target material and consists of energetic photons and electrons. Their ranges depend on the beam energy and can reach several centimeters in tissue. Scattered radiation is also generated in the collimator assembly and the intervening air space. The presence of scattered electrons in the beam is referred to as "electron contamination". These electrons, along with the low energy photons, deposit a considerable amount of their energy at the surface of the absorber causing an increase in the surface dose. From the radiotherapy standpoint, the implications involved are increased dose to the skin and to critical structures outside the treatment volume. The increased dose to radiosensitive organs, due to the radiation scattered outside the beam, may determine the outcome of the treatment, especially when large irradiation fields are required. Due to its clinical importance, the scattering properties of therapy beams have been the subject of recent research and a growing body of

target

collimators

TPD

penumbra

umbra

nominal
field size

PHANTOM
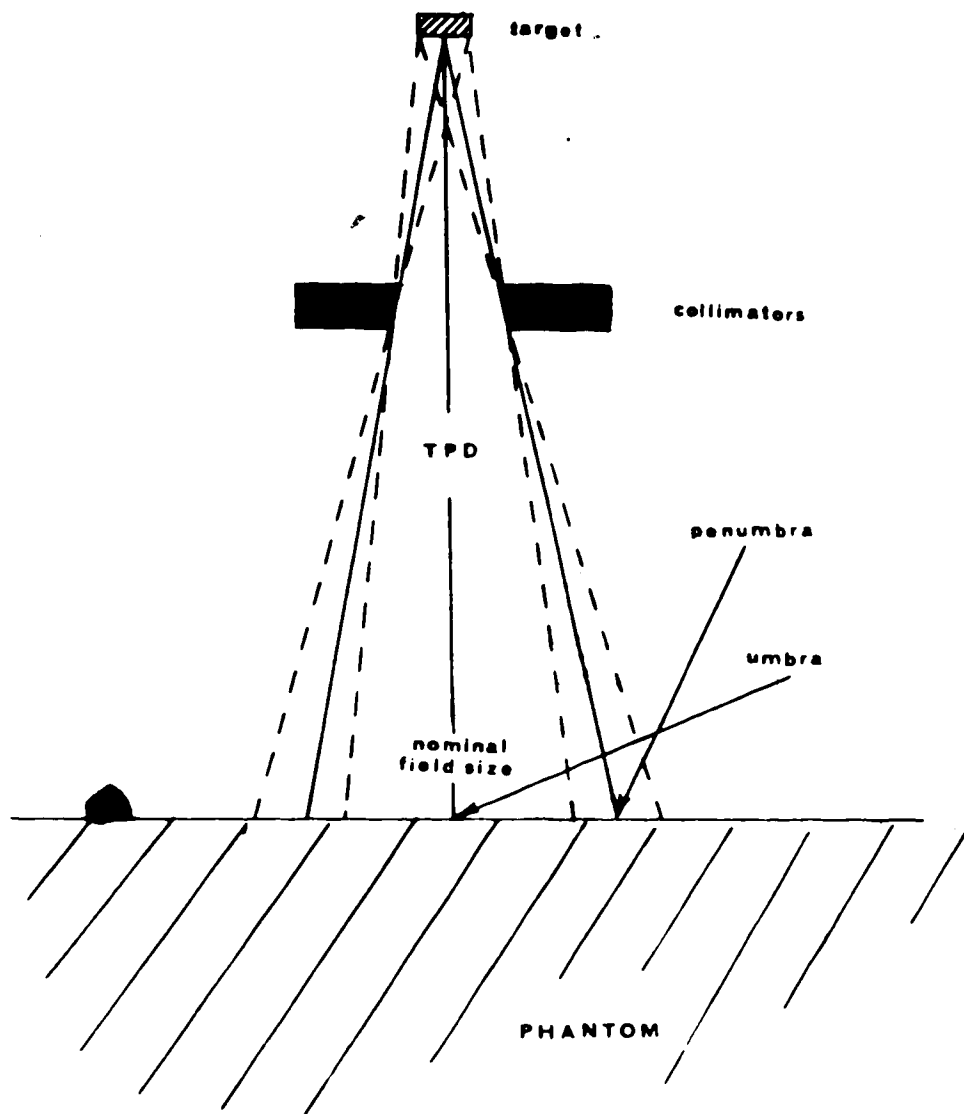
FIGURE 1.2.   Geometry of x-ray therapy beams.

literature. Scatter has been found to depend on the x-ray beam physical parameters as well as the design and construction of the treatment head of megavoltage equipment (Boland 1957; Keller 1974; Jackson 1971; .Richardson et al., 1954; Podgorsak et al., 1975; Rawlinson et al., 1973; Dutreix et al., 1965; Saylor et al., 1971).

In this project certain aspects of scattered radiation have been studied. Specifically, the nature and intensity distributions of scatter arising from beam modifying devices have been investigated. Beam modifying devices are specially designed filter introduced into the primary beam in order to produce more desirable d distributions within the irradiated volume.

In many cases in radiotherapy, the patient lies on the treatment couch with the tumour center located at the isocenter, a point fixed in space and defined by the orthogonal intersection of the central axis of the beam and the axis of rotation of the unit. Treatment is carried out for a set of fields directed through different angles. While the tumour lies within all fields, successively different sections of surrounding tissue are exposed to radiation. Isodose curves are plotted in order to provide information concerning the dose distribution within and in the vicinity of the irradiated volume, taking into consideration the effect of the combined beams, the presence of inhomogeneities in tissue, and the patient's contour. Figure 1.3 illustrates isodose distributions in tissue obtained from a Cobalt-60 beam and an 8 MV x-ray beam. The curves are plotted as a percentage of a reference value, which can be chosen to be the dose at the tumour depth or
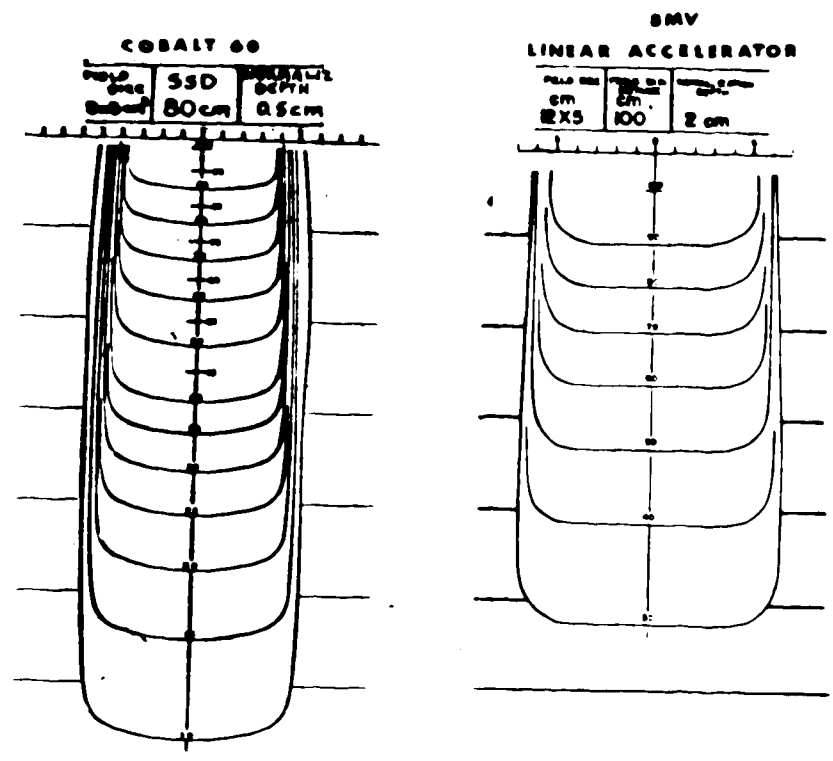
FIGURE 1.3. Isodose distributions in water for Cobalt-60
γ-rays and 8 MV x-rays.

that at any fixed point within the phantom. Figure 1.4 demonstrates how the patient's contour changes the isodose distributions for 6 MV x-rays. The isodose curves run parallel to the surface and the 100% contour occurs below the skin, closer to the surface. In this case, missing tissue is replaced by air, which has different attenuation characteristics. When homogeneous distributions are required, specially shaped filters are introduced into the beam, in order to compensate for missing tissue (tissue compensators). These are commonly, though not exclusively, constructed of low atomic number materials. Conversely, in some cases an uneven dose distribution, of the character shown in figure 1.4, is found more appropriate. Specially designed filters are then placed in the beam to produce any shape of isodose distribution desired. These devices are known as "wedge filters" and have found wide applications in megavoltage radiotherapy. Wedges are routinely made of high density materials and are placed in a recess provided within the treatment head. When radiosensitive organs are lying within the treatmenet field (e.g.lungs) isodose curves are modified by beam shaping devices in order to reduce the delivered dose around these structures. Such "shields" are customarily made of high Z materials. Finally when large fields are employed the surface dose increases, due to the larger amount of scattered radiation generated in the intervening air volume. Filters are in many cases placed in the beam, extending over the entire field in order to absorb scattered electrons before they reach the patient.

With the exception of wedge filters the above devices are

6 MV LINAC
F.S. 15x15 cm²
SSD 100 cm
norm. depth 1.5 cm
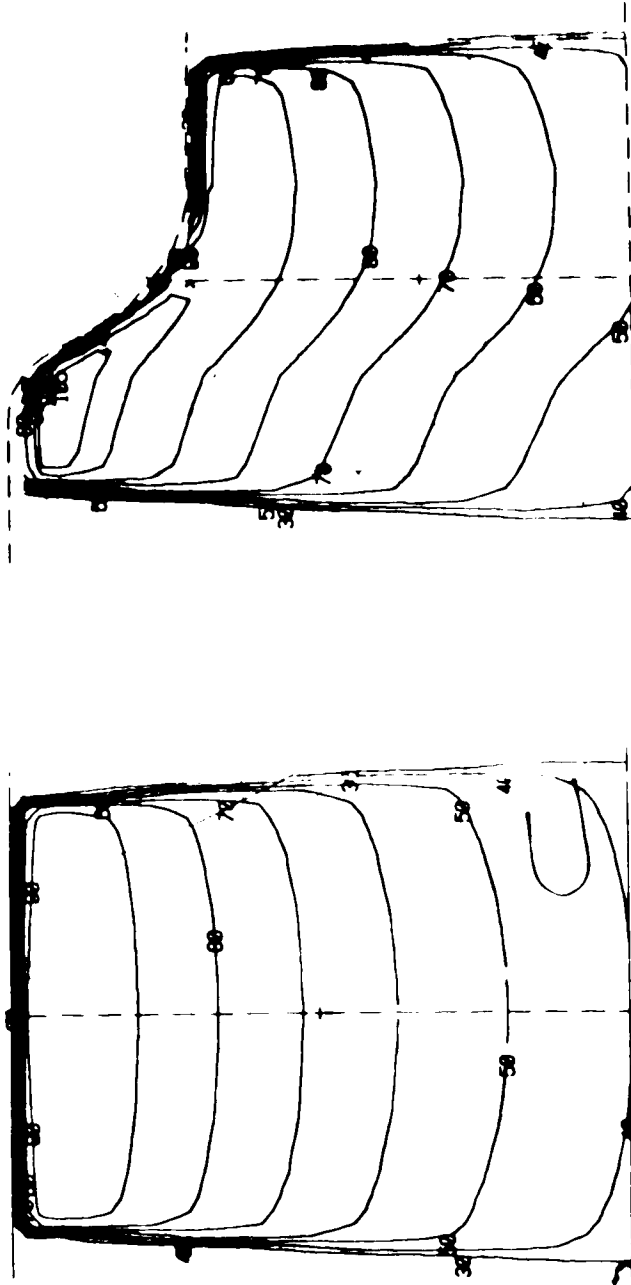
FIGURE 1.4. The effect of surface contours on isodose distributions.

placed outside the treatment head and at some distance from the patient. They then become sources of scattered radiation themselves, and if not properly constructed and positioned in the beam they give rise to an increase in the surface dose. This effect is minimized by the choice of a material and experimental arrangement which will yield minimum scatter intensity on the irradiated surface. However, the probability exists that radiation will be scattered at wide angles to the beam, to points outside the field, with a subsequent increase of the radiation intensity in this region. When radiosensitive superficial structures are lying within this area the use of such devices with therapy beams may become a cause for concern.

The object of this project was thus to investigate the behaviour of scattered radiation outside the field as a function of beam physical parameters. Experiments were carried out with three radiotherapy beams, in order to measure the scattered radiation beyond the field penumbra in the presence of scatterers within the beam. The nature of this radiation and its distribution were investigated for a number of scattering materials and experimental arrangements.

This study has been organized into both theoretical and experimental sections. The experimental section includes Chapters V and VI while the theoretical section is made up of Chapters I through IV.

The design and operation principles of the electron linear accelerator are described in Chapter II. Particular reference is made

to accelerators used for radiotherapy. Chapter III describes the processes by which x- ray and electron beams are attenuated and absorbed in extended media. Concluding the theoretical section Chapter IV describes radiation dosimetry. Ionization chambers and thermolumi-nescent dosimeters are treated to some detail.

CHAPTER TWO

THE MEDICAL LINEAR ACCELERATOR

2.1   OPERATION PRINCIPLES

In the linear accelerator, particles can be accelerated along

a straight path up to velocities close to the speed of light.   In

its most recent stage of development, the linac employs a corrugated

waveguide which constitutes the main accelerating structure. Accele-

ration of particles injected into the guide takes place by means of

an electric field associated with an electromagnetic wave which

oscillates at microwave frequen   . The field can be analysed into

travelling wave components, one of which will travel a·   · speed

as the particles to be accelerated. Particles with th   phase

will then "ride" on the wave and pick up energy continuous.   as if in

a constant field.   The phase velocity of the wave is arranged t vary

along the path and theoretically any amount of energy can be acquired.

The basic principle of operation is that electrons can generate

microwave power by exciting the properly designed microwave cavities

of klystons and magnetrons, and conversely, a sequence of cavities

can behave as an electron accelerating structure by transferring

energy from the cavity fields to the electron beam.   Electron bunches

travelling with the elctromagnetic field gain energy at a rate of

seve·· .. million electron-volts per meter of the structure length,

while the instantaneous potential difference between internal parts

of the accelerating tube does not exceed a few hundreds of volts and

the enclosure of the ·ructure remains at ground potential.

13

2.1.1 Microwave Cavities

The mechanism of generation of the microwave power and accelera-
tion of electrons involves the use of a hollow microwave cavity within
an electrical conductor. The concept of such a cavity is no different
from that of a lumped L-C circuit, which evolves into a microwave
cavity when requirements for very high resonant frequency are imposed.
In general, to increase the resonant frequency, both inductance and
capacitance have to be reduced. For frequencies in the microwave
region, the plates of the capacitor are drawn apart and then connected
by a number of inductances with reduced number of coils simulating
single straight wires. The circuit then resembles a conducting
cylindrical box, supporting current oscillations on its walls. Un-
like lumped constant circuits, a microwave cavity can resonate at a
number of frequencies, although the lowest one is usually employed in
the linac technology (Karzmark et al., 1973).

Introduction of microwave energy into the cavity excites electron
oscillations which in turn induce an electric field oscillating at
microwave frequencies. Electrons entering at the right phase of the
field at one end of the cavity can be accelerated towards the other.
Electrons injected at the decelerating phase of the electric field
however, are slowed down and deposit their kinetic energy in the
oscillating electromagnetic field of the cavity. These are the basic
ideas applied in the acceleration of particles in cavities and in the
generation of microwave power.

Theoretically, a microwave cavity constitutes an energy storing
system and no energy is radiated outside the structure. In practice
most of the input power is used to compensate for the resistive losses

at the cavity walls. Copper is usually used for cavity material, since its low resistance minimizes energy dissipation in the form of heat.

2.1.2 The Electromagnetic Field

For the cylindrical geometry of an electron linear accelerator, th useful field pattern is the transverse magnetic mode, usually des..ated by the symbol TM_{01}. The field consists of axial and radial electric fields and an azimuthial magnetic field component. The magnetic field runs in circles along the axis, being strongest at the cavity walls, while the electric field oscillates in a plane containing the axis and indpendent of the angle of rotation of the plane around this axis. The mathematical configuration of such a mode is a direct result of Maxwell's equations (Slater, 1948):

$$E_z = E \sin\omega(t - z/v_o) \, J_o(k_c r)$$

$$E_r = E \cos\omega(t - z/v_o) \left\{ \frac{[-iJ_1(k_c r)]}{(1-v_o^2/c^2)^{1/2}} \right\}$$

$$B = E \cos\omega(t - z/v_o) \left\{ \frac{v_o[-iJ_1(k_c r)]}{c^2(1-v_o^2/c^2)^{1/2}} \right\}$$

where : k_c is the wave number for which $k = \omega^2/c^2 - \omega^2/v_o^2$,

E is the axial field amplitude on the axis

ω is the angular frequency of the electromagnetic wave,

v_o is the velocity of propagation of the wave,

r is the radial distance from the axis and

z is the displacement along the axis

J_o, J_1 are Bessel functions with the following properties:

$$\text{for x small,} \quad J_o(x) \simeq 1 - x^2/4$$

$$J_1(x) \simeq x/2$$

$$\text{for } x = 2.405, J_o(x) = 0$$

$$J_1(x) = 0.519$$

In a resonant cavity of radius R the resonant frequency is determined by the condition that the electric field E_z is zero on the outer walls:

$$E_z = 0, \quad r = R \text{ and}$$

$$J_o(k_c r) = 0 \text{ or}$$

$$2\pi R/\lambda_o = 2.405$$

where λ_o is the wave length in free space.

2.1.3. Generation of Microwave Power

Klystrons usually operate as amplifiers driven by a low power oscillator. An elementary klystron employs a linear geometry of two cavities. An electron beam emitted from a cathode is accelerated by a DC potential. It then enters the first cavity (buncher), orting oscillations of a low power electromagnetic field. The electric field modulates the velocity of the electrons and bunches them, so they arrive at the second cavity as a sequence of bunches at microwave frequency. Electrons entering the buncher advanced in phase encounter the decelerating cycle of the electric field, are slowed down, and deposit their kinetic energy in it. Those arriving delayed are accelerated by picking up energy from the wave, while those arriving in the correct phase are transported by the wave without any velocity or phase change. As a result electron bunches are formed. No net

deposition of energy takes place in the first cavity, since electrons arrive at a constant rate at all times. The second cavity (catcher) is resonant at the same frequency as the buncher so that all bunches enter at the decelerating phase of the electric field and a large portion of their kinetic energy is converted into microwave power. For higher current bunching and amplification, klystrons incorporate additional cavities not resonant at the klystron operating frequency, so that they absorb no net power from the beam. Peak power as large as 25 MW can be obtained (Stanford research linac) with conversion efficiency of DC power to microwave power up to 55% (Karzmark et al., 1973). Klystrons usually operate at a frequency of 3,000 MHz in the microwave "S band", which for most conditions of linac operation has been proved to be the optimum frequency. All linacs in the radiation therapy field operate at or near this frequency.

Magnetrons commonly function as high power oscillators. They employ a cylindrical rather than linear geometry. Electrons are again accelerated from the cathode to the anode via a pulsed DC electric field (figure 2.1). Incorporated into the anode is a chain of resonant cavities arranged peripherally on the outer cylindrical wall, where electromagnetic oscillations are induced. In addition, a static magnetic field is applied along the axis of the cylindrical structure. The emitted electrons interact with the magentic field, the pulsed DC and the RF oscillating fields. They spiral towards the anode and convert up to 60% of their kinetic energy into microwave power, while at the same time they undergo velocity modulation. A typical S-band magnetron used in radiotherapy linacs operates at a 2 MW peak power and 2 kW average output.

Electric Field Lines

Cathode

Electron Trajectories

Anode

C

18
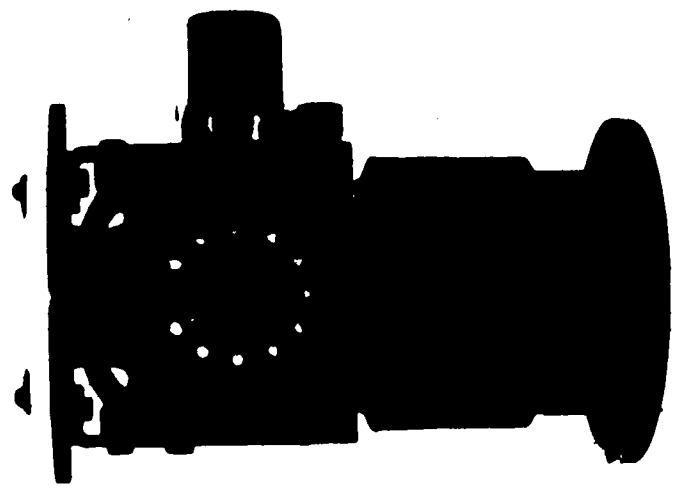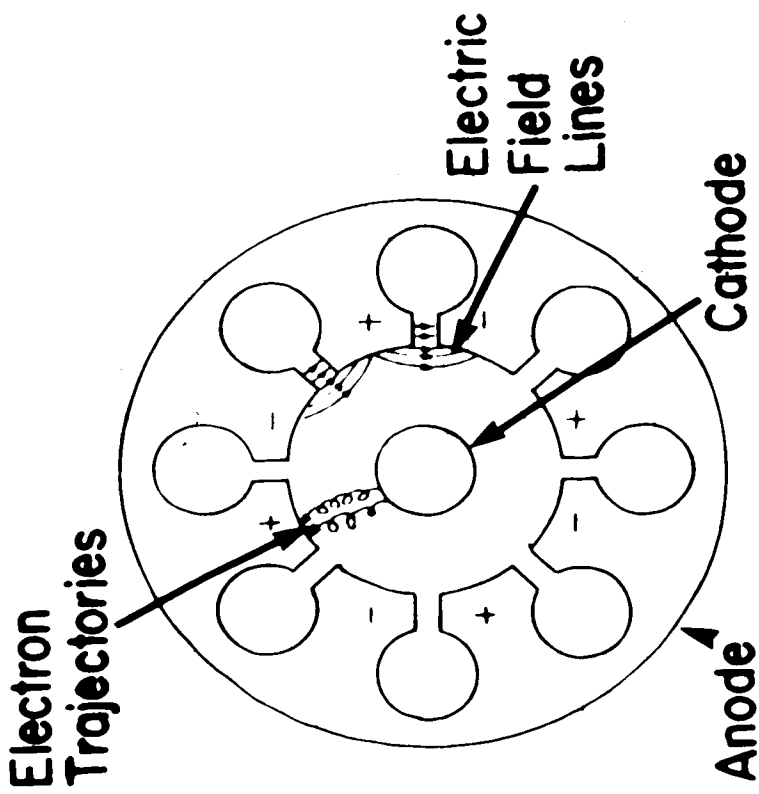
FIGURE 2.1. Cross-sectional drawing of a magnetron – the English Electric M 5010 magnetron

2.1.4. Propagation of Waves in Periodic Structures

It has been well established that a hollow pipe can act as a transmission line for alternating currents, i.e. a waveguide (Ramo, 1953). In the linear accelerator, electrons are accelerated in a "corrugated" waveguide supplied with RF power, which constitutes the accelerating structure. The demand for a corrugated rather than a smooth cylindrical waveguide is imposed by the requirement that the electromagnetic wave must propagate with a phase velocity lower than the speed of light, in order for the particles to keep in a fixed phase relationship with the wave and be accelerated by it.

Fourier analysis of the field equation as described by Floquet's theorem for periodic structures proves that the electromagnetic wave can be analyzed into n Fourier components, each representing a true travelling wave with angular frequency ω, wavelength $\lambda_n = 2\pi/k_n$ propagating along the axis with velocity v_n equal to ω/k_n (Slater, 1948):

$$E(z) = \sum_{n=-\infty}^{\infty} E \; \text{expi}(\omega t - k_n z)$$

where $k_n = k_o + (2\pi n/L)$ and represents displacement along the z axis corresponding to one period of the original electromagnetic wave.

Of all components, one is significant for the acceleration of the particle. It is the Fourier component which travels at the same speed as the particle to be accelerated and stays in phase with it. The particle can be considered to "ride" on this wave so that from the particle's standpoint, the resonating component behaves as a field independent of time. All other components will then travel

with velocities large with respect to the particle and appear to it as rapidly oscillating fields with alternatively accelerating and decelerating effect, producing no net acceleration. However, due to their finite amplitude, they store energy whose expenditure is useless for the acceleration. Therefore, the optimum excitation is the one for which the resonant component has a very large amplitude compared to the rest.

The object of the exercise is then to establish a measure of the velocity of the wave component resonant with the particle. It can be easily verified that the angular frequency ω is periodic with respect to k_o with period $2\pi/L$, as well as an even function of k_o over the whole range of k_n values. As a result, the plot of ω vs k_o will be a periodic curve around positive ω values as shown in figure 2.2, where $1/\lambda_o = \omega/2\pi c$, and $1/\lambda_g = k_o/2\pi$ have been plotted instead. Here $1/\lambda_o$ represents the inverse wavelength of the electromagnetic wave in free space, and $1/\lambda_g$ the inverse guide wavelength i.e. the wavelength propagated in the waveguide associated with the component $n=0$. This latter quantity cannot be uniquely defined, but is a periodic function of $1/\lambda_o$ with period equal to $(1/L)$.

The ratio of the phase velocity of the nth component to "c" is equal to:

$$v_n/c = \omega/k_n c = \omega/(k_o + \frac{2\pi n}{L})c = \frac{1/\lambda_o}{1/\lambda_g}$$

which is the slope of the radius vector out to a point of the curve. The magnitude of this slope as seen in figure 2.2 can have any value, positive or negative. Otherwise stated, there are components propagating to the right or to the left with phase velocities decreasing for higher
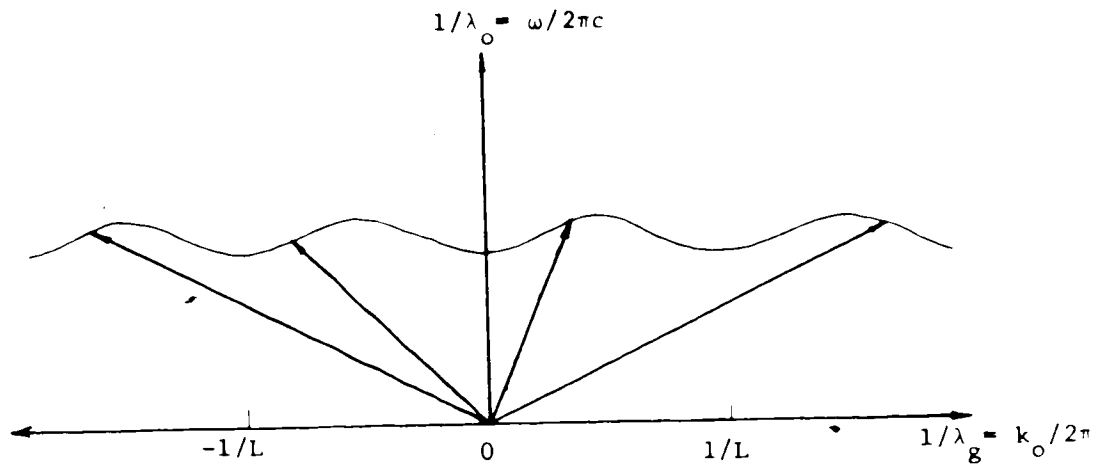
FIGURE 2.2. Frequency as a function of the reciprocal guide
wavelength for periodic structures.

values of n.

In a smooth cylindrical waveguide, resembling a single resonant cavity, the free space wavelength is related to the guide wavelength by the equation (Ramo, 1953):

$$1/\lambda_o^2 = 1/\lambda_g^2 + 1/\lambda_c^2$$

where λ_c is the guide cut-off wavelength. This value corresponds to the free space wavelength for which the guide wavelength becomes infinite and gives the minimum possible propagating frequency. The plot of this equation is shown in figure 2.3 along with the 45° lines corresponding to vectors of unity slopes indicating phase velocity equal to "c".

For λ_g approaching infinity,

$$\lambda_c = \lambda_o \text{ and}$$
$$k_c^2 = (\frac{2\pi}{\lambda_c})^2 = \omega^2/c^2 - \omega^2/v_o^2$$

Taking into account the boundary condition for a resonant cavity, $E_z = 0$ and the properties of the propagating mode:

$$kR = 2.405 \text{ for } F_z = 0$$

it follows that

$$v_o/c = \left[1 - (\frac{2.405c}{\omega R})^2\right]^{-\frac{1}{2}}$$

indicating that for $v_o < c$ no real propagation is possible. In this case there is no periodicity in the guide and a more sophisticated structure has to be introduced.

The situation, however, is different when disk-like irises are introduced into the initially smooth guide, with openings to allow for passage of the accelerated beam. This way separate cavities are formed and overlapping of the field into adjacent cavities through the iris holes provides the microwave power coupling, that is, allows the
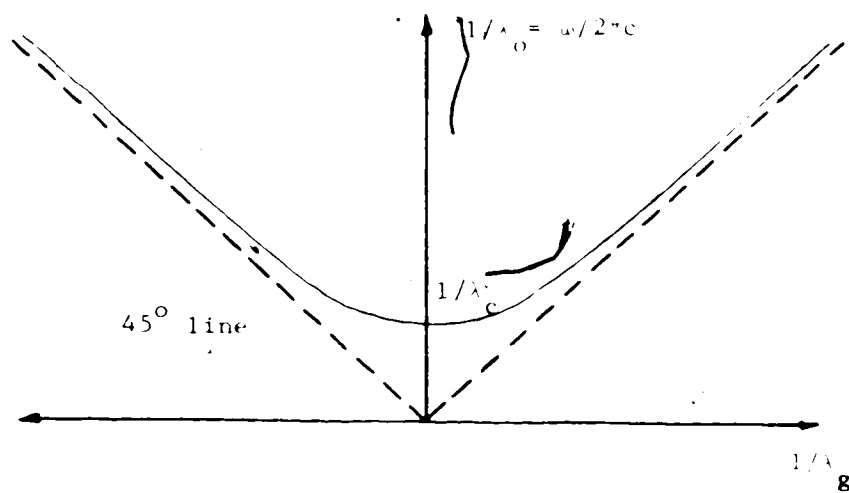
FIGURE 2.3. Reletionship between $1/\lambda_o$ vs $1/\lambda_g$ for an
unloaded waveguide.

power to flow from cavity to cavity. Such a structure is illustrated in figure 2.4.

In the case where the radius "a" of the iris aperture is large compared to the radial dimensions of the guide, (r - a) << R, the irises introduce small perturbations and the behavour of the iris loaded waveguide remains virtually unaltered. If the wavelength is long compared to the iris projection length into the guide, a very small fraction of the wave will be reflected and no appreciable change in the properties of the guide will occur. However, as the frequency is increased a larger fraction of the wave is reflected at each iris until eventually, a pure standing wave will be set up, and the wavelength will reduce to a value twice that of the iris spacing. In this case the phase velocity of the wave is zero. This is schematically shown in figure 2.5.a where as λ_g decreases, the curve deviates from the nonperiodic one of the smooth waveguide. Obviously, there are now frequencies between ω_1 and ω_2, such as ω_p , for which the phase velocity is less than "c". This curve is known as the dispersion curve.

The frequency has become again a periodic function of $1/\lambda_g$ with period equal to $1/2L$. In figure 2.5.b the lower curve corresponds to the Fourier component with n = 0. The rest of the curves arise from other values of n. For frequencies in the neighbourhood of multiples of $1/L$ the phase velocity is less than c. There are frequencies such as the ones in the band $\omega_2 - \omega_3$ whwre no real propagation mode
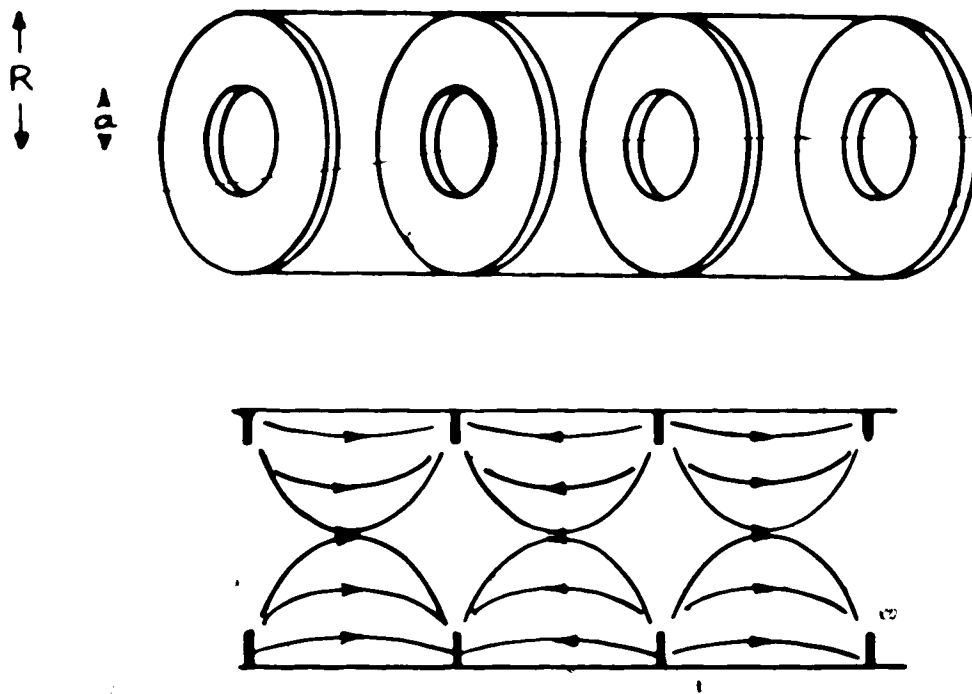
FIGURE 2.4. The iris loaded waveguide , used with travelling wave electron linacs and the electric field lines inside the structure.
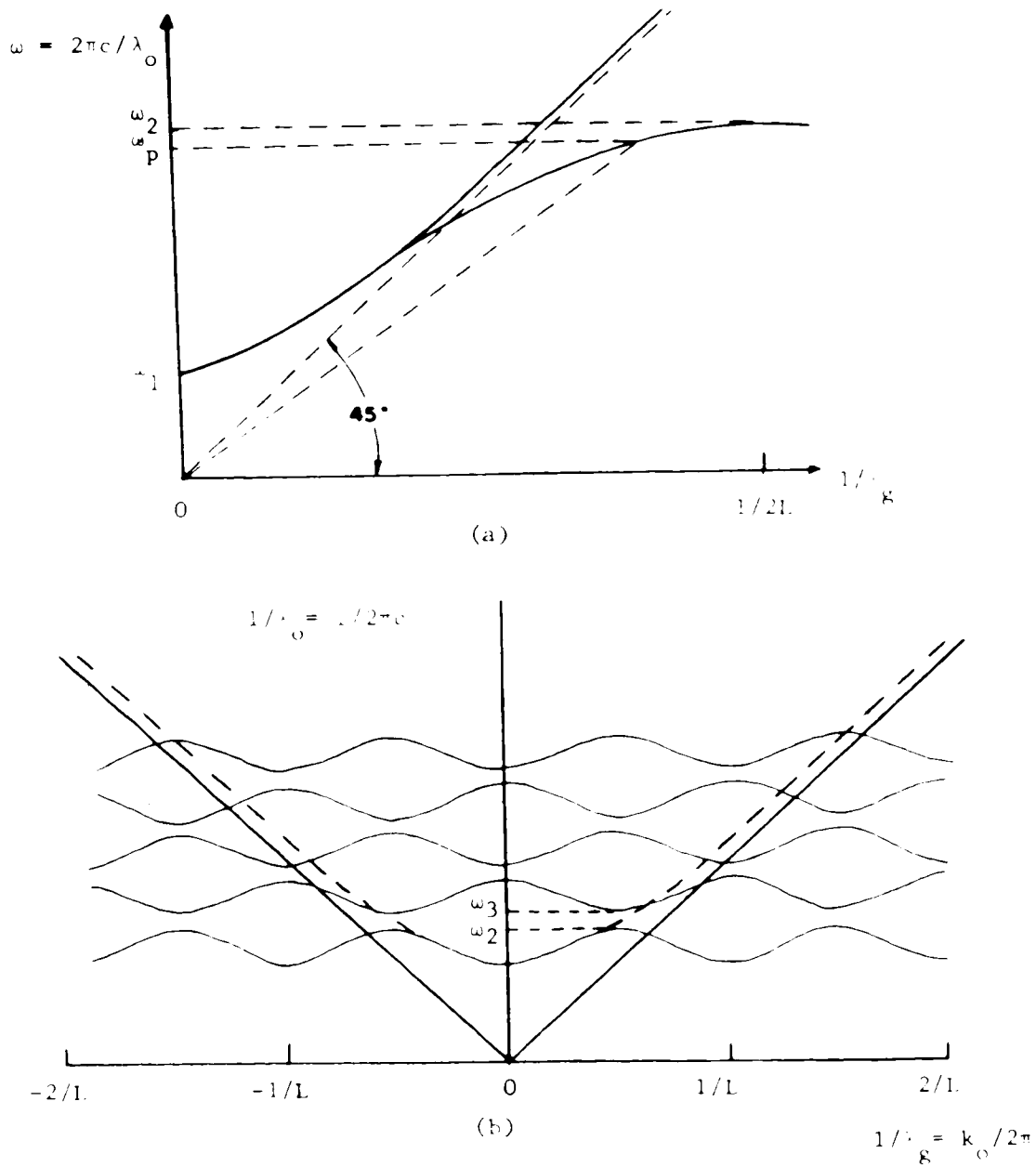
FIGURE 2.5.   (a) The dispersion curve for a uniform circular

waveguide (upper curve) and for the same guide

loaded with irises.   (b) The full dispersion curve.

exists. In other words the range of the frequencies is broken-up into pass-bands and the waveguide acts as a "frequency filter". It is also noted that for each frequency an infinite number of velocities can be propagated. In practice though, only the part of the curve n = 0 lying between 0 and 1/L is used, since the rest of the permissible branches correspond either to too small phase velocities or small impractical values of λ_g.

Further increase of the iris projection into the guide results in an increase of the scattering cross-section of the irises. The resonant Fourier component will increase in amplitude, but in addition other components of lower velocities will have considerable amplitudes with the disadvantage of absorbing useless power.

These considerations must be also taken into account in order to determine the optimum size and spacing of irises.

2.1.5 Dynamics of the Particle - Principle of Phase Stability

So far the mechanism of setting up the accelerating field with respect to the properties of the waveguide has been described. The mechanism involves construction of a periodic structure with the additional property of slowing down the wave to phase velocities smaller than the speed of light in free space.

The particle must remain   phase with the significant wave component in order for it to be accelerated. In addition, the properties of the field have to change along the path to accommodate the increasing velocity of the particle. Consequently, the process

of acceleration of the electrons to high energies is divided into
two stages that require different accelerator characteristics.
In the preliminary stage the velocity of particles increases to the
speed of light. They then enter the second phase of acceleration
in which the velocity remains constant and any increase in energy
can be considered as an increase in mass.

The study of the motion of the particles is based on the
principle of phase stability. It was formulated by Veskler in the
U.S.S.R. and independently by McMillan at the University of California,
and applies to all synchronous accelerators developed following the
war years. The principle of phase stability states the following:
In the phase-stable accelerator, particles will be accelerated by
an alternating electromagnetic field. The geometrical factors related
to the transmission line, the frequency and the strength of the
field can be adjusted in such a way that the particle will remain
in a fixed phase relationship to the wave during the acceleration
process. Particles with small errors in phase will still be
accelerated, performing small amplitude oscillations around an
equilibrium position (Livingston, 1952).

A mathematical formulation of the above principle is given in
the following paragraph. For simplicity, the velocity is considered
to be uniform during the motion. In this case the equation of motion
of the particle along the z axis can be derived as follows:

The only significant accelerating component of the electric
field is the axial one:

$$E_z = E \exp i\omega(t - z/v_o)$$

the sinosoidal form of which can be written as:

$$E_z = E \sin \omega (t - z/v_o)$$

The force exerted on the particle by the field is:

$$F = dp/dt = eE \sin \omega (t - z/v_o) \text{ and}$$

$$p = m_o v/(1 - v^2/c^2)^{1/2}, \quad v = dz/dt$$

where v_o is the phase velocity of the wave and p, v, m_o are the momentum, velocity and rest mass of the particle respectively.

A moving axis is then introduced, travelling with the wave at the velocity v_o. If z' is the displacement of the particle with respect to the new axis, then:

$$z' = z - v_o t$$

The total energy of the particle on the new axis is given by the Hamiltonian function, H, as follows

$$E = (m_o^2 c^4 + p^2 c^2)^{1/2} - pv_o$$

$$V = \oint F dz' = eE(v_o/\omega) \cos(\omega z'/v_o)$$

and

$$H = (m_o^2 c^4 + p^2 c^2)^{1/2} - pv_o - eE(v_o/\omega) \cos(\omega z'/v_o)$$

which satisfies the conditions:

$$\partial H/\partial p = dz'/dt \quad , \quad dp/dt = -\partial H/\partial z'$$

The Hamiltonion function expressed as above does not involve time explicitly, so it remains constant with time during the motion. The plot of momentum p versus displacement z' gives the energy contours for which H remains constant, and therefore the speed of the particle at any point of its path can be obtained.

The Hamiltonian can be expressed in the form:

$$H/m_o c^2 = \left[1 + (p/m_o c^2)\right]^{1/2} - pv_o/m_o c^2 - (eE/m_o c^2)\ (v_o/\omega)\cos(\omega z'/v_o)$$

where now the dimensionless parameter

$$(eE/m_o c^2)(v_o/\omega) = (eE/m_o c^2)(\lambda_g/2\pi)$$

describes the energy that the particle picks up, in $\tfrac{1}{2}\pi$ wavelengths, when subjected to maximum acceleration, divided by its rest energy.

In figure 2.6 the abcissa is the dimensionless quantity $\omega z'/v_o$, which is a periodic function of the wavelength with period 2π, and the ordinate is the dimensionless quantity $p/m_o c$. The energy contours are drawn for constant values of $H/m_o c^2$ and for $v_o = c/2$.

In the neighbourhood of the equilibrium position $z' = 0$, the potential energy $\dfrac{V}{m_o c^2} = -(eE/m_o c^2)(v_o/\omega)\cos(\omega z'/v_o)$ has a minimum value and the particle travels with velocity v_o, that of the wave. In this region the curves are closed periodic orbits. They represent points where the force on the particle is zero, and the particle remains in a fixed point with regard to the wave.

A particle which encouters the wave delayed in phase, that is $z' < 0$ but small, will come upon a higher potential in entry and will be speeded up to a velocity greater than v_o. Then it will advance with respect to the wave and enter the retarded phase too soon, so that it will be slowed down to a velocity less than v_o. Consequently, over the entire cycle of acceleration the particle will perform small amplitude oscillations around the equilibrium position $z' = 0$. Similarly a particle entering advanced in phase will be alternatively

decelerated and accelerated by the wave, oscillating about the equilibrium position. So, while the total energy remains constant, the particles traverse the closed curves in figure 2.6 in a clockwise direction.

As z' increases, the velocity of the particle becomes very different from that of the wave and for sufficiently high values of z', the particle, even though it experiences the effects of either the retarding or the accelerating phase of the wave, keeps advancing or slipping behind. Obviously, in this case there is no phase stability. Therefore, for each system there is an accepted range of values of entering phase. Particles falling into this range will be accelerated by the wave; those that do not will be lost in the accelerating cycle.

It is important to note that for phase stable oscillations, the equilibrium phase has to be located on the falling side of the accelerating wave. Particles entering the rising side of the wave, progressing ahead or lagging behind with respect to the equilibrium phase, will be never made resonant with the wave and eventually will be lost from the beam.

2.1.6 Longitudinal Motion of the Particle

The general treatment of the problem applies to the case where the particles are being accelerated up to the speed of light, so that the velocity of the wave will have to continually vary with the position of the particle. In practice this is done by having the cavity geometry change in the waveguide, in such a way that the whole
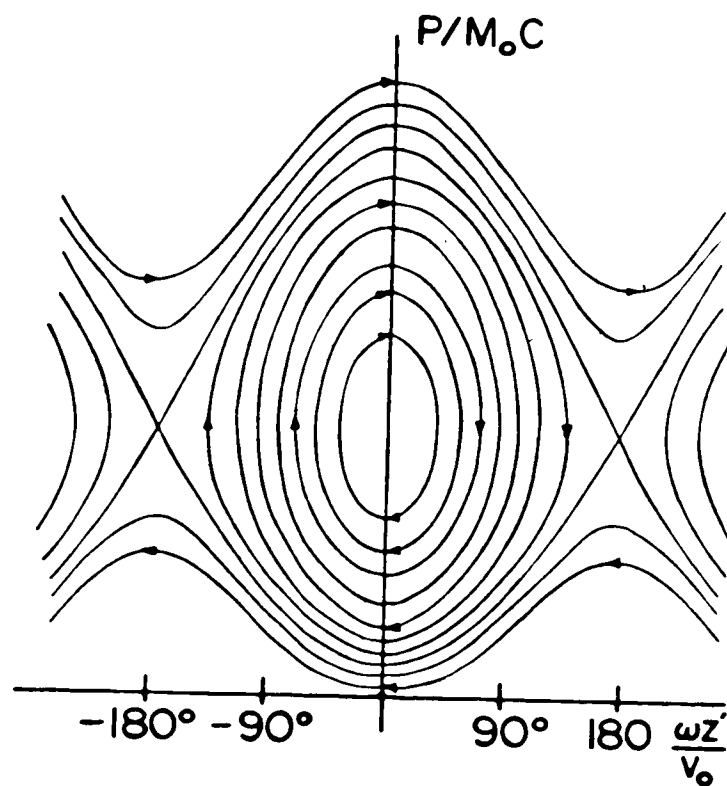
FIGURE 2.6. Momentum as a function of z´. Each curve
describes energy contours for H = constant
(Slater, 1948).

tube can be excited by a field of constant frequency.

The equations of motion of the equilibrium particle and the non-equilibrium one are derived in a similar way to the case of constant phase velocity, with the modification of expressing the velocity of the wave v_o as a function of position "z".

The field along the axis is:

$$E(z) = E\sin\omega\left[t - \int dz/v_o(z)\right]$$ where E is assumed to be independent of position.

If a moving axis at the velocity of the wave is introduced, so that z' is the displacement of the particle with respect to this axis, then $z_o'(t)$ is the position of the equilibrium particle and

$$Po(t) = m_o v_o/(1 - v_o^2/c^2)^{1/2}$$

is the momentum of the equilibrium particle.

The equation of motion of the particle can be written as: •

$$F_o = dp_o(t)/\delta t = eE\sin\omega\left[t - \int dz/v_o(z_o)\right]$$

To a good approximation the equilibrium particle always experiences a constant force, so the quantity $\left[t - \int dz/v_o(z_o)\right] = t_o$, where "$t_o$" is a constant. This last equation defines z_o in terms of time. The constant t_o can be calculated by computing the force necessary to produce the desirable acceleration:

$$F = eE\sin\omega t_o$$

Therefore the equation of motion of the equilibrium particle can be found as a function of time.

For the non equilibrium particle, $z = z' + z_o$, z' being the displacement from the equilibrium position and $v' = dz'/dt$ the rate of change of this displacement.

For z' very small, $v_o(z) = v_o(z_o)$ and

$$dp/dt = F = eE\sin\omega\left[t - \int dz/v_o(z_o)\right]$$

$$= eE\sin\omega \left[t - dz_o/v_o(z_o) - z'/v_o(z_o)\right]$$

$$= eE\sin\omega \left[t_o - z'/v_o(z)\right]$$

Also,

$$dp/dt = dp_o/dt + m\, dv'/dt + v'\, dm/dt = eE \sin \omega t_o + m\, dv'/dt$$

Here m is the relativistic mass of the particle. If only very short time intervals are considered, so that the relativistic mass does not change appeciably with time, the motion of the non-equilibrium particle is described by the equation:

$$m\, dv'/dt = eE \left[\sin\omega(t_o - z'v_o) - \sin \omega t_o\right]$$

The total energy of the system is given by the Hamiltonian

$$H' = p'^2/2m - eE(v_o/\omega)\cos \omega(t_o - z'/v_o) + eE_z\, z' \sin \omega t_o.$$

When v_o approaches c, any fairly large changes in energy will cause small variations in the velocity of the particle. With reference to the principle of phase stability, if the difference between the velocity of the particle upon entry and that of the wave is small, the period of oscillation of the particle around the equilibrium position approaches infinity. In this case the distinction is made among:

a) non-equilibrium particles with sufficiently high initial

momentum, which will be captured by the wave. At first they lag behind, then get into the accelerating cycle and start increasing in momentum. The particles will never be speeded up to the velocity of the wave, but remain at a fixed phase relationship to it and continue to acquire arbitrarily large amounts of energy, reaching asymtotically the speed of light.

b) particles with inadequate initial velocities to be bound to the field,which will soon be lost from the beam.

c) the equilibrium particles which will approach "c". For $v = c$ further increase in energy results in increase of mass.

In review, particles moving at velocities lower than c tend to form stable bunches around phase stable points in the field. They perform small amplitude oscillations about this position at a frequency which reduces to zero as the velocity of the wave and the particle approaches "c". Then the bunching phenomenon disappears; nevertheless bunches already formed at lower velocities persist as the particles are accelerated to the speed of light.

2.1.7   The Transverse Motion - Beam Instability

Associated with the transverse motion of the particle is the problem of beam instability and defocusing. In fact the phase stable positions described in terms of the longitudinal motion are inherently unstable with respect to transverse motion. This can be generally demonstrated, by noting that a Lorentz transformation transforms the equilibrium particle to rest while the non-

equilibrium particles perform oscillations about the equilibrium position. Then the only forces acting on the phase stable particle are those exerted by the electrostatic field, tending to drive it away from the axis, and a defocusing problem occurs.

However, at velocities comparable to the speed of light where stable bunches no longer exist, the transverse beam instability does not appear to be a problem. In the electron linear accelerator, only a small number of acceleration cycles in the buncher are required to bring the electrons to substantially the velocity of light and the problem is overcome by applying good focusing during this preliminary stage of acceleration.

2.1.8 Standing Wave Design

The iris loaded waveguide, as described, is employed by all conventional travelling wave linear accelerators. It is relatively easy to construct at comparatively cheap manufacturing costs and is commonly used in research electron linear accelerators. At the end of the cycle the remaining power is usually dissipated in a resistive load. Certain designs employ a high power directional coupler and phase shifter to recirculate the remaining power which however adds to construction costs and operational complexity.

Of increasing popularity is the standing wave accelerating structure, which underwent great developments during the 1960-70 decade. This system offers high efficiency, phase and amplitude stability, and is inherently insensitive to minor operational errors.

The first medical linac of this design to appear in the scene of clinical practice was the Varian Clinac 4, installed in 1968.

In the standing wave design the microwave power is coupled via side coupling cavities, located off the beam axis, to the sides of the accelerating structure, rather than through the iris aperture. The microwave power is reflected at both ends, so that a standing wave is set-up. The heart of the design is a side coupled guide which consists of a succession of resonant elements (cavities). Depending on the operation mode, these cavities can either be alternatively excited and unexcited ($\pi/2$ mode), or supporting oscillations of the electric field varying by a half period (π - mode). The resonantly coupled cavities are made to resonate at a single frequency, whereas the shape of each element varies to accommodate the desirable field pattern and retain a fixed frequency.

The conventional operating mode is the π - mode, where alternate cavities have the electric field directed in opposite directions at any instant in time, (figure 2.7.a). The shape and length of the cavities is such that the incident and the reflected waves are additive in each cavity, and a standing wave is set up.

The π - mode operation is by definition operation at the maxima and minima of the disperstion curve, where the group velocity is zero. The side coupling cavities support the field minima and are drawn off the axis to the side of the structure to reduce the accelerator length, while the field maxima in the accelerating cavities are located along the beam axis. The main disadvantage of this operating mode is the maximum sensitivity to frequency errors
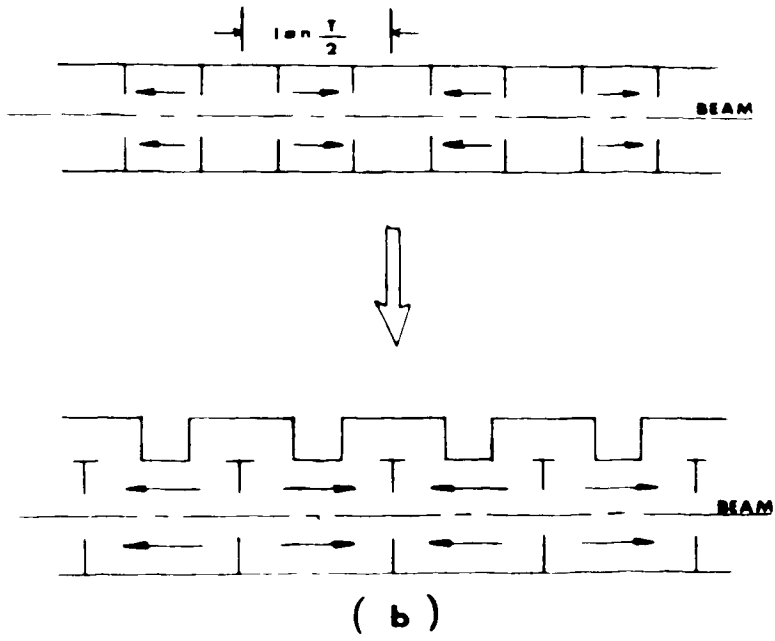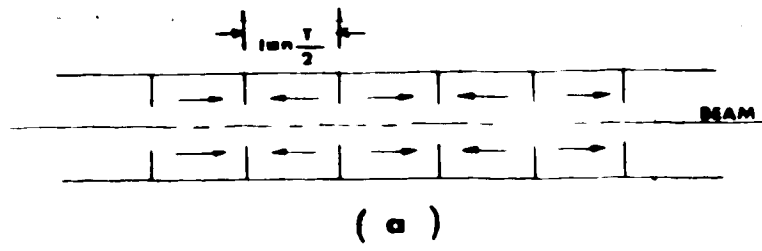
FIGURE 2.7. Illustration of incident and reflected E waves

(a) TM π-mode   (b)   TM $\pi/2$-mode.

which can result in phase shifts from cavity to cavity, other than
π/2 - mode. Here the geometry of the cavity array is different
from before and such as to provide high shunt impedance, although
operation under this mode is at maximum group velocity on the
dispersion curve. This is due to the properties of the π/2 - mode,
where in a chain of cavities resonant at identical frequencies,
every other cavity stores no energy except for that required to
overcome resistance losses and transmit power. These cavities serve
as the coupling (microwave transport) elements to the system.
Figure 2.7 (b) demonstrates the field pattern in three adjacent
cavities each providing a π/2 phase shift to the incident and
reflected waves. The coupling cavities do not contribute to the
acceleration and are moved off the axis to provide bimodal struc-
ture. Figure 2.8 illustrates a cross-section of the typical bimodal
standing wave structure.

Standing wave accelerator structures are designed to provide
reflections from both ends of the cavity array. No power is lost
through coupling to a resistive load and considerably less (less
than one half) microwave power is required to attain the same
electron energy of the conventional travelling wave unit of the
same length.

Associated with this design is its vulnerability to power
reflections back to the power supply resulting in detuning of the
source. The accelerator structure is adjusted during manufacturing
to a specific beam loading to absorb all reflected power. Never-
theless strong reflections are present during the exponential
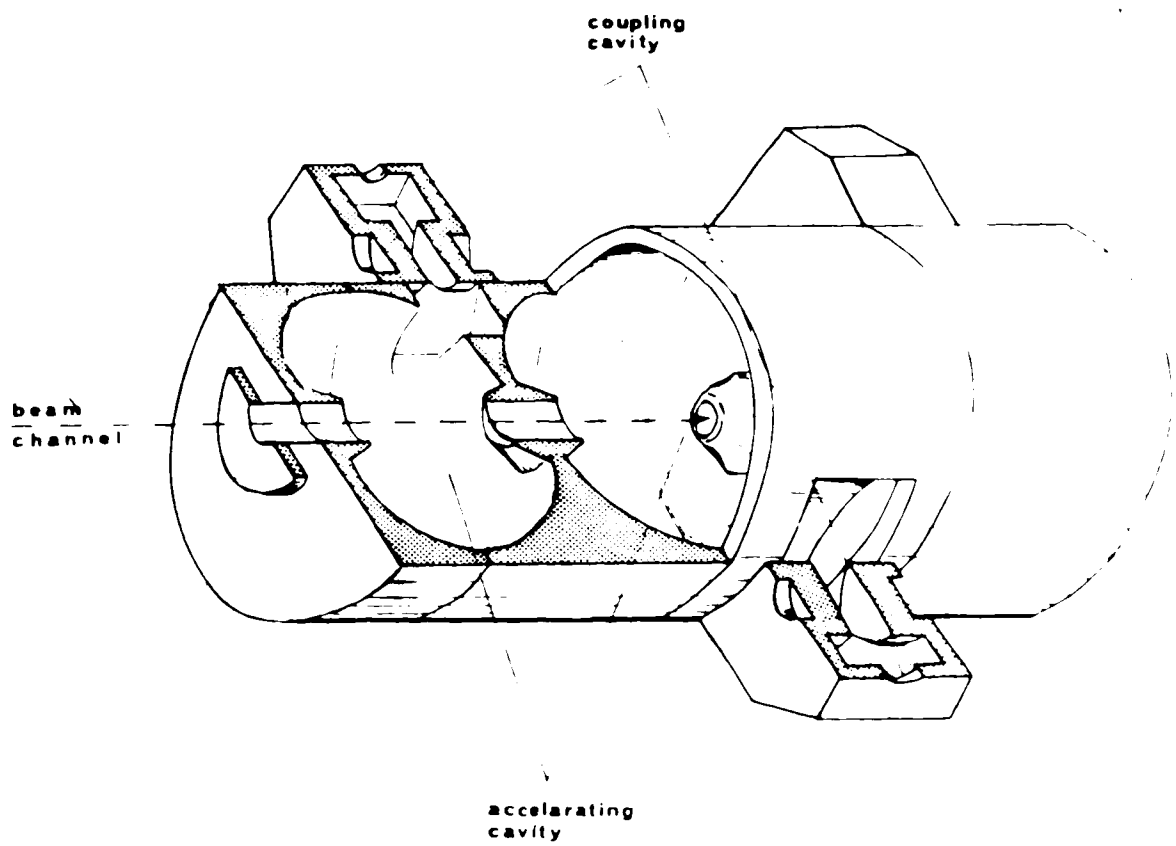
FIGURE 2.8. Cross-sectional drawing of a side coupled
accelerator structure (Karzmark, 1973).

build-up and fall-off of the field and installation of a circulator between the source and the structure is necessary, to absorb nearly all reflected power.

2.2   DESIGN AND CONSTRUCTION OF THE MEDICAL LINEAR ACCELERATOR.

The operation of the linear accelerator on a routine basis, in the hospital environment is more complicated than that in the laboratory. Here certain requirements are imposed, concerning the patient and personnel safety as well as the applicability of such a machine on a clinical basis.

The physical size of the medical linac can not exceed certain limits. Therefore a high power microwave source is required to compensate for the reduced waveguide length, or a high shunt impedance - high efficiency structure should be imployed. The fabrication cost of the medical linac is consequently higher.

All medical linacs are constructed with isocentric mounting (figure 2.9). This is an important feature, since isocentric techniques are employed in many radiotherapy cases. The gantry is capable of rotating through 360° about the isocenter, at a speed of at least one rotation per minute.

In order for the treatment procedure to be efficient, it is necessary that the medical linac operates at an output which should not fall below pre-set limits. Depending on their design and nominal energies, medical linacs deliver an output of anywhere between 200 rads/min to 1000 rads/min.
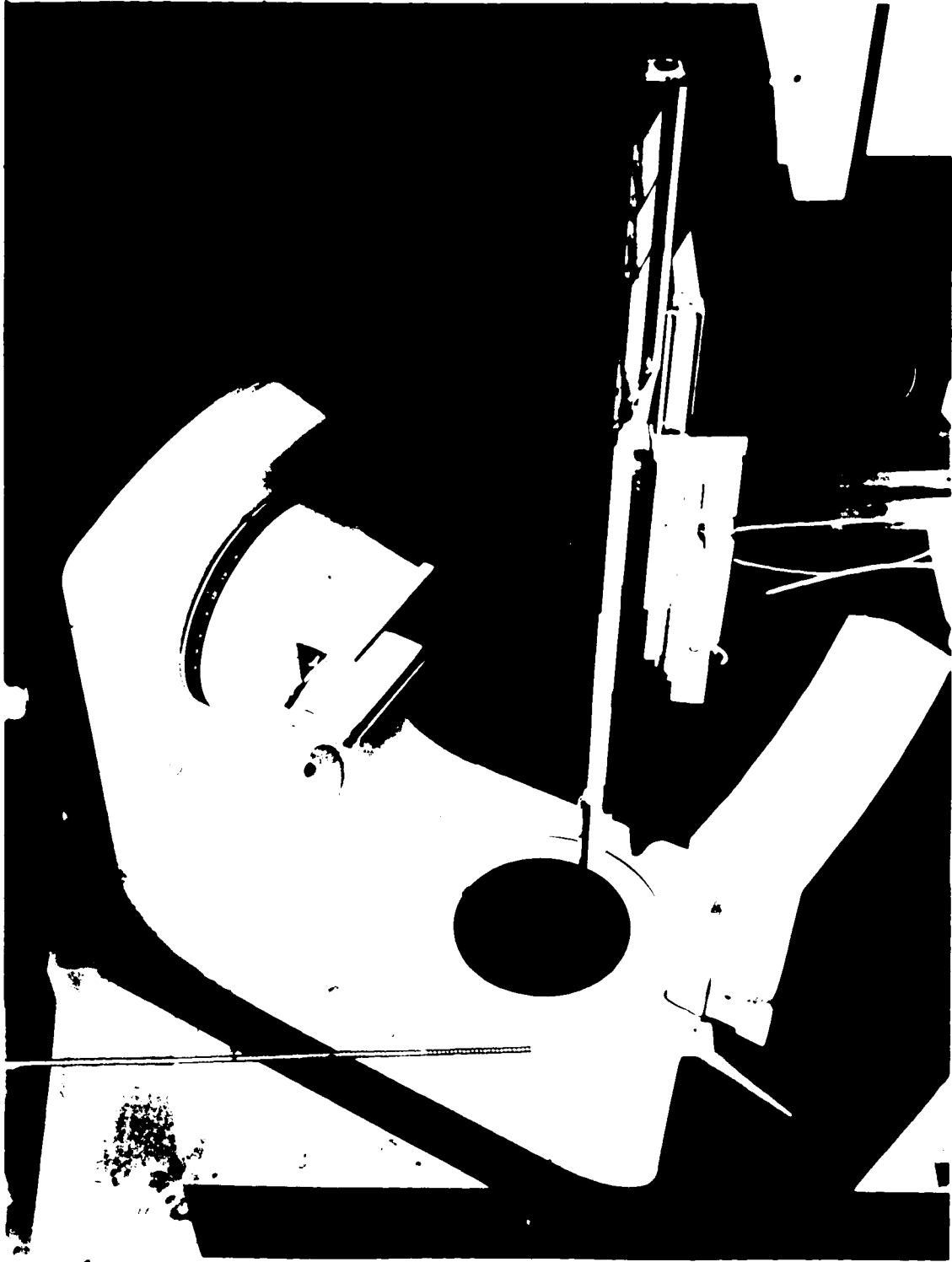
FIGURE 3.9. The SIEMENS 6 MV Linear Accelerator Unit (Mevatron 6) with the CRRH Head Phantom in position.

Considerations of the patient and personnel safety impose the demand for precise dose monitoring, stability and shielding. The treatment beam must have an homogeneous energy and intensity distribution throughout the treatment field and the dose should be delivered with a degree of accuracy no less than ·3% (Linac Code of Practice, 1975). Therefore the components of the treatment head and the beam shaping devices have to be carefully designed.

It is often desirable that the medical linac offer an electron therapy option. For this purpose the treatment head assembly is removed from the path of the electron beam, which is then either scanned or scattered in specially designed foils in order to obtain clinically useful field sizes

Finally, it is important that accelerator failures and "breakdown" time be minimized. For best maintenance and servicing the linac is regarded as a combination of separate subsystems, each of which has different operational tolerances. These subsystems are listed as follows:

(a) The Injector System (b) The R.F. System (c) The Vacuum System (d) The Beam Transport System and

(e) The Treatment Head Assembly.

2.2.1 The Injector System

In the injector, electrons liberated at low kinetic energies from the source (less than 100 keV) are bunched and accelerated to almost the speed of light, through a two stage process. The

components of the system are the electron gun, the pre-buncher, the buncher and the focusing coils. These are diagramatically shown in figure 2.10. The electron gun consists of the anode block and the cathode assembly, placed in line with the guide. A filament cathode is made of a pure metal (ie. tungsten or tantalum) and must be operated at high temperatures. Oxide coated cathodes are indirectly heated. They have a longer life but require a high vacuum for satisfactory operation. The anode-cathode dimensions of the gun and the cathode operating temperature are so chosen that the gun delivers constant current, independent of variations in the heater current. As a result, the final electron energy is not subjected to change due to the injected electron current variations.

The emitted electrons, focused by beam forming electrodes, are then guided into a resonant cavity, the prebuncher. Here they are pregrouped around the correct phase for them to be taken up by the wave and undergo acceleration. During the prebunching procedure the electrons experience a fairly weak RF field, obtained from the accelerator power supply. They are accelerated or decelerated depending on their entry velocity, then are allowed to drift over some distance in an evacuated envelope. The distance is so chosen that all electrons reach a particular velocity and therefore are bunched around the correct phase. The prebunching process is non-linear and incomplete.

The final stage of grouping takes place in the buncher, where electrons undergo bunching and acceleration simultaneously. The
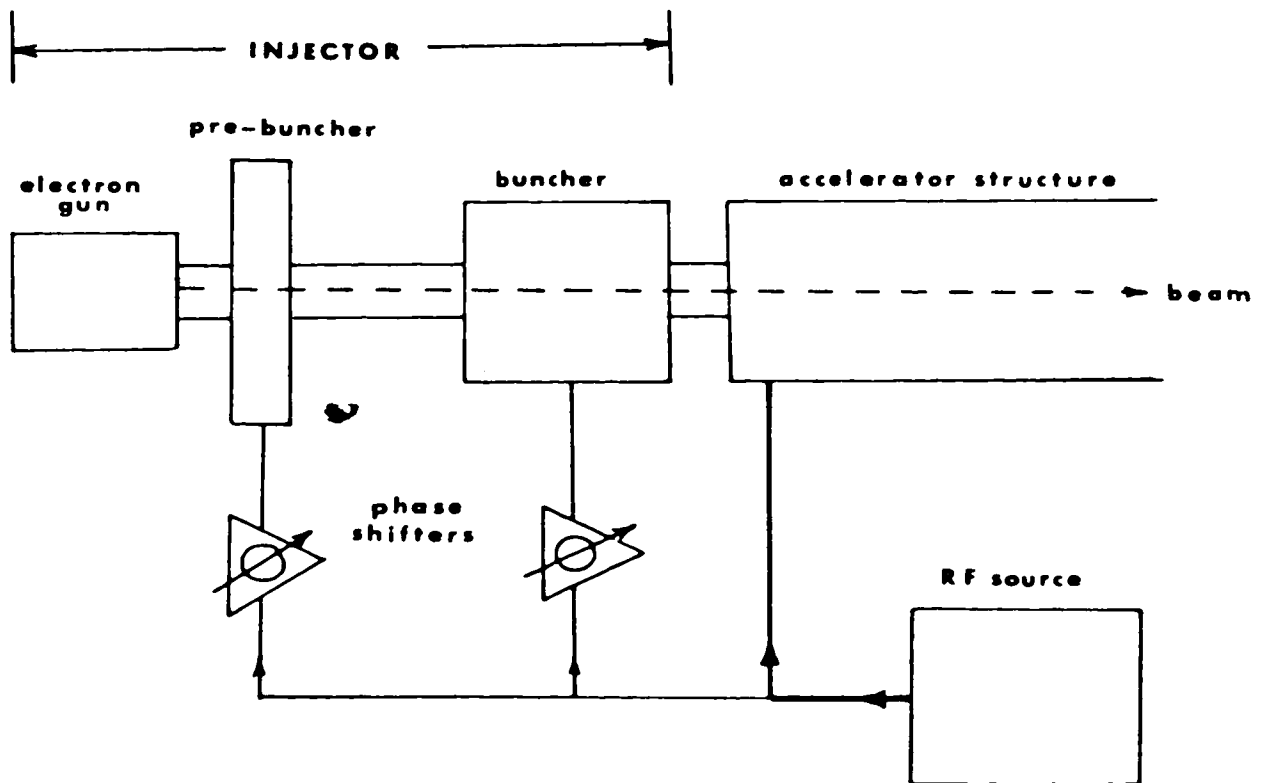
FIGURE 2.10. Block diagram of the components of the injector system.

buncher constitutes the first section of the waveguide and is especially constructed for this purpose. The characteristics of the wave, during this stage change continuously to match the increasing velocity of the particle. The electron beam is arranged to pass through focusing coils, to off-set the transverse motion defocusing at the phase stable positions. The beam then leaves the injector assembly to enter the main accelerator structure where the acceleration cycle is completed.

2.2.2 The Vacuum System

It is essential for proper operation of the linac that the entire path of the electrons is maintained at a high vacuum in order to avoid problems of electrical break-down in the waveguide and scattering of the beam by gas molecules. Typically a pressure lower than 10^{-7} Torr is maintained by means of an ion pump. Such a device consists of a number of anode plates and a titanium cathode, placed in a strong magnetic field. The electrons emitted when a suitable voltage is applied between the two electrodes follow a long spiral path in the presence of the magnetic field. Thus, they have a large probability of ionizing the intervening gas molecules. Ions so produced are accelerated towards the high potential cathode or the titanium surface with sufficient energies to embed themselves in it. For   pumping range of 10^{-7} Torr to below 10^{-10} Torr the pressure is   ortional to the number of collected ions, that is, the curr·   wing from the power pack.

No additonal monitoring is required.

2.2.3 The Radiofrequency System

This system comprises all low and high power components supplying the RF accelerating field, including the isolator and the automatic frequency control system. The RF power is supplied by a tunable magnetron or klystron operating at a peak pulse power in the range of 1 MW to 20 MW, and a radiofrequency of around 3000 MHz. The power is delivered in short pulses and the pulse repetition rate can be selected; for routine x-ray therapy it is usually in the region of 300 p.p.s. The power is fed from the magnetron to the waveguide via a radiofrequency transformer, so designed to ensure minimal power losses.

The isolator is a unidirectional attenuator, with minimal insertion loss properties in the forward direction and high attenuation efficiency in the reverse direction. As a result, power is allowed to flow into the waveguide, while reflected power to the source is absorbed in the isolator. This component is particularly important in the standing wave design where reflected, unabsorbed power would result in detuning of the power supply source.

Any change in the source operating frequency results in a variation of the phase velocity of the accelerating wave, with a subsequent variation in the final electron energy. Frequency changes as little as .25MHz can significantly alter the energy spectrum

of the beam. Such changes occur during the warming-up of the magnetron or klystron when the temperature distribution within the source body is not uniform. They are also found to occur when the gantry is rotated through large angles. It is evident that the injected radiofrequency must be kept within acceptable limits by means of a stabilizing system. An automatic frequency control system is a simple transmission cavity, receiving a monitor signal from the waveguide, and tuned to the correct frequency. An amplified difference signal between the cavity output and a reference voltage automatically correct the source frequency by setting a control motor in operation.

2.2.4 The Beam Transport System

The beam transport system can be divided into collinear and bent-beam designs. The former are found in low energy accelerators - some 4MV and 6MV - where the structure is small and the physical size of the machine is not a matter of concern. In collinear systems the electron beam, collimated to a cross-section of about 5mm., strikes a target placed along the beam axis. Any errors occurring during lateral displacements are compensated for by steering coils and therefore can be easily corrected.

In medium and high energy linacs the beam is carried to the target by a bent-beam transport system, which changes the flight path of the electrons by a nominal 90° or 270° deflection. The system incorporates one or more bending magnets and a number of focusing and steering elements. Such a design reduces the size of

the accelerator which increases with energy. In addition a 90° deflection system acts as an "energy-monitor"; should the energy exceed preset levels, the unbent high energy electrons will be lost from the beam. The first warning is a reduced output, followed by a vacuum deterioration.

In the 90° beam bending design, the electron beam, well focused and collimated, passes through a magnetic field to be deflected by approximately 90°. Higher energy electrons will follow a path of larger radius, thus deflected by a lesser amount, while the low energy particles will suffer a greater than 90° deflection. The cross-section of the bent-beam is again increased, so the beam is magnetically focused before it strikes the target. The 90° deflection system is capable of providing adequate focusing over a restricted range of energies. It is susceptible to energy changes in the beam, as well as variations of the BBM (bem bending magnet) current. Consequently, changes in the operating parameters of the linac, causing energy variations may result in large field asymetries. Field symmetry is defined by the difference between the average dose delivered to each section of the field, when it is disected by any straight line passing through the central axis of the beam. The clinically acceptable limits of field asymmetries have been set at ·3% of the dose at the central axis at a depth of 10 cm., and for all field sizes (ENVIRO-med, 1969). The traditional solution to the problem of field asymetries, associated with the 90° beam bending system has been to install stabilizing systems applied to the relevant parameters (ie., frequency and temperature).

Beam bending through 270° can be made insensitive to large variations of energy and the system is known as "achromatic". Achromatic deflection is based on the properties of a number of magnetic elements. In figure 2.11 (a) the beam passes through the uniform field of a specially shaped magnet. Electrons of differing energies follow a loop trajectory of varying radii, until they meet again at the focusing point. The "achromatic mirror" system (figure 2.11 (b) employs a non-uniform field between the shaped poles of the magnet. Again particles follow loop trajectories of varying radii. They enter the progressively increasing field, get deflected by 90° and leave it at the same point of entry, as if reflected by a magnetic mirror. The higher energy electrons do not suffer significant deflection initially, until they encounter the section of the strong magnetic field. Their path is so corrected, that they leave the magnet at the same points as the less energetic electrons.

Achromatic systems accept electrons of all energies within their design limits and deliver them to a small focal point onto the target. It appears that 270° bending is advantageous in ensuring good field symmetry. However the more flexible 90° bending design has proved sufficient when the stabilizing system, incorporated into the linac, allows only minimal perturbations.

2.2.5 The Treatment Head Assembly

The treatment head comprises the x-ray target, the beam
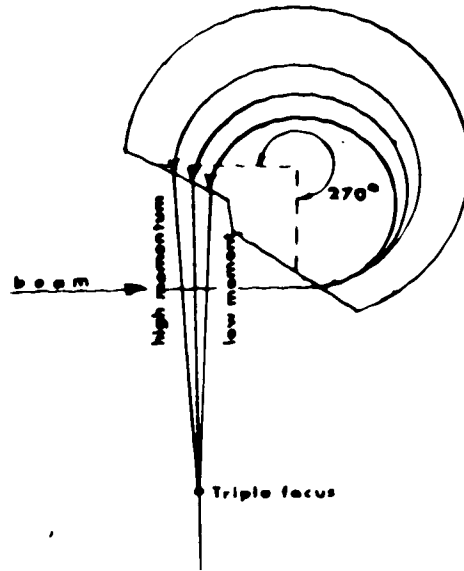
(a)
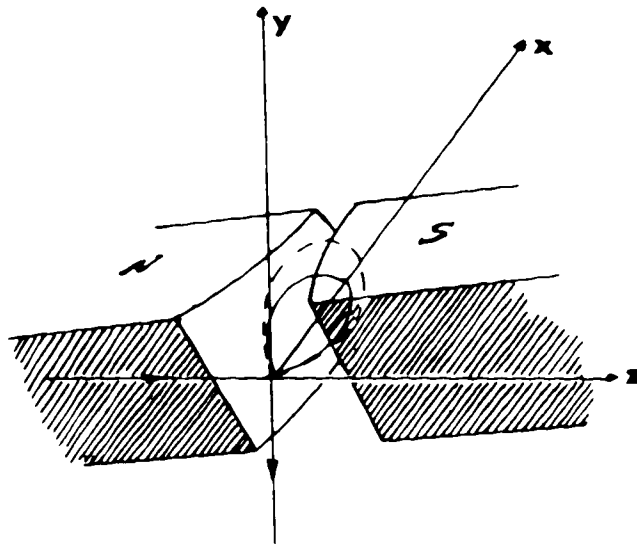
(b)

FIGURE 2.11. 270° deflection systems (a) Achromatic beam
transport system (b) the achromatic mirror.

flattening filter, dose monitoring probes and collimators
(figure 2.13).

A thick target is traditionally used for maximum absorption
of the incident electrons in order to avoid electron contamination
of the x-ray beam. The intensity and energy spectrum of
bremsstrahlung radiation, generated when electrons are stopped in
thick targets, is a function of electron energy, atomic number
of the target material and the angle of incidence of the electrons.
The most important processes involved in the production of
bremsstrahlung from thick targets are: (a) Radiation losses of
monoenergetic electrons, incident on thin targets; the thick
target sectrum can be assumed to be the summation of a series of
thin target spectra of varying incident electron energies (b)
Electron absorption, scattering and energy degradation (c)
Absorption of bremsstrahlung photons in the target. The
superposition of all processes results in a continuous x-ray
spectrum with all energies from zero to the maximum electron energy.
From the point of view of dose delivery and radiation shielding,
the behaviour of the beam is similar to that of a monoenergetic
photon beam of the effective energy characterizing its spectrum.

The x-ray beam intensity distribution on a plane, perpendicular
to the central axis is forward peaked and axially symmetrical. The
effect is more pronounced for higher electron energies. In
clinical practice a beam flattening filter is inserted into the
x-ray beam as shown in figure 2.12 and accurately aligned to the

electron
beam

target

primary
collimator

flattening
filter
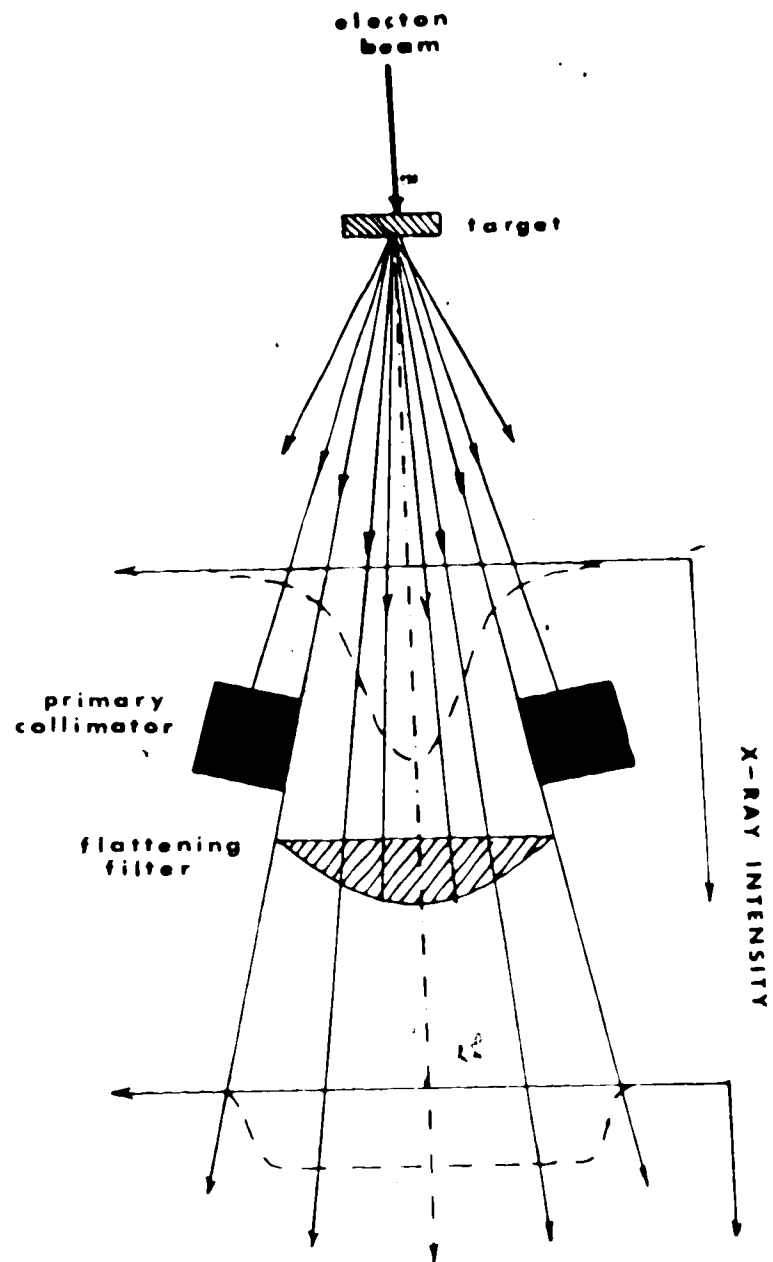
X-RAY INTENSITY

FIGURE 2.12. X-ray treatment beam production and flattening.

electron beam and the target, to compensate for the off-axis reduction of the beam intensity. The design of the filter is determined by examining the depth-dose data over the entire field, relative to the central beam axis. Optimum flatness can be achieved at any preset depth, usually 5 cm or 10 cm.

Both the target and the filter are fundamental components affecting the field symmetry, depth-dose characteristics and surface scatter of the beam. The thickness of the target as well as the composition of the target and the filter are parameters related to the effective energy of the spectrum and the x-ray yield in the forward direction. These two properties depend on the target thickness in such a way that when improving the x-ray yield, by increasing the thickness, the effective energy is reduced. The optimum compromise of target thickness is considered to be approximately equal to the mean electron range in the target material. Increasing the flattening filter thickness, generally reduces the spectral variations across the field, but it also reduces the output. The optimum thickness is therefore determined according to the type and output potential of the specific machine. Rawlinson and Johns (1973) found that the choice of the target material depends on the electron energy, while the low atomic number filters are favoured for all energies. Targets and filters used in high energy linacs (greater than 15 MV) should be both made from low atomic number materials, while for lower energies the most penetrating beam is produced the combination of high atomic

number target and low atomic number filter. Considering that
the cost of medical linacs increases with beam energy, it is
important to optimize the x-ray target and the beam flattening
filter.

The dose monitoring is accomplished by means of several
ionization chambers, or one multiple ionization chamber, intersecting
the path of the beam, before it reaches the collimators. The
plates are placed a few millimeters apart and are connected to a
high voltage power supply. The ions produced during interaction
of the x-ray beam in the air space are collected by the plates. The
rate of the chamber output is proportional to the delivered dose
rate.

The x-ray beam emerging from the target is initially collimated
by a primary collimator. Definition of the field is achieved by a
pair of collimators, capable of providing fields rectangular in
shape and continuously variable up to around (35×35) cm^2 at the
nominal source to the isocenter distance. It is important that the
collimator transmits minimal incident energy. NCRP recommendations
state that an upper limit of 5% transmission should be set. However,
currently available machines employ collimators with reduced
transmission to less than 0.5%. Adequate shielding beyond the
useful field edges introduces problems of excessive dimensions,
even when high atomic number materials (ie. lead or steel) are used.
To conserve space, collimating devices are often fabricated from
depleted uranium, or an expensive tungsten alloy having a density

more than •1.5 times that of lead.

A block diagram of the components of the linear accelerator •
and their relative position is shown in figure 2.13
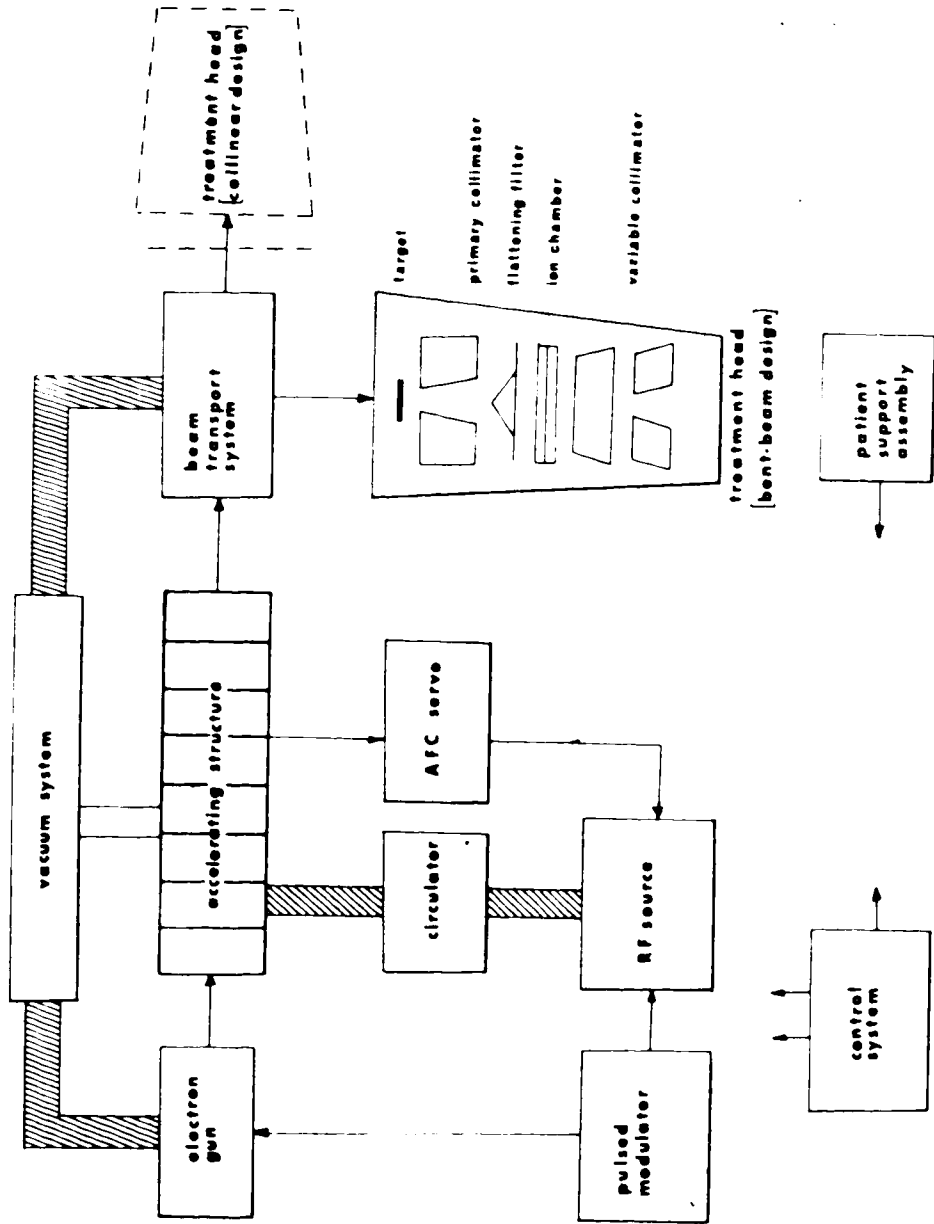
FIGURE 2.13. Block diagram illustrating the subsystems of a medical linear accelerator and their relative positioning. (Karzmark, 1973).

CHAPTER III

INTERACTIONS OF X-RAYS AND ELECTRONS WITH MATTER

3.1 ATTENUATION OF PHOTON BEAMS

The processes contributing to the removal of photons from the primary beam are statistical in nature. The probability of interaction is a function of the incident photon energy and the composition of the absorbing medium. Reduction of the intensity of a narrow beam, during passage through an absorber, is attributed to two basic processes. These are local absorption of the incident photon, and scattering with subsequent removal from the beam. To a first approximation the attentuation of an x-ray beam is considered to be exponential in nature. The fractional reduction of the beam intensity "I" is proportional to the thickness "dx" of absorber traversed by the beam and is described by the differential equation:

$$- \frac{dI}{I} = \mu dx$$

the solution of which is: $I(x) = I(0)e^{-\mu x}$.

The linear attenuation coeficient, μ, characterizes the penetration and diffusion of the photon beam in extended media and is defined as the probability per unit path length that a photon will interact with the medium.

The above relation does not apply to broad beam geometries, where the irradiation area is fairly large and scattered photons

58

reach the detector. These secondary photons arise in the absorber, mainly as a result of Compton scattering. For broad beam geometries the attenuation is still exponential but is modified by two additional factors. One, the "geometric factor" applies to the source geometry. The second factor, often called "build-up factor", accounts for the contribution of the scattered photons which reach the detector (Fitzgerald et al., 1967).

In a narrow beam, the thickness t of the absorber required to reduce the beam intensity by a factor of e is called the mean-free-path. This thickness equals the inverse linear attenuation coefficient and represents the average distance travelled by a photon between successive interactions. The attenuation coefficient can be made independent of density when expressed in $cm^2 g^{-1}$. This is referred to as the mass attenuation coefficient, μ/ρ, and is defined as the fractional reduction in the beam intensity produced by a layer of absorber of thickness $1gm/cm^2$.

Similarly, the atomic and electronic attenuation coefficients are defined by the equations

$$_a\mu = (\mu/\rho)(A/N_o)$$

$$_e\mu = (\mu/\rho)(A/N_o Z)$$

respectively. In these expressions, A is the atomic weight of the absorber, Z is its atomic number and N_o is Avogandro's number. The atomic and electronic attenuation coefficients are commonly referred to as cross-sections. Values of attenuation coefficients for a large range of energies and atomic numbers have been published

In the NBS Report 29, 1969.

Photons interact with matter by a number of mechanisms, depending on their energy and the properties of the absorbing medium. However, for the range of energies dealt with in this report, interactions are limited to three primary processes; in order of importance, Compton scattering, photoelectric absorption and pair production. Photon interactions through these processes result in a large amount of ionization of the atoms and molecules of the absorber.

3.1.1 Compton-scattering

Compton-scattering is an inelastic and incoherent type of collision. It assumes that photons interact with loosely bound or virtually free electrons, rather than with the atom as a whole. During the collision, part of the incident energy is transferred to the recoil electron, which is scattered at an angle "θ" relative to the direction of incidence. The photon leaves the site of interaction, degraded in energy and deflected from its initial path by an angle ϕ. Mathematical considerations of conservation of momentum and energy lead to the following relationships between energy and angle for the scattered electron and photon:

$$E = h\nu_o \frac{\alpha\,(1-\cos\phi)}{1 + \alpha(1 - \cos\phi)}$$

$$h\nu = h\nu_o \frac{1}{1 + \alpha(1-\cos\phi)} \qquad \alpha = \frac{h\nu_o}{m_o c^2}$$

$$\text{and } \cot\theta = (1 + \alpha)\tan\phi/2$$

Here, E is the kinetic energy of the recoil electron, $h\nu$ is the kinetic energy of the scattered photon and $h\nu_0$ is the incident photon energy.

The electron acquires the maximum energy when scattered at 0°. This value corresponds to a 180° deflection of the incident photon. At this limit the energy equations can be written as:

$$h\nu_{(min)} = h\nu_0 / (1 + 2\alpha)$$

$$E_{(max)} = 2\alpha_0 h\nu / (1 + 2\alpha)$$

While the photon can be scattered at any angle between 0° and 180°, the maximum deflection of the electron is 90°. Around shallow photon scattering angles the recoil energy of the electron is so low that the binding effect becomes of importance. The assumption that the electrons participating in the interaction are free is valid only if the momentum transferred to the electrons greatly exceeds the initial momentum of the electronic motion within the atom. When this condition is not satisfied the probability of occurance of the Compton interaction becomes considerably reduced. As a result the Compton effect is not the predominant interaction for low energy photons, especially when they are incident on high Z absorbers. Heisenberg and Bewilogua evaluated the probability $S(h\nu_0, \phi, Z)$ that any energy absorption results in a Compton interaction with electrons bound to an atom, as a function of the photon energy, scattering angle and atomic number (Nelms, 1953). Their findings are summarized in figure 3.1 , where the dependence of "S" on the above parameters is expressed
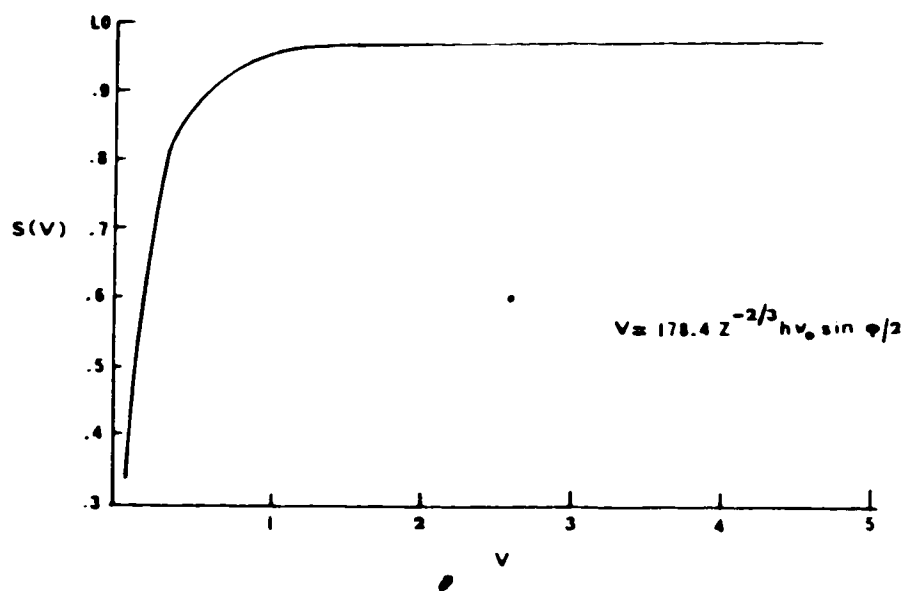
$$V = 178.4 \, Z^{-2/3} h\nu_o \sin \varphi/2$$

FIGURE 3.1. The probability of a Compton interaction as a function of incident photon energy, scattering angle and atomic number of absorber (Nelms, 1953).

in terms of $V = 178.4 \ Z^{-2/3} \ h\nu \ \sin:/2$. The Compton effect then
becomes an efficient process for values of $V \cdot 1$.

For smaller values of V, the photon can interact with the
atom as a unit by means of a coherent, elastic scattering by the
bound atomic electrons. Minimal energy is lost by the photon, so
that it is deflected with a virtually unaltered wavelength. Since
no energy is deposited locally attenuation of the beam is
exclusively due to scattering. The effect is known as Rayleigh
(coherent) scattering.

3.1.2. Compton Cross-sections

The collision differential cross-section, expressing the
probability per unit solid angle d, per electron, that a photon
will be scattered in the direction defined by the angle : as a
result of a Compton interaction, is given to a very good
approximation by the Klein-Nishina formula:

$$\frac{d_e t}{d.} = \frac{e^4}{2m_o^2 c^4} \left[\frac{1}{1+i(1-\cos:)} \right]^2 \left[1+\cos^2 t + \frac{i^2(1-\cos\phi)^2}{1+i(1-\cos:)} \right] cm^2/elec./\ steradian$$

The probability that any amount of energy h will be
scattered in a particular direction is proportioral to the
fractional energy carried off by the scattered photons,

$$h\nu/h\nu_o = \left[1 + i(1-\cos\phi) \right]^{-1}$$

Then, the scattering differential cross-section is described
by the expression:

$$\frac{d_e\sigma_s}{d\omega} = \frac{e^4}{2m_o^2c^4}\left[\frac{1}{1+\alpha(1-\cos\phi)}\right]^3\left[1+\cos^2\phi + \frac{\alpha^2(1-\cos\phi)^2}{1+\alpha(1-\cos\phi)}\right] \ cm^2/electr./\text{steradian}$$

Consequently, the differential absorption cross-section, referring to the energy transferred to the electron in the form of kinetic energy is:

$$\frac{d_e\sigma_a}{d\omega} = \frac{d_e\sigma_t}{d\omega} - \frac{d_e\sigma_s}{d\omega} \quad cm^2/\text{electron/steradian}$$

By integration of the above over all angles ϕ, the total Compton cross-sections are obtained. The total collision cross section is the probability of any Compton interaction by one photon, while passing through a layer of material with a thickness of 1 electron/cm^2 and is given by the expression:

$$_e\sigma_t = \int_0^\pi \frac{d_e\sigma_t}{d\omega} 2\pi\sin\phi d\phi =$$

$$= \frac{2\pi e^4}{m_o^2c^4}\left\{\frac{1+\alpha}{\alpha^2}\left[\frac{2(1+\alpha)}{1+2\alpha} - \frac{\ln(1+2\alpha)}{\alpha}\right] + \left[\frac{\ln(1+2\alpha)}{2\alpha} - \frac{1+3\alpha}{(1+2\alpha)^2}\right]\right\} \ cm^2/electr.$$

Similarly the total Compton scattering cross-section is:

$$_e\sigma_s = \int_0^\pi \frac{d_e\sigma_t}{d\omega} 2\pi\sin\phi d\phi = \frac{2\pi e^4}{m_o^2c^4}\left[\frac{4\alpha^2}{3(1+2\alpha)^3} - \frac{(1+\alpha)}{\alpha^2(1+2\alpha)^2}\right. \cdot$$

$$\left. (1+2\alpha-2\alpha^2) + \frac{1}{2\alpha^3}\ln(1+2\alpha)\right] \ cm^2/\text{electron}$$

Then the total Compton absorption cross-section will be the
difference:

$$_e\sigma_a = {}_e\sigma_t - {}_e\sigma_s \qquad cm^2$$

It is interesting to note that the electronic cross-sections are
independent of the composition of the absorbing material.
However, the formulae are not suitable for evaluation of the cross-
sections at low energies, as the logarithmic and purely algebraic
terms tend to cancel out. In the limit, as the photon energy
approaches zero, the differential scattering cross-section reduces
to the Thomson classical scattering cross-section, independent
of photon-energy:

$$\frac{d_e\sigma_s}{d\omega} = \frac{e^4}{2m_o^2 c^4} (1+\cos^2\phi) \qquad cm^2/electron/steradian$$

3.1.3. Angular Distribution of Compton Scattered Photons and Recoil Electrons

The angular distribution of the number of scattered photons
can be derived from the collision differential cross-section,
considering that:

$$\frac{d\omega}{d\phi} = 2\pi\sin\phi \qquad and$$

$$\frac{d_e\sigma_t}{d\phi} = \frac{d_e\sigma_t}{d\omega} 2\pi\sin\phi \qquad cm^2/electron/radian$$

Then, the distribution of the energy of the photons scattered in any angular interval between ϕ and $\phi + d\phi$ is:

$$\frac{d_e{}^\circ s}{d\phi} = \frac{d_e{}^\circ s}{d\omega} \, 2\pi \sin\phi \qquad cm^2/electron/radian$$

The distribution of the recoil electrons as a function of the angle α is:

$$\frac{d_e{}^\circ}{d\alpha} = \frac{d_e{}^\circ}{d\omega} \, \frac{d\omega}{d\phi} \, \frac{d\phi}{d\alpha}$$

$$= \frac{d_e{}^\circ}{d\omega} \left[\frac{2\pi(1+\cos\phi)\sin\phi}{(1+\alpha)\sin^2\phi} \right] \qquad cm^2/electron/radian$$

Figures 3.2 and 3.3 illustrate the angular distributions for photons and recoil electrons for a range of energies

3.1.4. Energy Distribution of Compton Recoil Electrons

Expression describing the energy distribution of the scattered photons and the recoil electrons are similarly derived. The probability that an electron will acquire any energy in the interval E to (E + dE) is given by:

$$\frac{d_e{}^c(E)}{dE} = \frac{d_e{}^c t}{d\omega} \, \frac{d\omega}{d\phi} \, \frac{d\phi}{dE} \qquad cm^2/electron/ MeV$$

which leads to the expression:
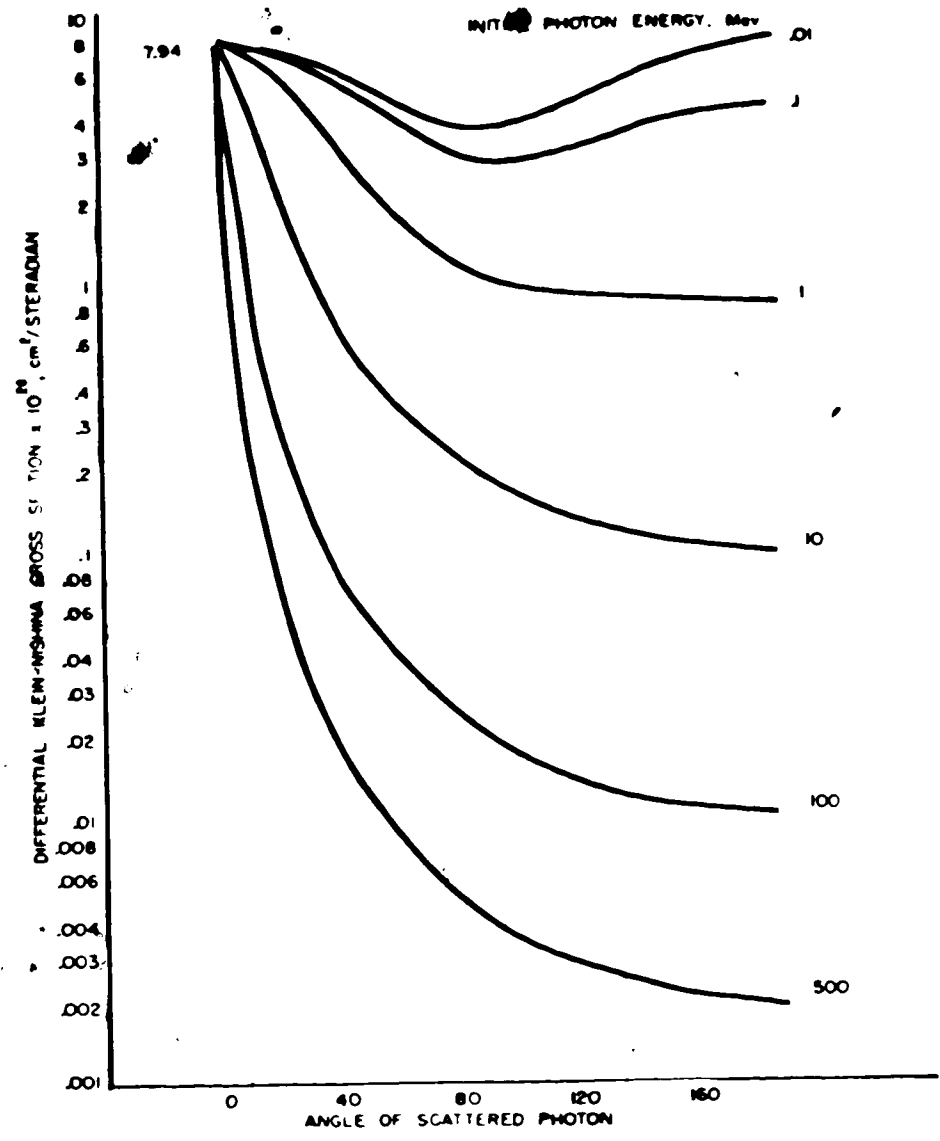
FIGURE 3.2. Differential Klein-Nishina cross-section

per electron - photon angular distribution
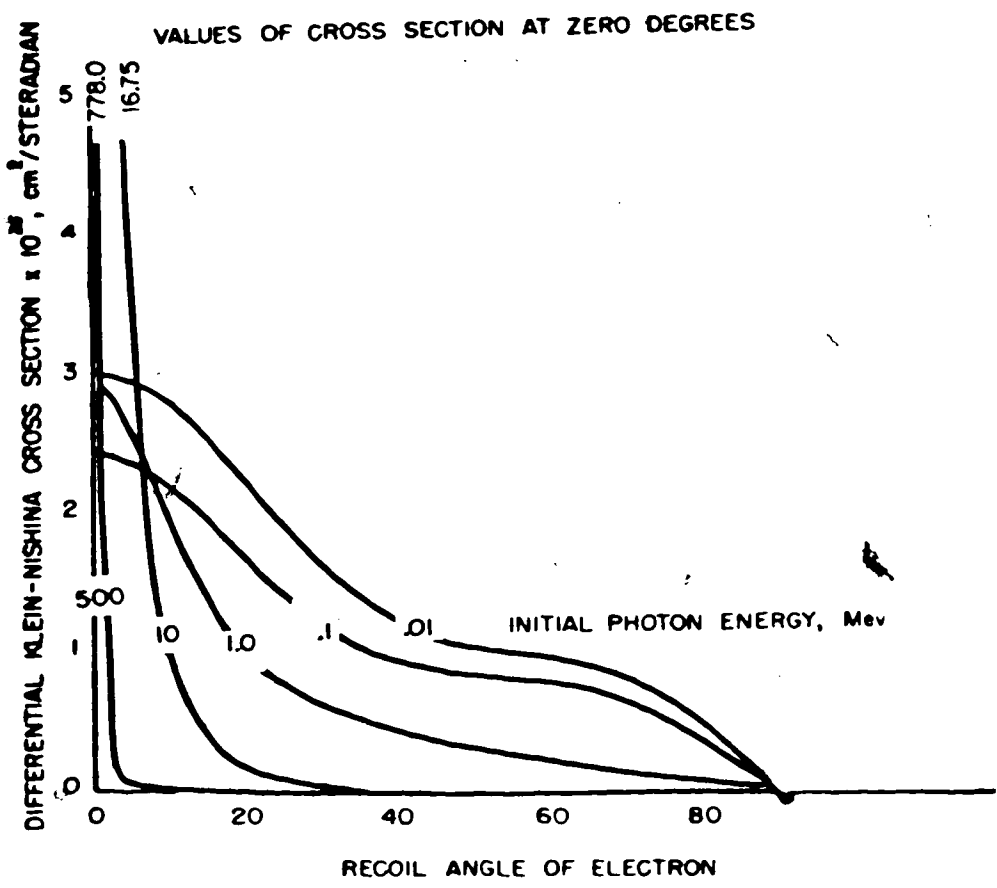
(Nelms, 1953)

FIGURE 3.3. Differential Klein-Nishina cross-
.section - electron angular distri-.
bution (Nelms, 1953).

$$\frac{d_e\sigma(E)}{dE} = \frac{\pi e^4}{m_o c^2 (h\nu_o - E)^2}\left\{ \left[\frac{m_o c^2 E}{(h\nu_o)^2}\right]^2 + 2\left[\frac{h\nu_o - E}{h\nu_o}\right]^2 + \left[\frac{h\nu_o - E}{(h\nu_o)^3}\right]\left[(E - m_o c^2)^2 - (m_o c^2)^2\right] \right\} \quad cm^2/electron/MeV$$

The electron energy spectra have a well defined maximum which occurs at the cut-off value E_{max}. This value is known as the Compton edge.

Since the energy of the scattered photons is $h\nu - E$, their energy spectrum is complementary to that of the recoil electrons.

Calculated data on the Compton energy and angular distributions and the Klein-Nishina cross sections have been graphically presented by A.T. Nelms in NBS Circular 542, 1953.

3.1.5. The Photoelectric Effect

When a photon undergoes a photoelectric interaction, the photon is totally absorbed by a bound electron, which is then ejected from the atom carrying all the deposited energy in excess of its binding energy. In contrast to the Compton effect, the process takes place between the incident photon and the atom as a unit. The fact that the electron is bound rather than free is essential for the photoelectric effect to take place and arises from considerations regarding conservation of momentum. Because of

the relatively large mass of the atom a negligible amount of
energy is transferred to it. The probability of interaction
is a discontinuous function of energy, characterized by various
absorption edges corresponding to atomic shell energy levels.
Otherwise stated, the probability of extraction of a photoelectron
from the atom is maximum when photons have energies similar to,
but exceeding the binding energies of the shells. The photo-
electric effect is an efficient process for low energy photons.
The atomic cross section varies as the inverse cube of the
incident energy, and becomes negligible at about 100 keV and above
in low atomic number absorbers. As the value of Z increases the
energy span for the photoelectric effect shifts to higher values,
due to the increased electron binding energy. This energy and
atomic number dependence is summarized in the empirical relation:

$$_a\tau \propto \frac{Z^{4.1}}{(h\nu_o)^3}$$

where $_a\tau$ is the atomic absorption coefficient. The photoelectric
effect is the terminal interaction by which the Compton-scattered
photons are absorbed in extended absorbers, after having lost a
considerable amount of their energy through scatter.

3.1.6. Pair Production

At energies higher than 1.022 MeV a photon may interact with

the electrostatic field of the nucleus by a process in which

the photon "disappears" and an electron-positron pair is produced.

The created particles carry off essentially all of the energy

in excess of $(2m_c c^2)$ MeV, while the nucleus, due to its large mass,

takes up minimal recoil energy. Therefore momentum is conserved.

This type of interaction can also take place in the field of an

atomic electron, and is referred to as triplet formation. The

threshold energy in this case is found to be 2.04 MeV. After the

positron is slowed down to thermal energy, it combines with an

electron in a pair-annihilation process, producing two .511 MeV

photons. The theoretical value for the atomic cross-section for

pair production in the vicinity of a nucleus is proportional to Z^2:

In summary the attenuation of a photon beam involves two major

processes, those of absorption and scattering. During a photo-

electric interaction or a pair production process, the incident

photon is locally absorbed, transferring its kinetic energy to

the medium in the form of kinetic energy of charged particles.

During a Compton collision with the atomic electrons, the photon

is scattered, carrying off a reduced amount of energy while an

electron is set in motion. The total attenuation coefficient

characterizing the beam is then the sum of those assigned to each

individual process:

$$\mu = \sigma_a + \sigma_s + \tau + \eta \quad (cm^{-1})$$

The probability that one of the interactions will take place,

depends on the incident photon energy and the composition

of the absorber. Their relative significance as a function of

energy is shown in figure 3.4 for photons incident on water and

lead. Figure 3.5 illustrates the energy domain of the three

interactions as a function of the atomic number of the abrsorber.

It can be seen that for low atomic number absorbers the Compton

effect predominates over a wide range of energies.

3.2 INTERACTIONS OF FAST ELECTRONS WITH MATTER

Electrons undergo Coulombic interactions with the atomic

electrons and the electrostatic field of the nucleus. These

interactions result in energy transfer to the medium via ionization

and radiative losses, or in elastic and inelastic deflection of

the incident particles. The mechanisms involved can be classified

in terms of four principle types of interactions:

(i) Inelastic collisions with atomic electrons. Energy is

transferred to one or more atomic electrons, which may be transmitted

to an excited state (excitation of the atom) or to an unbound state

(ionization).

(ii) Inelastic collisions with the nucleus. In the field of

the nucleus, the electrons undergo a deflection from their initial

path. Part of their kinetic energy is taken up by the colliding

pair and the rest is radiated as bremsstrahlung. The probability of

excitation of the nucleus exists, though small.

(iii) Elastic collisions with atomic electrons. The incident
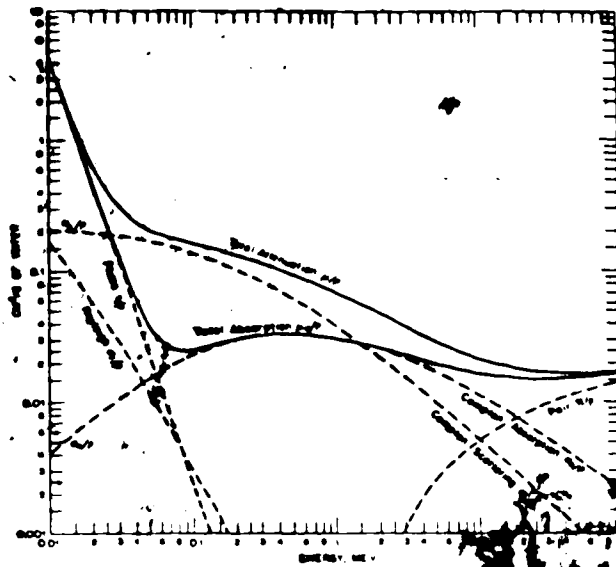
(a)
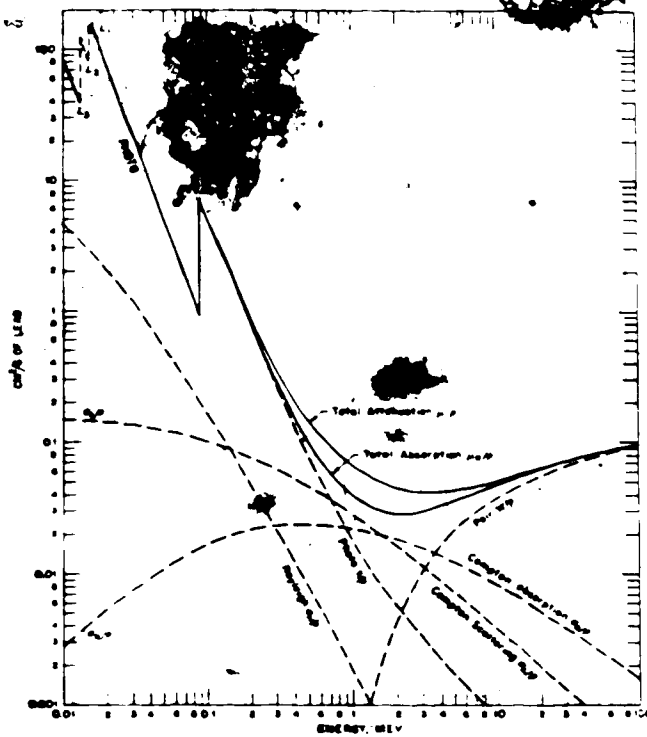
(b)

FIGURE 3.4. Mass-attenuation coefficients as a function of energy for photons in (a) water and (b) lead (Evans, 1955).
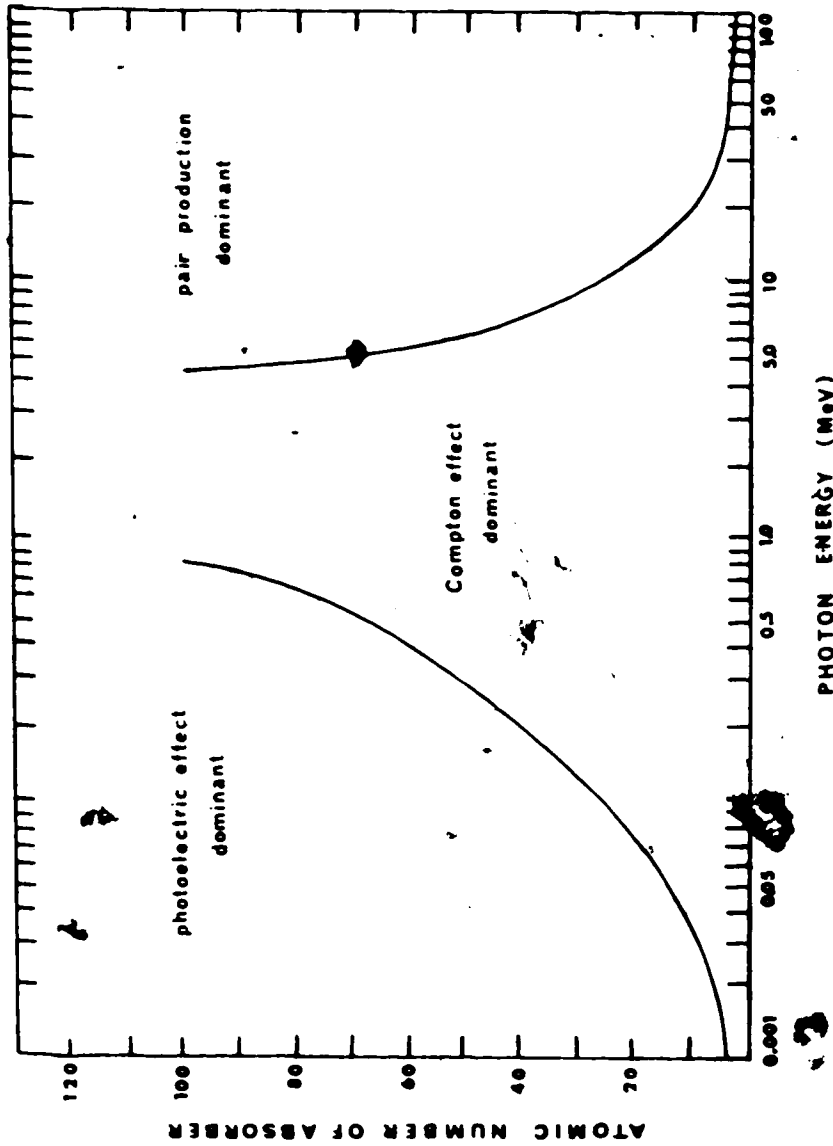
FIGURE 3.5. Relative importance of the three major photon interactions. The lines show the values of Z and $h\nu_0$ for which the probability of the two neighbouring effects is the same (Evans, 1955).

electron is elastically scattered in the field of the atomic electrons. The amount of energy transferred to the atom is generally smaller than its lowest excitation potential. This type of interaction is significant for very low energy electrons.

(iv) Elastic collisions with the nucleus. No radiative energy loss occurs. The incident particle loses only the amount of energy required for the conservation of momentum between the colliding pair. Electrons have a high probability of experiencing elastic scattering, due to their small mass.

From the radiation dosimetry point of view, the only significant mechanisms of energy transfer to the interacting medium are the ones of ionization and radiative energy losses of the incident electron.

3.2.1. Ionization Loss

The incident electron transfers all its kinetic energy to the absorber, via one "hard" collision or a number of "soft" collisions, by atomic excitation and ionization. In hard collisions the kinetic energy imparted to the atomic electron is sufficient to permit the assumption that the struck electron was initially free. The released electrons form δ-rays, which are energetic secondary electrons that lose their energy by ionizing the medium like any negatron. These secondary electrons can thus carry off any amount of energy in the span from a maximum allowable energy E_{max}, equal to the incident electron energy, down to a value E_{min} for which

the electron binding energy becomes significant. However, although hard collisions are responsible for a great amount of energy loss, they are infrequent. The most probable energy loss, which is experimentally important, is through soft collisions. The total relativistic linear energy transfer (LET) i.e., the energy loss of the electron per unit path length in the absorber, has been derived by Bethe and is described by the equation:

$$\left[-\frac{dT}{ds}\right]_{ioniz.} = \frac{4e^4 ZN_o}{m_o v^2}\left[\ln\beta\ \left(\frac{T+m_o c^2}{I}\right)\left(\frac{T}{m_o c^2}\right)^{1/2} - \frac{1}{2}\beta^2\right] \quad MeV/cm$$

where $\beta = v/c$, $v =$ the velocity of the electron,

$m_o =$ the electron rest mass,

$T =$ the relativistic kinetic energy of the electron,

$I =$ the average ionization potential,

$N_o Z =$ the number of electrons per cubic centimeter

of the absorbing medium,

$N_o =$ Avogandro's number.

The Bethe equation assumes that the most energetic electron after the collision is the incident electron. Thus, most of the energy is deposited along the electron path rather than carried off by δ-rays. The energy transfer rate is a function of both the incident beam energy and the composition of the attenuating medium. It decreases with increasing energy up to about 1 MeV, then slowly increases. It is also seen to increase with increasing atomic number of the absorber. The rate of energy loss by an energetic

electron is often expressed in terms of the "stopping power" of the absorber:

$$-\frac{dT}{ds} = {}_e S N_o Z$$

Where $_e S$ is the electronic stopping power, i.e., the stopping power per electron of the medium, described by the following expression:

$$_e S = \frac{4\pi e^4}{m_o v^2} \left[\ln \left(\frac{T+m_o c^2}{I}\right) \left(\frac{T}{m_o c^2}\right)^{1/2} - \frac{1}{2} \beta^2 \right] \quad MeV/cm$$

3.2.2. Radiative Loss

An incident electron can undergo deflection in the field of nucleus, and as a result a photon is emitted. Production of bremsstrahlung is the most important process for electrons with energies considerably in excess of their rest mass energy. The total radiative cross-section describing the probability, per nucleus of absorbing material, that an electron of kinetic energy T will emit a photon with energy in the range $h\nu$ to $h\nu + dh\nu$ is given by the expression (Evans, 1955):

$$\sigma_{rad} = \sigma_o \bar{B} Z^2 \quad (cm^2/nucleus)$$

where: $\sigma_o = 1/137 \ (e^2/m_o c^2)^2 = 5.8 \times 10^{-28} \ cm^2/nucleus$

and $\bar{B} =$ is a complicated function of Z and T, the value of which

depends on energy. For non relativistic energies $\bar{B} = 16/3$, for $m_o c^2 \ll T \ll 137 \, m_o c^2 z^{-1/3}$

$$\bar{B} = 4 \left[\ln\left(2 \; \frac{T+m_o c^2}{m_o c^2} - 1/3\right) \right]$$

and for

$$T \cdot 137 \, m_o c^2 \, z^{-1/3}, \quad B = 4 \left[\ln(183 \; z^{-1/3} + 1/18) \right]$$

The total radiative energy loss

$$\left[-\frac{dT}{ds} \right]_{rad.} = N \; (T + m_o c^2) \cdot \quad _{rad.}$$

varies approximately as $z^2 E$, where E : the total energy of the electron. Figure 3.6 summarizes the above obse▮▮▮ regarding the two types of energy losses. For sufficient▮▮▮ energies, the predominant energy loss is via ionization. As the incident energy increases radiative losses gain in importance until, for sufficiently high energies, they become the most efficient process. The energy for which ionization losses equal the radiative losses is called the critical energy, its value depending on the atomic number of the absorber and the incident electron energy. The critical energy is 340 MeV in hydrogen and 7 MeV in lead (Fitzgerald et al., 1967)

3.2.3 Electronic Range

Although inelastic collisions with atomic electrons and the
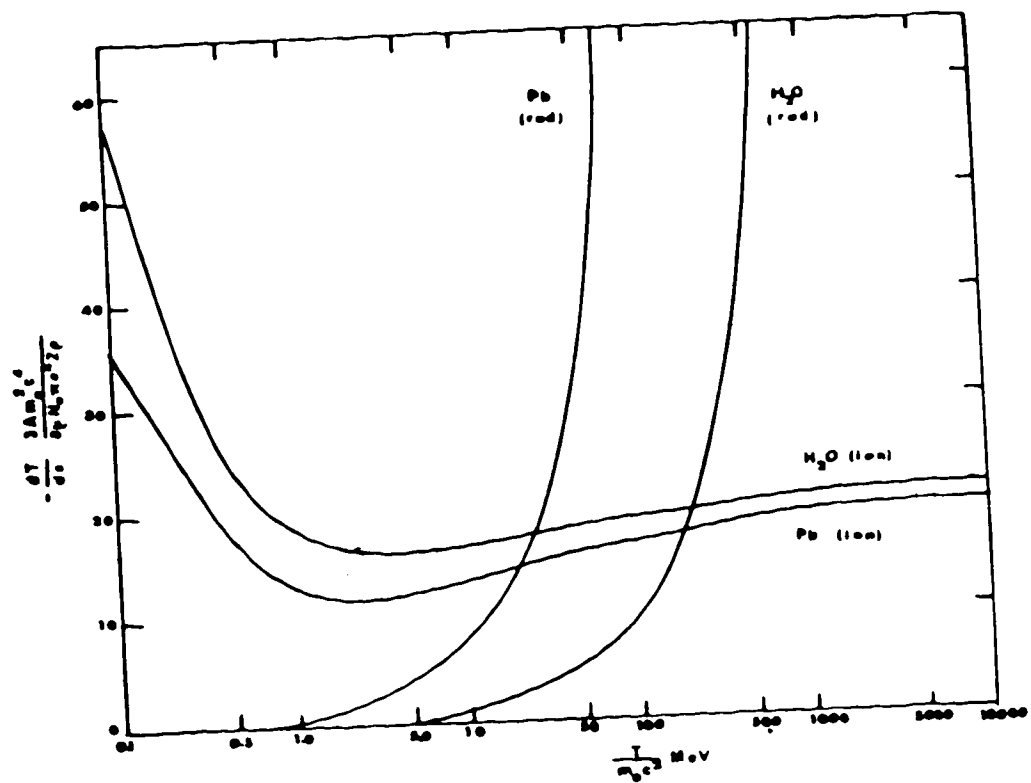
FIGURE 3.6. Average energy loss for electrons in lead and water, as a function of energy (Fitzgerald, 1967).

nucleus are the only important interactions from the transfer of energy stand point, elastic nuclear interactions are also important when the particle's total path length and range is considered. The range of a particle in a thick absorber is an experimental concept and relates to the thickness of absorber which the particles can penetrate. The total path length on the other hand, corresponds to the actual distance within the absorber travelled by the particle before it comes to rest.

Due to the statistical nature of both scattering and energy loss processes, the ranges of particles with the same initial energies will in general not be identical. This variation in range is referred to as "range straggling". Likewise,an initially monoenergetic beam, after transversing a given thickness of absorber, will exhibit an energy distribution (energy straggling). Therefore, the range "R" assigned to the beam can be considered to be the total path length of the few electrons that suffer no scattering or radiation losses. Theoretically the range of monoenergetic beams can be calculated using the linear energy transfer equation, as follows:

$$R = \int_{T_{max}}^{0} - \frac{dT}{\left[- \dfrac{dT}{ds} \right]_{ioniz.}}$$

The energy deposited is the absorbing medium as a function of penetrated depth is shown in figure 1.1.b. The initial non-exponential part of the curve for higher energy electrons is attributed to the presence of bremsstrahlung (photon contamination) produced by the higher energy electrons, while the negative slope represents attenuation of the beam due to straggling.

There is no theoretical expression permitting the calculation of the range of heterogeneous beams. Katz and Penfold, using available experimental data, obtained the empirical range energy relationsip:

$$R_{Al} (mg/cm^2) = 412E^n, \quad n = 1.265 - 0.0954 \ln E$$

Feather proposed an expression which is satisfavtorily accurate for energies higher than 0.6 MeV, and up to 20 MeV:

$$R_{Al} (gm/cm^2) = 0.530T - 0.160$$

where R_{Al} is the range in aluminum and E is the particle's energy expressed in MeV (Evans, 1955).

CHAPTER IV

THE MEASUREMENT OF ABSORBED DOSE

4.1   UNITS AND TERMINOLOGY

The problem of radiation measurement and standardization in radiology have been dealt with by the International Commission on Radiological Units and Measurements (ICRU) since its establishment in 1925.

The first radiation unit, the roentgen, was defined in 1928 and revised in 1937 as follows":.. The international unit of quantity or dose of x-rays shall be called the 'roentgen' and shall be designated by the symbol 'r'... the roentgen shall be the quantity of x or gamma radiation such that the associated corpuscular emission per 0.001293 grams of air produces in air, ions carrying 1 e.s.u. of quantity of electricity of either sign" (ICRU, 1938). The term 'dose' remained unclear until 1950 when it was recommended that"... the dose be expressed in terms of the quantity of energy absorbed per unit mass (ergs/gm) of irradiated material at the place of interest... By 'energy absorbed' is meant the energy imparted to the material at the place of interest." (ICRU, 1951).

The definition of the roentgen as such was inadequate as it was only defined for x and gamma rays and also it was not a measure of absorbed energy. The quantity of absorbed dose was established

in 1962 and was defined as follows: "The absorbed dose (D)

is the quotient of ΔE_D by Δm where ΔE_D is the energy imparted

by ionizing radiation to the matter in a volume element, Δm is the

mass of the matter ▉ that element...

$$D = \frac{\Delta E_D}{DM}$$

the special unit of absorbed dose is the rad" (ICRU 10a). The

rad is equivalent to absorbed energy of 100 ergs per gram of

irradiated matter (ICRU, 1954). The roentgen was then assigned

to the quantity 'exposure dose' defined as"...a measure of the

radiation that is based upon its ability to produce ionization"

(ICRU, 1957). In 1962 the term 'exposure dose' was changed to

'exposure'

$$X = \frac{\Delta Q}{\Delta m}$$

where ΔQ is the sum of the electrical charges on all the ions of

one sign (positive or negative) produced in air when all the

electrons (negatrons or positrons) liberated by photons in a

volume element of air whose mass is Δm are completely stopped

in air."

Finally in 1974 the Gray was adopted as a unit of absorbed

dose which"...can also be used with other physical quantities,

expressed in joules per kilogram, provided that these quantities

belong to the field of ionizing radiations" (ICRU, 1974). Thus

the Gray (symbol Gy) is equivalent to 100 rads of absorbed dose.

Table I summarizes all the quantities and units recommended

TABLE I

QUANTITIES AND UNITS RECOMMENDED BY THE ICRU (1962)

Name	Symbol	Dimensions	Units		
			mksa	egs	Special
Energy imparted (integral absorbed dose)	–	E	J	erg	grad
Absorbed dose	D	EM^{-1}	Jkg^{-1}	erg g^{-1}	rad
Absorbed dose rate	–	$EM^{-1}T^{-1}$	$J\ kg^{-1}s^{-1}$	erg $g^{-1}s^{-1}$	rad s^{-1} etc.
Particle fluence or fluence	Φ	L^{-2}	m^{-2}	cm^{-2}	–
Particle flux density	φ	$L^{-2}T^{-1}$	$m^{-2}s^{-1}$	$cm^{-2}s^{-1}$	–
Energy fluence	F	EL^{-2}	$J\ m^{-2}$	erg cm^{-2}	–
Energy flux density or intensity	1	$EL^{-2}T^{-1}$	$J\ m^{-2}s^{-1}$	erg $cm^{-2}s^{-1}$	–
Kerma	K	EM^{-1}	$J\ kg^{-1}$	erg g^{-1}	–
Kerma rate	–	$EM^{-1}T^{-1}$	$J\ kg^{-1}s^{-1}$	erg $g^{-1}s^{-1}$	–
Exposure	X	QM^{-1}	$C\ kg^{-1}$	esu g^{-1}	R (roentgen)
Exposure rate	–	$QM^{-1}T^{-1}$	$C\ kg^{-1}s^{-1}$	esu $g^{-1}s^{-1}$	Rs^{-1}, etc.
Mass attenuation coefficient	μ/ρ	L^2M^{-1}	m^2kg^{-1}	cm^2g^{-1}	–
Mass energy – transfer coefficient	$\mu k/\rho$	L^2M^{-1}	m^2kg^{-1}	cm^2g^{-1}	–
Mass energy – absorption coefficient	$\mu en/\rho$	L^2M^{-1}	m^2kg^{-1}	cm^2g^{-1}	–
Mass stopping power	S/ρ	EL^2M^{-1}	$J\ m^2kg^{-1}$	erg cm^2g^{-1}	–
Linear energy transfer	L	EL^{-1}	$J\ m^{-1}$	erg cm^{-1}	$\frac{KeV}{(\mu m)^{-1}}$
Average energy per ion pair	W	E	J	erg	eV

TABLE I cont'd

Name	Symbol	Dimensions	Units		
			mksa	cgs	Special
Activity	A	T^{-1}	s^{-1}	s^{-1}	Ci (curie)
Specific γ-ray constant	Γ	QL^2M^{-1}	$C\ m^2kg^{-1}$	$esu\ cm^2g^{-1}$	$R\ m^2h^{-1}$ Ci^{-1}, etc.
Dose equivalent	DE	—	—	—	rem

by the ICRU in 1962. The definitions have remained unchanged
with two exceptions: The introduction of the Gray as a unit of
absorbed dose and the replacement of the Curie by the Becquerel,
as a unit of activity:

$$1 \text{ Bq} = 1\text{s}^{-1} \doteq 2.703 \times 10^{-11} \text{ Ci}$$

4.2 X-RAY AND ELECTRON DOSIMETRY

Radiation dosimetry involves the development of theoretical
methods for evaluation of the energy deposited in an irradiated
medium, as well as applied methods for measurement of this energy
in terms of the absorbed dose or dose-rate in the material.
Generally, radiation induces changes in the physical or chemical
state of the absorber. Any material that exhibits measurable
changes when exposed to radiation can be used as a dosimeter.
Evaluation of the absorbed dose is then based on both the
properties of the radiation beam, that is, the processes resulting
in the energy transfer to the medium, and the properties of the
dosimeter itself.

The following methods are employed in x-ray and electron
dosimetry:

(a) Ionization methods, involving derivation of the absorbed
dose from measurements of the ionization produced in a gas filled
cavity.

(b) Solid state dosimetry based on the properties of certain

solids which may exhibit changes in their luminescent properties or their conductivity. The magnitude of these changes must be proportional to the absorbed dose.

(c) Calorimetry, i.e., measurement of the energy absorbed by the irradiated system in terms of the increase in temperature, provided that no chemical reaction occurs.

(e) Actinometry or chemical dosimetry which relates the absorbed dose to the chemical changes induced in the dosimeter.

(f) Film dosimetry, which involves measurement of exposure in terms of the degree of change in the optical density of x-ray sensitive films.

4.2.1 Photon Penetration in Thick Absorbers

Photons deposit their energy in a medium through a two step process. They transfer their energy to the interacting electrons which in turn, deposit their energy along their path, via a large number of interactions. It is then necessary to distinguish between energy released by the photons at some point in the absorber and that actually absorbed at this point.

The average energy transferred to the absorber in the form of kinetic energy of electrons per centimeter of absorber is described by the energy transfer coefficient, μ_k defined as:

$$\mu_k = \mu \, \frac{\overline{E_k}}{h\nu_o} \quad cm^{-1}$$

The average energy absorbed $\overline{E}a$ in the medium is a fraction of

$\overline{E}_k$, since the electrons dissipate part of their energy in the form of radiative losses. The energy absorption coefficient, μ_{en}, is then defined as :

$$\mu_{en} = \mu_k \frac{\overline{E}_a}{\overline{E}_k} \; cm^{-1} \qquad or$$

$$\mu_{en} = \mu \frac{\overline{E}_a}{h\nu_0} \; cm^{-1}$$

and describes the average fractional energy, which is truly absorbed per centimeter of absorber. The ICRU introduced a quantity called KERMA (kinetic energy released in the medium), which represents the energy transfer from the incident beam to the ionizing particles. KERMA is defined for a beam of ΔN photons each of energy $h\nu$, crossing an area Δa as follows :

$$K = \frac{\Delta N}{\Delta a} \; h\nu \; \frac{\mu_k}{\rho}$$

where $\mu_k/\rho = (\mu/\rho)(\overline{E}_k/h\nu)$ is the mass-energy transfer coefficient.

The subsequent deposition of the electrons' kinetic energy to the medium is described by the absorbed dose. Penetration of a photon beam through consecutive thin layers (much smaller than the electron range) of the absorber will give rise to an electron flow from layer to layer. Considering that photons generally have much longer ranges than the generated electrons, it can be assumed to a first approximation that the number of electrons set in motion

in each layer is independent of the penetrated depth for all values smaller than the photon range. Then the total number of electrons traversing each layer will increase to reach a maximum at a depth "d_{max}" equal to the mean electron range, and this number will remain constant for all greater penetrated depths. Consequently, the absorbed dose as a function of depth will exhibit a similar behaviour. These ideas are demonstrated in figure 4.1. The thickness of the absorber enclosed between the surface and the depth of maximum absorbed dose is called build-up region and the portion beyond this, the region of electronic equilibrium. However, in practice true electronic equilibrium is never attained due to attenuation of the primary beam. This attenuation is due to two factors.

(i)   The exponential reduction in beam intensity, after penetrating thickness dx of the absorber: $\Delta I = -I \mu dx$

(ii) The reduction of beam intensity, predicted by the inverse square law, which is derived from geometric considerations. If a point source is considered, located at a center of a sphere, then the radiation intensity across the surface of this sphere varies as the inverse square of the radius: $I \propto r^{-2}$

Therefore, the number of electrons found in each slab will still rise to a maximum at d_{max}, which is somewhat smaller than the average electron range. Beyond the equilibrium thickness the absorbed dose will slowly diminish with depth, as shown in figure 4.1.
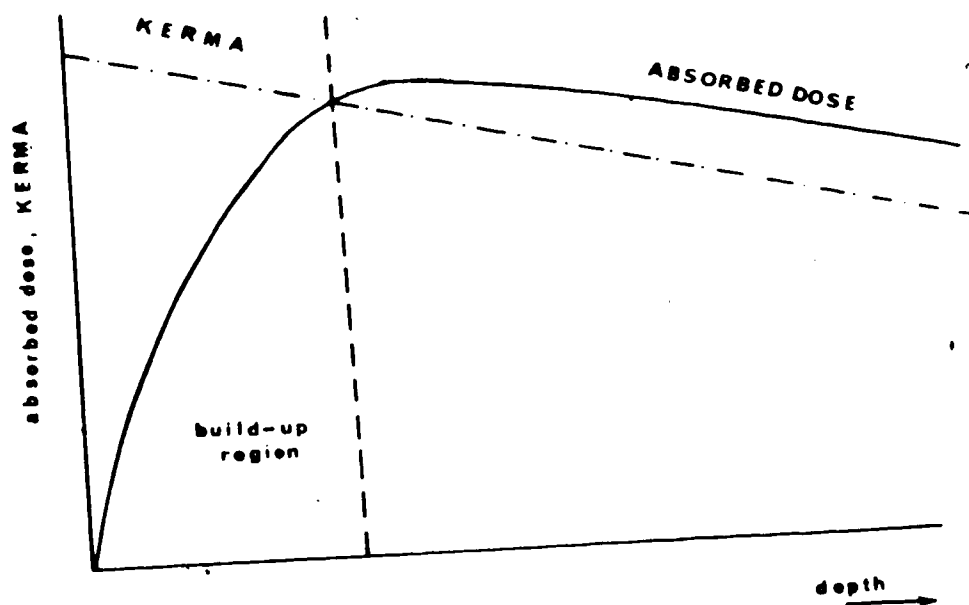
FIGURE 4.1. Variation of absorbed dose and KERMA with depth in the absorber.

4.2.2? Ionization Methods of Dosimetry

Any device placed at some point in the absorber with the aim of measuring the dose absorbed by the medium at the same point, introduces a discontinuity in the system which is generally referred to as a "cavity". Ionization methods of dosimetry involve the measurement of the amount of ionization produced in such a cavity and the interpretation of this measurement in terms of the dose absorbed by the medium at the same point, if the cavity were not present.

An ionization chamber is essentially an air or gas filled cavity, enclosed by a "chamber wall " constructed from material with similar properties to that of the medium or the gas. Although ionization chambers traditionally employ gas filled cavities, there is no fundamental reason for this limitation and materials of any density can be generally used. The use of an ionization cavity in radiation dosimetry has to satisfy the following basic requirements:

   i.   The dimensions of the cavity are small compared to the range of the secondary electrons.

   ii. The secondary electron spectrum is not affected by the introduction of the cavity.

   iii. The events (ionization) measured in the cavity are primarily due to photon interactions with the absorbing material rather than the gas volume within the cavity.

   iv. The primary photon fluence in the region from where

secondary electrons can enter the cavity is spatially uniform.

The measurement of the absorbed dose is a three step procedure. It involves the measurement of the amount of ionization "J_g" produced at the point of interest in the cavity, interpretation of this measurement in terms of absorbed dose, and application of the necessary corrections to account for perturbations at the presence of the chamber.

If, to a first approximation, the radiation losses are considered negligible, the processes resulting in energy transfer to the medium are those of excitation and ionization. The amount of energy required to produce an ion-pair is denoted by "W" and is found to be a constant, independent of the energy of the ionizing particles, with the exception of very low energies for which the electron velocity approaches the orbital velocity. Generally, the energy dependence of W is negligible in all gases for electrons with energies greater than 20 keV (ICRU 1964). The ionization in the gas cavity is measured experimentally and the energy deposited in the gas volume can thus be obtained.

The next step is then to determine the energy absorbed at the same point if the gas volume was to be substituted by an identical volume of the absorbing material. The cavity-ionization theory formulated by Bragg and Gray predicts that the introduction of a gas filled cavity into a homogenous solid material does not perturb the existing electron spectrum, provided that the cavity

is small compared to the electronic range. Then, the energy
absorbed per unit volume in the gas cavity will be equal to the
energy absorbed per unit volume of the solid multiplied by the
factor $(S_g^{med})^{-1}$, where S_g^{med} is the average mass stopping power
ratio of the solid to that of the gas:

$$E_{med} = S_g^{med} W_g J_g$$

If E_{med} is expressed in terms of ergs per gram, the corresponding
absorbed dose D expressed in rads is:

$$D = 0.01 \, E_{med} (rad)$$

When a cavity ionization chamber is used to measure absorbed
dose in any medium from a photon beam, a wall of sufficient
thickness to ensure electronic equilibrium has to be provided. To
avoid additional disturbance of the electron flux, the wall material
is matched to either the absorber or the gas in the cavity, which
is usually air for convenience. The only electrons that enter
the cavity originate in the walls and the absorbed dose is
given by the general expression:

$$D_{med} = 0.869 \frac{Q}{V} \cdot S_{air}^{wall} \cdot \frac{(\mu_{en}/\rho)_{med}}{(\mu_{en}/\rho)_{wall}} \cdot A_{eq} \cdot K(T,P)$$

A_{eq} is a correction factor accounting for the perturbation
of the photon flux, due to the presence of the cavity, μ_{en}/ρ is
the mass energy absorption coefficient and K(T,P) is the pressure
and temperature correction:

$$K(T,P) = (\frac{273.2 + t}{273.2}) (\frac{760}{P})$$

4.2.3. The Design of Ionization Chambers

In order to measure ionization in air, that is the exposure in the x-ray beam, it is required that all the electrons liberated within a small volume of air surrounding the point of measurement, are collected, and their charge is measured. The exposure at this point can be calculated as:

$$X = \Delta Q / \Delta V$$

In practice, a narrow beam of the x-rays to be measured is allowed to pass centrally between two plates that collect the ions produced between two planes, thus defining an effective volume "V". For meaningful measurement this volume must be accurately known and the collected ions should be liberated within this volume only. However electrons set in motion earlier in the path of the x-rays will enter the volume V and some of those liberated in this volume will be scattered away before being collected. The above requirement then amounts to the need for constant electron flow through V, which in turn implies that equilibrium conditions should be established prior to measuring the exposure. Figure 4.2 illustrates diagramatically the design of a free-air ionization chamber. The two collecting plates are separated by a distance of approximately 2R, where R is the electronic range, in order that the liberated electrons do not reach the plates. The upper plate is
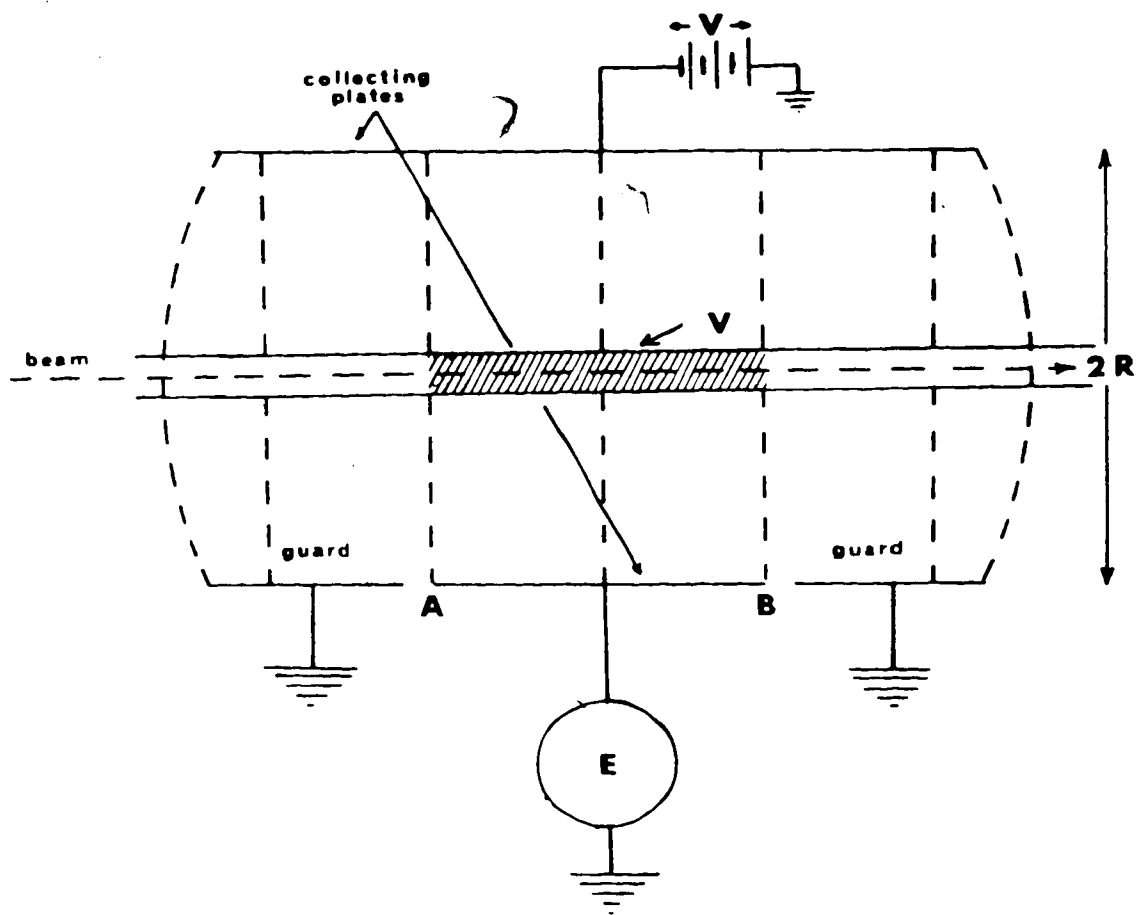
FIGURE 4.2. Schematic representation of the free-air

ionization chamber.

at a negative potential, while the lower plate is at ground and
connected to an electrometer in order to measure the collected
charge. The effective volume is then defined by the cross-
sectional area of the beam and the distance between the lines of
force of the electric field at the edges of the plates. Since
distortion of the field occurs at the edges, it is desirable to
limit the volume at the center of the field and for this purpose
the lower plate consists of three sections separated by insulating
material. The collecting plate is then the section AB, while
the other two serve as guard electrodes collecting the ions
produced outside the effective volume, which are therefore not
included in the measurement.

The positive and negative ions tend to recombine unless
efficiently separated and collected. Therefore, a sufficiently
high potential should be applied between the plates, the value of
which depends on the concentration of ions in V and consequently
on the exposure rate. When all ions are collected, "saturation"
is attained.

Free-air ionization chambers are exclusively used for
calibration purposes in standardization laboratories. For high
energy photons (greater than 3 MeV) the thickness of air required
to provide electronic equilibrium reaches large, impractical
dimensions. Small "air-wall" chambers have been developed for
routine radiation measurements, the dimensions of which do not
exceed a few centimeters. They employ a solid air-wall with

density much higher than air, but with properties of absorption and scattering of x-rays that are similar to those of air. The inside area of the chamber wall is coated with a thin conducting layer, simulating the upper plate of the free air chamber. A charged electrode is inserted in the center and seperated from the walls by insulating material, which collects the ions produced.

For measurements at higher energies, a chamber calibrated at Cobalt-60 is used, and the obtained reading is corrected by an appropriate factor. In general the dose in the medium is related to the reading of the dosimeter "I" by the expression:

$$D_{med} = I. \; C. \; C_\lambda$$

where C is the calibration factor for the dosimeter at Cobalt-60 energies, and the factor C_λ is obtained from tabulated data (ICRU 14). For 8MV and 6MV x-rays incident on water, C_λ is equal to 0.94, while for Cobalt-60 it is 0.95.

4.2.4. Thermoluminescence Dosimetry

Certain phosphors exhibit thermoluminescence properties when exposed to ionizing radiation. When heated to sufficiently high temperatures after irradiation they luminesce in the visible region of the optical spectrum. In general, exposure to radiation induces changes in the physical state of a crystal (Schulman 1967, Fowler et al., 1966). In the field of the energetic particle,

electrons in the valence band may receive sufficient energy

to be raised to the excitation band or be removed from the

atom and enter the conduction band (figure 4.3). In the case

of ionization, the extraction of an electron from the valence

band leaves behind a deficiency of electronic charge i.e., a

"hole". Both the electrons and the holes move freely through

the crystal and they eventually become trapped at a site of

excess charge of the opposite sign (a "vacancy"). The existence

of such trapping centers is due to structural imperfections of

the crystal itself or to the presence of impurities, if their

energy levels are in the forbidden band. If, on the other hand,

only excitation takes place, the electron remains bound to the

hole creating an "exciton". Excitons can also migrate through

the crystal lattice.

The trapped electron, hole or exciton can return to the

ground state, if the transition is a permissible one, and a

photon will be emitted. The process is generally called

luminescence. The transition to the ground state can occur

spontaneously and the process is then referred to as fluorescence,

or with a temperature dependent delay giving rise to phosporescence.

The latter can be accelerated by thermal agitation and the

phenomenon is known as thermoluminescence. Heating provides the

amount of energy necessary to liberate electrons from their traps.

Upon returning to their ground state they release an amount of

energy, equal to the difference between the two energy levels, in
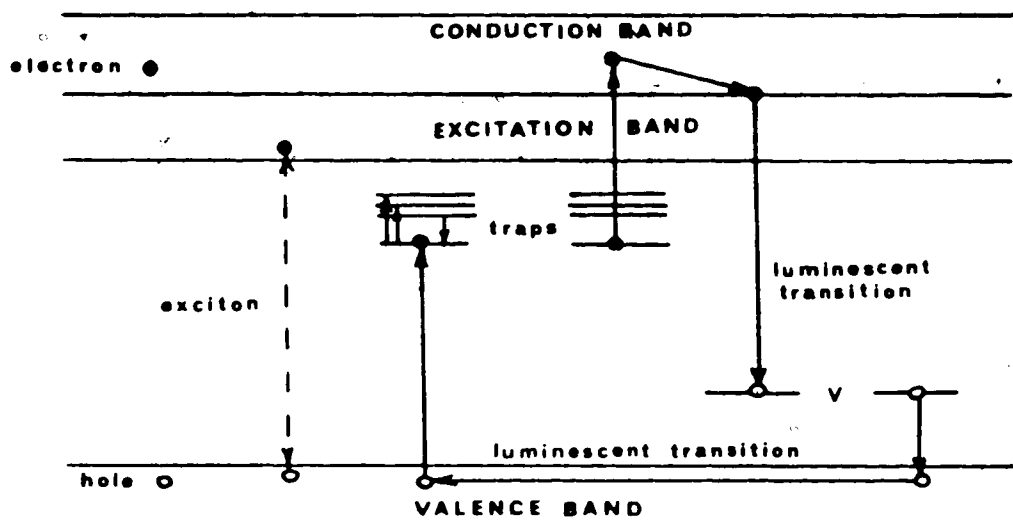
FIGURE 4.3. Mechanism of radiation induced luminescence in solids.

the form of visible light. The amount of light released,

that is the amount of thermoluminescence, is a function of the

number of electrons trapped in the energy level, corresponding

to the thermal energy absorbed by the system. This number is

determined by the amount of energy originally absorbed from the

incident radiation. The system can thus be calibrated and used

as a dosimeter.

The number of electrons remaining trapped at any temperature,

for a constant heating rate $\beta°$/sec, is given by the expression

(Zimmerman et al., 1966):

$$n = n_o \exp\left[-s/\beta \exp (E/KT)\right]$$

where n_o is the initial number of trapped electrons, s is the

frequency factor, related to the frequency of atomic vibrations in

the solid, E is the trap depth, T is the absolute temperature

and K is Boltzmann's constant.

The luminescence intensity is determined by the rate of

emptying the traps:

$$I = \frac{dn}{dt}$$

$$= -\beta\frac{dn}{dT}$$

$$= n_o \ s \ \exp(-E/KT) \ \exp \int_{T_o}^{T} -s/B \ \exp(-E/KT) \ dT$$

The curve of thermoluminescence versus temperature, obtained when

the phosphor temperature is continuously raised, is called the

"glow curve". This is shown for LiF(TLD-100) in figure 4.4. The
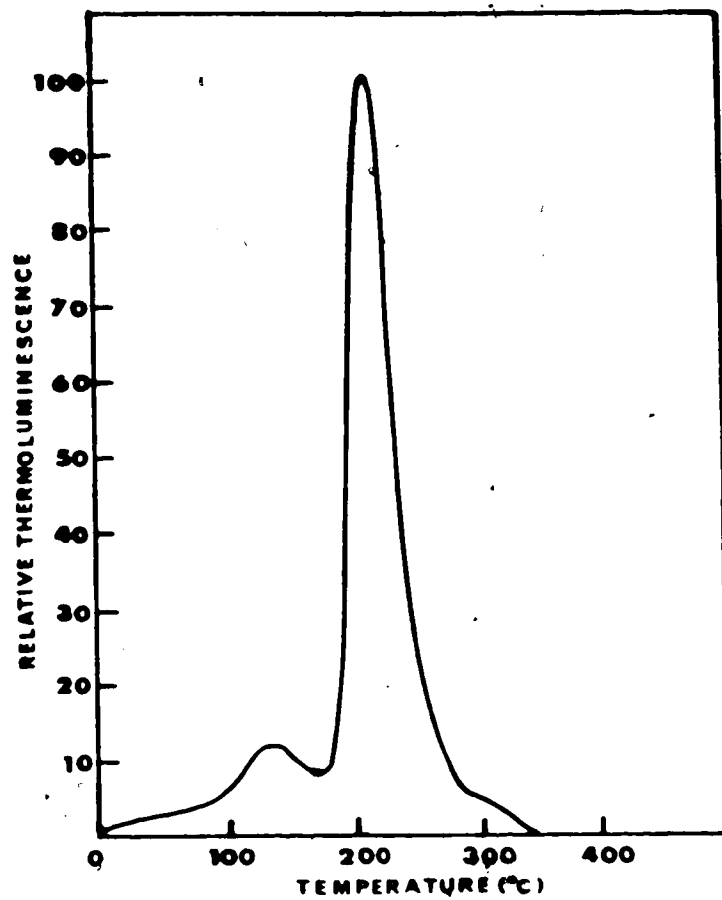
FIGURE 4.4. Glow curve of LiF (TLD - 100) ; heating

rate 5°/sec.

various peaks correspond to traps of different depths, while the total area covered by the curve is related to the total absorbed dose.

By combining the above ideas, it is possible to state the following general requirements that phosphors should meet in order to be successfully used for thermoluminescent dosimetry:

1. High concentration of electron or hole traps.

2. High luminescence efficiency when thermally agitated

3. Long storage of trapped electrons or holes at normal working temperatures.

4. A simple trap distribution for simplicity in interpretating the readings.

5. Stability of traps, i.e., no traps should be created or destroyed by radiation.

6. Energy independence and linear response over a wide range of absorbed dose.

Several thermoluminescent dosimeters have been developed, among which are, Al_2O_3, $CaSO_4$:Mn, LiF, CaF_2:Dy. TLD-100 is a thermoluminescent grade LiF developed by the Harshaw Chemical Company which has been widely used for clinical measurements. It is approximately tissue equivalent and exhibits a linear response over a range of 10-2000 rads of absorbed dose in soft tissue. This response is independent of energy and dose - rate over a wide range (Hendee, 1967). In addition TLD-100 has been found to give reproducible readings and is able to store the

absorbed energy for long periods (Cameron et al., 1964).

Thermoluminescent dosimeters can be reused several times. In order to ensure that all the traps have been emptied the crystals are heated to sufficiently high temperatures to liberate any remaining trapped electrons. It has been reported.that the reannealing procedure changes the properties of the dosimeters and recalibration of each group prior to use is necessary (Zimmerman, 1966; Hendee, 1967).

4.3. DOSIMETRIC FUNCTIONS

The dose received by a small mass of tissue at any point in the absorber consists of two components, i.e., the dose due to primary radiation alone and that due to scattered radiation. The former depends on the experimental geometry and the physical parameters of the beam; it also varies with distance of the point of measurement from the central beam axis. In the presence of beam modifying devices, the dose due to primary radiation depends on the thickness of the absorber (expressed in g/cm^2) that lies between the source and the point in question. The dose due to scattered radiation depends strongly on the size of the irradiated volume. In addition, if there are beam modifying filters the scatter contribution depends on the total amount of scatterer within the beam. In general the dose at any point in a phantom along the central axis of the beam is given by the expression:

$$D(d,W_d,f) = A\ e^{-\mu d}S(d,W_d,f)$$

where W_d is the field size at depth d, f is the source-to-point distance, A is a constant related to the primary beam energy spectrum and μ is the linear attenuation coefficient (Bagne, 1974). The first term represents the attenuation of the incident beam. The second term is the total scatter arising within the absorber. It consists of the forward scatter $S_F(d,W_d,f)$ and the backscatter $S_B(d,W_d,f)$:

$$S(d,W_d,f) = S_F(d,W_d,f)\ S_B(d,W_d,f)$$

In order to facilitate accurate calculation of the absorbed dose at any point within the irradiated volume, certain physical concepts have been developed. These include dosimetric functions such as percentage depth dose, tissue-air-ratio, tissue-maximum-ratio, scatter function and scatter-air-ratio. These functions vary with irradiation parameters and their properties are based on the absorption and scattering characteristics of the x and γ-rays.

Dose measurements for clinical applications are made using "phantoms" that is, absorbers made of tissue equivalent materials.

4.3.1 Percent Depth-dose

Percent depth-dose relates the absorbed dose to a point at some depth along the beam axis, to the absorbed dose at a fixed reference point on the beam axis. It is defined as the ratio of the two doses expressed as a percentage. The point of reference

is usually chosen to be at the depth of maximum absorbed dose:

$$\% \, DD = 100 \, \frac{D(d,W_d,f)}{D(t,W_d,f)}$$

where t is the depth of electronic equilibrium. The percent depth-dose depends on the beam energy, the depth, the source-to-surface distance and the size and shape of the field.

4.3.2 Tissue-air-ratio (TAR)

The tissue-air-ratio is defined as the ratio of the absorbed dose at a given point in a phantom to that measured at the same point in free air, with the minimum volume of phantom material required to provide electronic equilibrium at the point of measurement (Johns et al., 1974).

$$TAR = \frac{D(d,W_d,f)}{D^{'}(d,W_d,f)}$$

The tissue-air-ratio depends on the thickness of the material overlying the point of measurement, the size of the irradiation field and the beam energy. To a close approximation, it is independent of the distance from the source.

The tissue-air-ratio describes the combined effects on the beam of attenuation of the primary radiation and scatter within the phantom. In the special case where the depth equals the equilibrium thickness, the tissue-air-ratio reduces to the backscatter factor:

$$B(W_d) = \frac{D(t,W_d,f)}{D^{'}(t,W_d,f)}$$

The backscatter factor gives the fractional increase of the
dose due to radiation backscattered from the phantom.

The experimental arrangement for TAR measurements is
shown in figure 4.5.

4.3.3 Scatter-air-ratio (SAR)

The scatter-air ratio is an empirical quantity used to
calculate the amount of scattered radiation in an irradiated
phantom. The SAR is derived from tissue-air-ratio data and is
defined by the expression:

$$SAR = T(d,W_d) - T(d,0)$$

where $T(d,0)$ is the "zero-area tissue-air-ratio" (Cunningham,
1971). If the field were reduced to approach zero, the scattering
volume would also approach zero and the dose at depth d would be
due to primary radiation alone. If this value is subtracted from
the TAR value for any field size W_d, a measure of the dose at that
depth due to scattered radiation can be obtained. The quantity
$T(d,0)$ cannot be measured directly but is obtained by plotting
tissue-air ratios for beams with small field dimensions against
beam area and extrapolating to zero.

A similar quantity introduced for the same purpose is the
scatter function, which is derived from percentage-dose and
backscatter data. It expresses the dose from scattered radiation
to a small mass of tissue at depth d, for 100 rads of primary
radiation to a similar mass of tissue at the depth of maximum
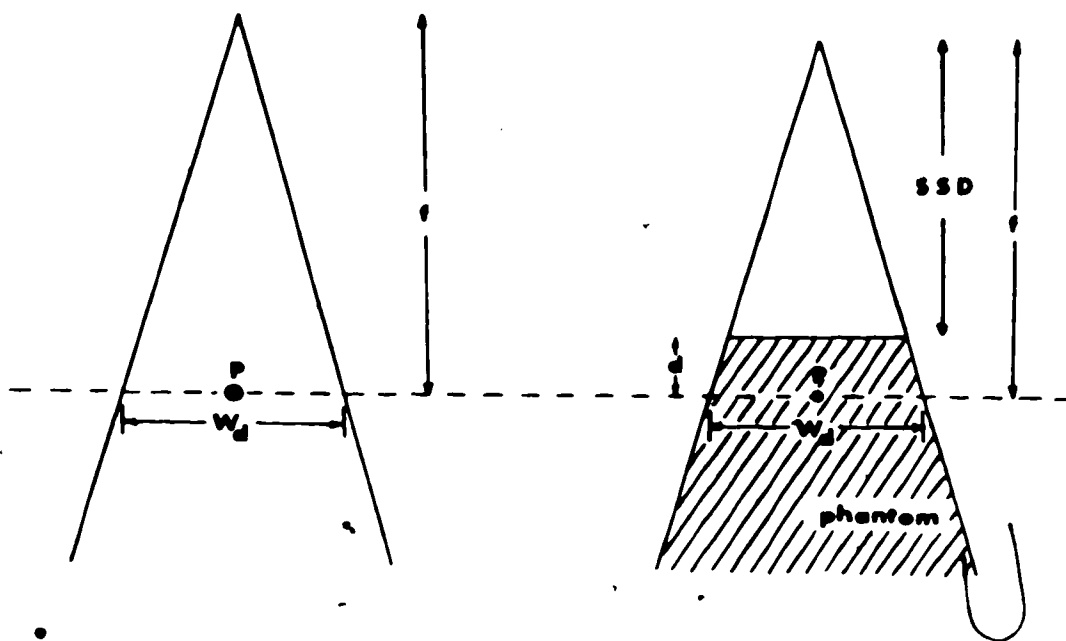
FIGURE 4.5. Experimental arrangement for TAR measurements.

electronic build-up   (Johns et al., 1974).

4.3.4 Tissue-maximum-ratio

The definition of TAR breaks down for high energy radiations, where the required build-up material amounts to several millimeters. Under these conditions, measurements become difficult to interpret, since scatter from the build-up material itself becomes significant.

The concept of tissue-air-ratio has been extended to high-energy x-ray beams as "tissue-maximum-ratio (TMR)". At depth d and field size W_d, the TMR is defined as the ratio of the dose in the medium at some point to the dose for which there is just enough medium covering the point to provide maximum dose build-up at that point (Holt, et al., 1970):

$$TMR = \frac{D(d,W_d,f)}{D(t,W_d,f)}$$

The TMR by definition describes the combined effect of the attenuation of the primary beam in thickness (d - t) in the phantom and the forward scatter $S_F(d,W_d,f)$ generated in the entire thickness d in the absorber (figure 4.6) The backscatter being identical for both doses is cancelled out in the expression and

$$TMR = k\ e^{-\mu(d-t)}\ S_F(d,W_d,f)$$

where k is a constant.

Therefore the TMR can be seen as the equivalent of TAR for higher energies if the former is multiplied by a factor $S(W_d)$

109
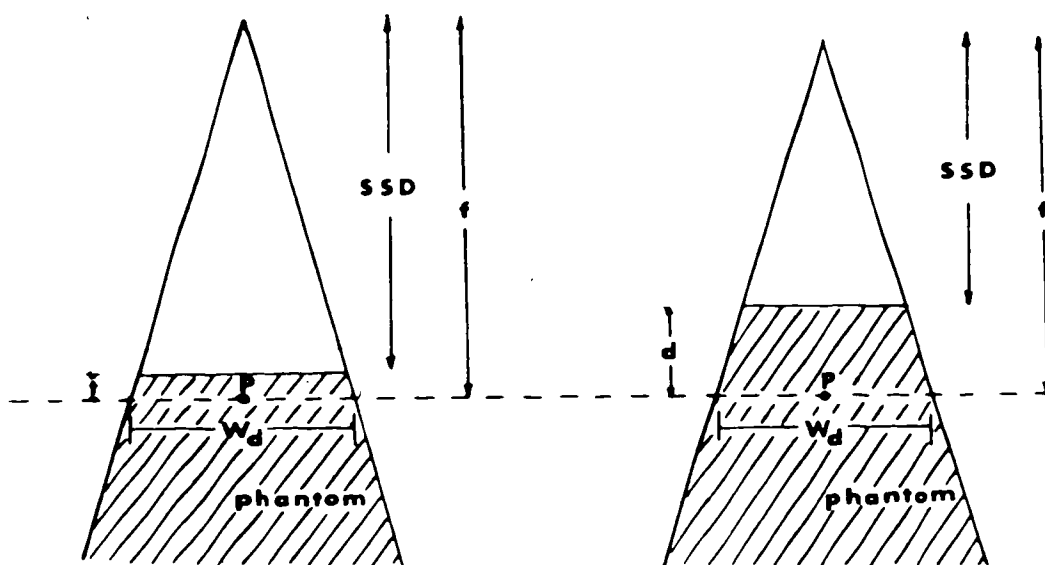
FIGURE 4.6.   Experimental arrangement for TMR measurements.

to account for the phantom backscatter. It is then referred to as the attenuation factor $a(d,W_d)$.

A more general concept related to the TMR is the tissue-phantom-ratio,

$$TPR = \frac{D(d,W_d,f)}{D(d_r,W_d,f)}$$

where $D(d_r,W_d,f)$ is the dose at a specified point on the central axis in a phantom located at a fixed reference depth d_r in the phantom, and $D(d,W_d,f)$ is the dose at the same point with an arbitrary depth d of overlying material (Karzmark, 1965).

CHAPTER V

SURFACE SCATTER FROM MEGAVOLTAGE THERAPY BEAMS

5.1 THE RELATIVE SKIN DOSE AS A FUNCTION OF TREATMENT PARAMETERS

The "skin sparing" effect under various conditions has been studied by a number of workers. The term applies to conditions that will ensure minimal surface (skin) dose in order to prevent adverse skin reactions for doses exceeding the skin tolerance levels.

Skin sparing has been extensively investigated for the surface area defined by the field edges and for points within the field. The dose received by the skin is commonly expressed in terms of the "relative surface dose". This dose corresponds to the dose at zero depth obtained for the particular irradiation parameters (figure 1.1.a).

It has been reported that under certain conditions the relative surface dose increases when a scattering material is positioned in the beam, while the depth of d_{max} shifts towards shallower depths (Richardson et al., 1974; Scrimger 1972; Ibbott et al., 1970; Gray 1973; Leung et al., 1977). These effects have been observed with low Z scattering materials, especially when placed at short distances from the skin, and are attributed to scatter contributions from the material itself. Increase of the relative surface dose also occurs for large field sizes with open beams.

However the situation is different when medium or high Z
scatterers are placed in the beam. Then, for the majority of
experimental conditions, the surface dose is less than that for
open beams. The scatterer acts protectively and is referred to
as a "filter" (Johns et al., 1952; Richardson et al., 1954;
Haybittle 1955; Dutreix et al., 1965). Such filters are some-
times used with t   erapy machines, especially when a large field
is required. The relative surface dose initially decreases with
filter thickness up to a value corresponding to the maximum range
of most of the electrons generated in the collimator and the very
low energy photons of the beam. These are mainly responsible for
the surface dose (Saylor et al., 1971; Gray 1973).

Hine (Hine 1952) measured the dose due to scattered radiation
in the forward and back direction, using a variety of gamma sources
with energies up to 1.35 MeV and a number of scatterers. He observed
that while the forward scatter diminished with Z, the backscatter
increased. The ratio of the forward scatter to the backscatter
was found to increase with beam energy.

The optimum distance between the filter and the phantom consists
of a compromise position between 'two extremes. On the one hand,
with short retraction distances, scatter from the filter itself
reaches the phantom and this increases the surface dose. On the
other hand, long retraction distances allow scatter from the inter-
vening air space to reach the surface unfiltered, again increasing
the surface dose. The best filter position therefore lies between
these two extremes. The requirement for correct positioning of

such objects in the beam is particularly important when using
beam modifying devices. These devices are placed on an accessory
tray, commonly constructed of a small thickness of lucite, which
is a low atomic number material. The choice of such a material is
based on the fact that lucite has sufficient strength to support
heavy beam modifying devices, and is also transparent to light. The
latter facilitates the definition of the field on the irradiation
surface, allowing the light from an -illuminating source to pass
through. Saylor and Quillin (1971) proposed the use of a lead
glass material for such applications, which gave considerably improved
results for the majority of experimental parameters.

Typical source to tray distances used with isocentrically
mounted machines is around 50 cm., and for Cobalt-60 units,trays
are customarily placed at 55 cm.from the source. Large fields
generally require greater separation distances between the filter and
the patient. In general the relative skin dose decreases, as the
ratio of this distance to the radius of the equivalent circular
field is increased (Saylor et al., 1971).

It has been well established that high energy radiation presents
a skin sparing advantage over lower energy therapy beams. Investiga-
tion of the relative skin dose as a function of beam energy has
proved that this advantage is preserved when introducing filters
in the beam (Gray 1973; Gagnon et al., 1975). When comparing differ-
ing energy beams, the relative skin dose should be determined for
the same tumour dose. In the typical case of a deep situated tumour
(around 10 cm. below the skin) and for the same tumour doses and
experimental parameters, the surface dose is considerably reduced

when a higher energy beam is used.

In review, available data suggest that the skin sparing qualities of megavoltage teletherapy beams can, under certain conditions, be improved by the use of filters. The question arises whether or not these qualities are actually preserved when the dose to superficial structures lying outside the field is of concern. Such is the case for example with the treatment of Hodgkin's disease requiring a large field extended out to a few centimeters from the patient's eyes. The investigation presented in this report involves relative measurements of surface scatter at points outside the field and within a few centimeters from its edges. A closely related problem is the scatter arising around beam modifying devices, used with radiotherapy beams. Unlike filters, these devices are placed at certain areas in the field and do not extend over its entire range. Some (i.e. tissue compensators) are commonly constructed from low Z materials and they vary in size and shape. In these experiments, the scatter arising from various materials has been studied for a range of atomic numbers and experimental arrangements.

5.2 MATERIALS AND METHODS

5.2.1. Experimental Arrangement

The radiation scattered from high energy x-ray beams onto the surface of an extended absorber was measured at points outside the field. The experimental set-up is shown diagrammatically in figure

5.1. An approximately tissue equivalent phantom constructed
of dry pressed wood (masonite or hardboard) was positioned in the
beam and at variable distance from the target. The dimensions
were chosen such that the phantom extended well beyond the limits
of the field, and was of adequate thickness to provide full scatter
within and outside the irradiated volume. Such a phantom will meet
the requirements set by ICRU, according to which: "A phantom is a
volume of tissue equivalent material usually large enough to provide
full scatter conditions for the beam being used....". Tissue
equivalent material is "a material whose absorption and scattering
properties for a given irradiation simulate, as nearly as possible,
those of a given biological material, such as soft tissue, muscle,
bone or fat..." (ICRU 24). A phantom should, therefore, have the
same density and number of electrons per gram, as the tissue
simulated. Pressed wood meets these requirements for soft tissue.

Measurements of absorbed dose were taken at points M at
varying lateral distances from the field edge as defined by the
collimators at the set target-to-phantom distance (TPD). The
measurements at these points were expressed as a percentage of the
measurement obtained along the beam axis at the equilibrium depth
d_{max}.

The nature of the scattered radiation was determined by
examining its penetration characteristics. Depth dose distributions
were obtained using LiF thermoluminescent powder (TLD-100), arranged
in thin layers at progressively increasing depths. For this purpose
a number of disks, 3 mm thick, were constructed from lucite, each
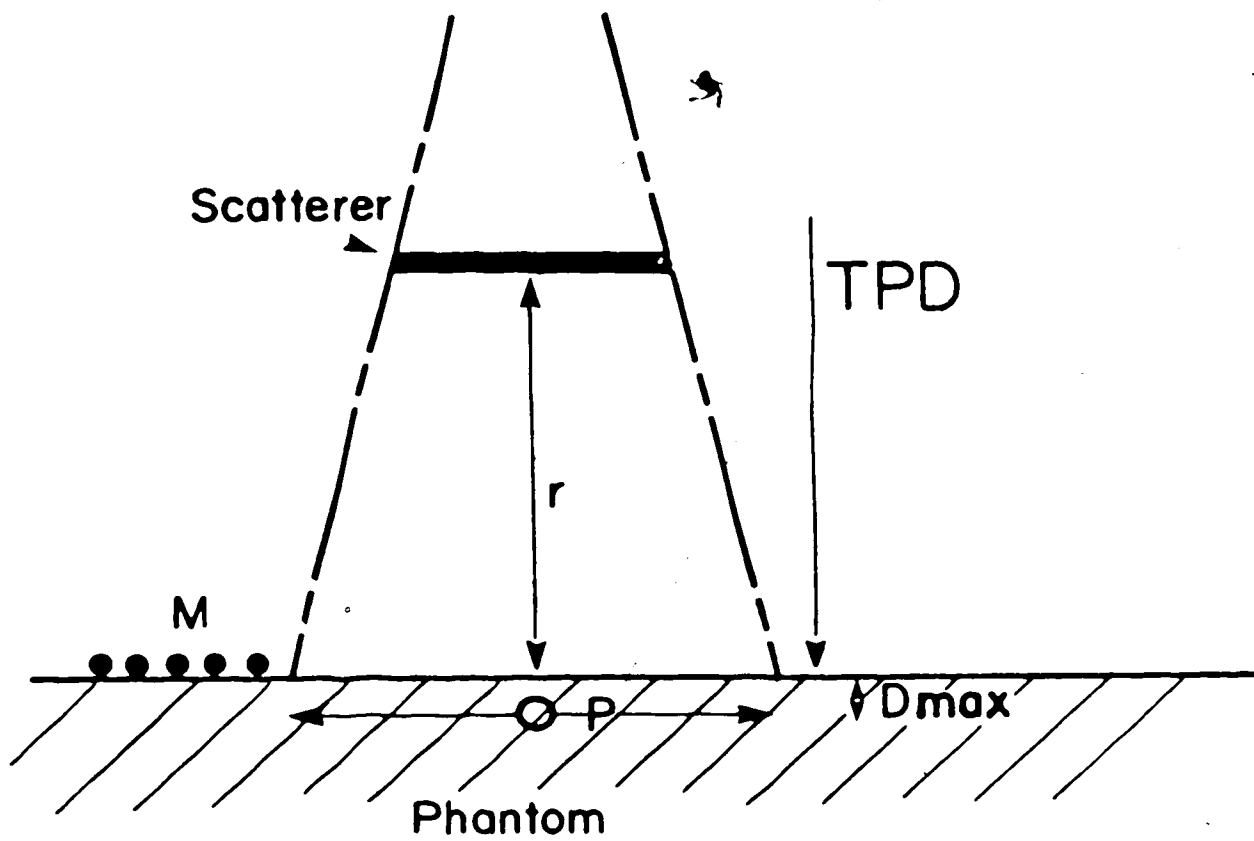
Fig.5.1 Experimental arrangement.

bearing a recess of 1 mm in depth, filled with powder. Thermo-
luminescence dosimetry was favoured for this type of measurement
since, due to the small size of the dosimeters, accurate positioning
at depth varying by a few millimeters only, could be achieved. This
could become a significant source of error if a larger dosimeter
was used.

The distribution of scattered radiation as a function of
distance from the field edge was investigated for open beams at
varying distances from the surface of the phantom. The character-
istics and intensity distribution of the scattered radiation,
produced by scatterers placed into the primary beam, were then
investigated for a number of experimental variables, i.e.,

- field size
- retraction
- position of scatterer in the field
- composition of scatterer
- energy of the x-ray beam

Dose measurements on the surface of the phantom were obtained with
a 0.6 cc ionization chamber in conjunction with an Ionex dose/ dose-
rate meter. The probe was used without build-up material in order to
measure electrons and low energy photons.

The procedure was carried out for the beams from two medical
linacs. An x-ray beam with an effective energy of 2.8 MeV was
obtained from an 8MV linear accelerator (Vickers, Series III). A
second x-ray beam with an effective energy of 1.8 MeV was obtained
from a 6MV linear accelerator (Siemens, Mevatron 6). A similar

series of measurements were also performed,using the Cobalt-60 gamma ray beam (1.25 MeV) in order to measure some of the effects at lower-photon energies.

The effective energy of the beams was obtained from TAR values at zero field size and for tissue equivalent materials, according to the relation:

$$(\mu)_{tis} = \frac{\ln\left[TAR(d_1)/TAR(d_2)\right]}{d_2-d_1}$$

where d_1,d_2 are arbitrary depths (Kijweski, 1978). The photon energies corresponding to the calculated values of $(\mu)_{tis}$ were obtained from tabulated data in NBS, Report 29 (Hubbell, 1969).

5.2.2. Operating Parameters and Performance of the Linear Accelerators

The operation of the 8 MV linear accelerator is determined by a number of parameters. In routine operation, each of these parameters has a fixed value, so that the system yields uniform radiation intensity throughout the field, output of around 300 rads/min at the isocenter and a photon beam with energies up to 8 MeV.

The 8 MV Vickers linear accelerator employs a travelling wave structure. The operating parameters of the system are:

Radiofrequency :   2998 MHz

Power Source :   2MW magnetron (English Electric
                                 M5015)

Duty factor : 10^{-3}

Bending magnet : 90°

Pulse repition rate: 300 p.p.s.

The electron beam is collimated to 0.3 mm diameter and is
transported onto a tungsten target for the production of x-rays.
The emerging beam passes through a brass flattening filter,
conically shaped, with a base diameter of 70 mm and a height of
30 mm. Field flatness is attained at the equilibrium depth, which
in water occurs at 2 cm below the surface. Final adjustment of
the field flatness is achieved by setting the BBM magnetic field
strength. The irradiation field is defined by a pair of motor
driven collimators. It is rectangular in shape and its dimensions
can be continuously varied up to a maximum field size of 25 x 30 cm^2
at 100 cm from the target.

The 6 MV Siemens medical linac differs in design and
construction. It is a standing wave system, providing an electron
beam 3 mm in diameter, and with energies up to 6 MeV. This beam
is transported onto the target by means of a 270° (nominal) achromatic
magnet. The operating parameters of the linac are listed below:

Radiofrequency :   2998 MHz

Power source :   2 MW magnetron (English Electric
                                          M5015)

Duty factor : 10^{-3}

Bending magnet : 261° (nominal 270° deflection system)

Pulse repetion rate :   variable from 0 to 300 p.p.s.

The accelerator is equipped with a tungsten target and a
brass flattening filter. The irradiation field is also rectangular
with a maximum clipped field size of 35 x 35 cm^2 at 100 cm from the
target. The x-ray energy spectrum ranges from a few keV up to 6 MeV.
The depth of maximum ionization in water occurs at 1.5 cm below the

surface.

5.2.3. Dosimetry and Reliability of the Results

The thermoluminescent phosphor used for depth dose measurements
was TLD-100 powder with grain diameter 75-150 microns, manufactured
by the Harshaw Chemical Company. All measurements were expressed
as a percentage of the maximum absorbed dose, therefore calibration
of the dosimeter was not required. It was however decided to
evaluate the dosimeter in terms of its linearity, prior to these
measurements. LiF powder was exposed to known doses of radiation
from the Cobalt-60 beam. The samples were read with a Harshaw
Chemical (model 2000-A) thermoluminescence analyzer. In such a
readout instrument, accurately dispensed samples of approximately
30 mg of powder each, are evenly distributed on a planchette and
heated to $240^{\circ}C$. A photomultiplier tube receives the emitted light
and produces an output proportional to it, which is then amplified
and presented on a digital display. The instrument has a standard
light source, with a light output constant with time, which is used
to determine the stability of the instrument and to set the desired
sensitivity. The performance of the analyzer was found to be
satisfactory. Readings of the light source were reproducible to
within $\pm$ 0.3%. Output measurements of uniformly irradiated powder
samples exhibited an uncertainty of $\pm$ 2.4%. This higher uncertainty
is attributed to small inconsistancies in dispensing equal amounts
of powder for each sample, which predetermines the amount of light
emission. However, this level of uncertainty lies within the

acceptable limits of d̶

The response of LiF powder as a function of absorbed dose
is shown in figure 5.2, and is seen to be linear for absorbed doses
of 100 rads to 1000 rads. During all TLD measurements, a monitor
dose of 1200 rads was delivered to the phantom to ensure that the
dose due to scattered radiation at all points of measurement was
well within the linear region of the dosimeter.

The thimble chamber used for the measurement of the dose on
the surface of the phantom has an approximate air volume of 0.6 cc.
The thimble consists of graphited tufnol, corrected to "air wall"
characteristics, and has a wall thickness of 0.06 cm. The collecting
voltage applied to the chamber is 215 Volts. The accuracy and
consistency of the dose/dose-rate meter is better than +1% as tested
by the manufacturer.

During the measurements of the scattered radiation intensity
at points M on the phantom surface, the ionization chamber was
positioned with its center at the point of measurement. The
geometrical center of a cylindrical ionization chamber coincides with
its effective center unless it is placed at short distances from a
point source. Then, the intensity of the radiation may vary
considerably over the wall giving rise to large inconsistencies.
The problem has been investigated and the maximum observed discrepancy
was less than 2.5 % with the chamber placed at two diameters distance
from the source (Boag, 1966). For the experimental geometries used
here, any error in the determination of the effective center of the
chamber would be minimal, as the distances used were of the order of
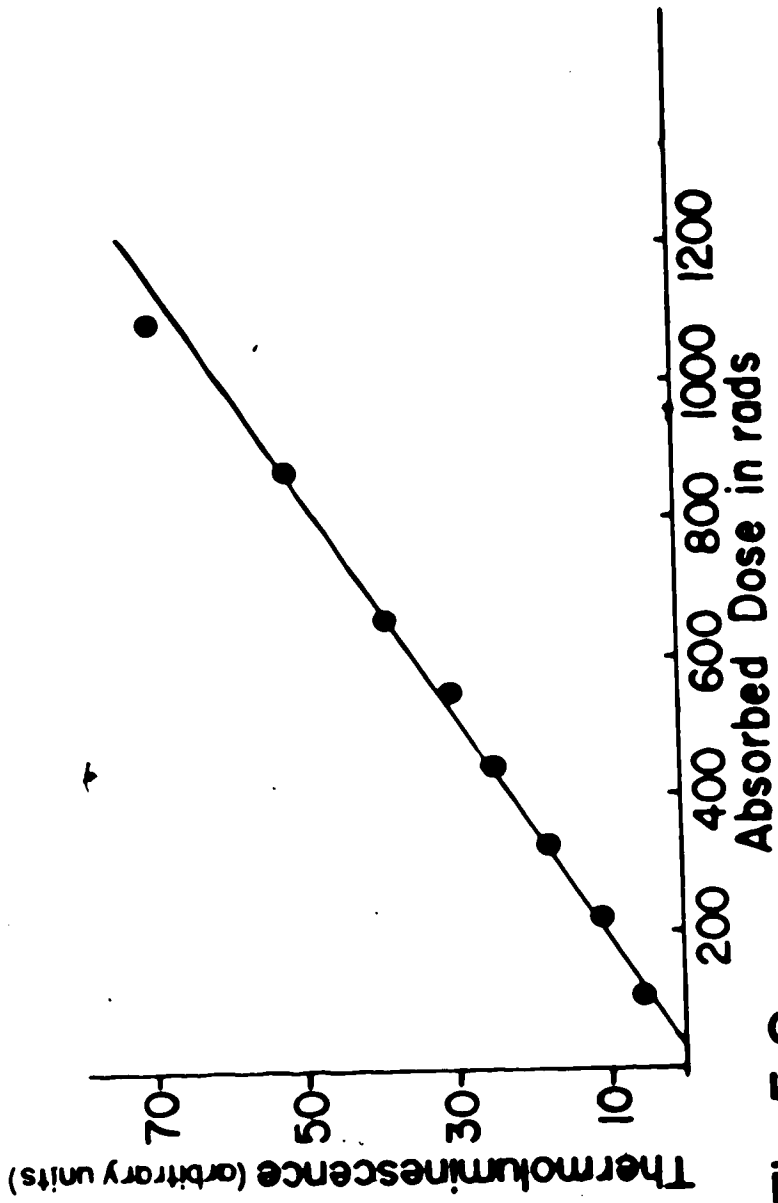
Fig.5.2 ___ Linear response of TLD-100

ten diameters or more and the irradiated area of the scatterer
had always a finite size.

In order to determine the experimental uncertainty measurements
were obtained at 1 cm outside the beam and with no scatterer, prior
to every experiment. The standard deviation over these measurements
was found to be $\pm 1.3\%$. This includes uncertainties due to beam
instability, field definition reproducibility of the experimental
arrangement and random instrumental errors. Some additional
uncertainty in the dose measurements is involved when positioning the
scatterer in the beam. Calibration of the ionization chamber and
pressure and temperature correction were not necessary, since only
relative absorbed dose was measured.

5.3 EXPERIMENTAL RESULTS

5.3.1. The Absorption Characteristics of the Scattered Radiation

The absorption characteristics of the radiation arising in the
scattering material was determined by obtaining its depth dose
distribution in the phantom. This was measured at points outside
the field and for two different positions of the scatterer in the
beam. The curves shown in figure 5.3 for 8 MV and 6 MV x-rays are
normalized to 100 % maximum absorbed dose, which occurs at the
surface. The rapid fall off region suggests the penetration of
thick absorbers by high energy electrons. The flat portion of the
curves is due to the presence of scattered radiation from within
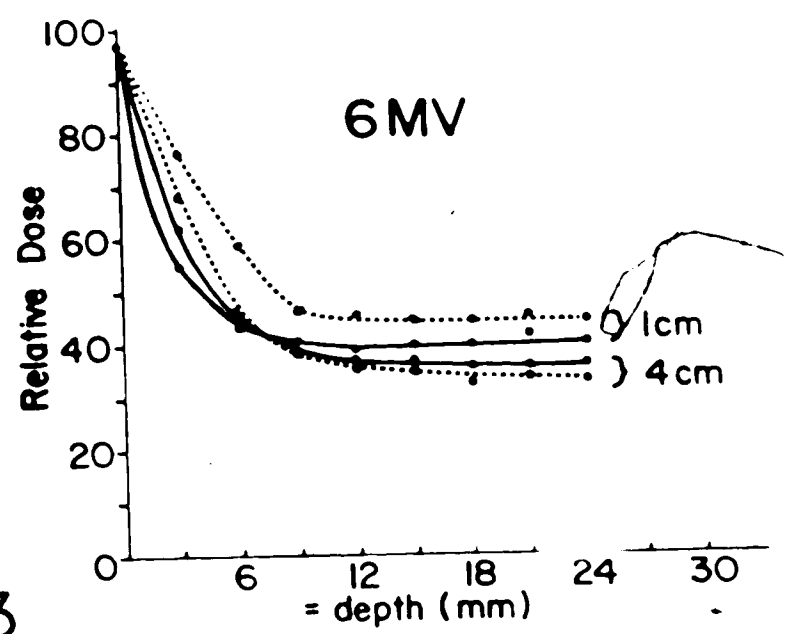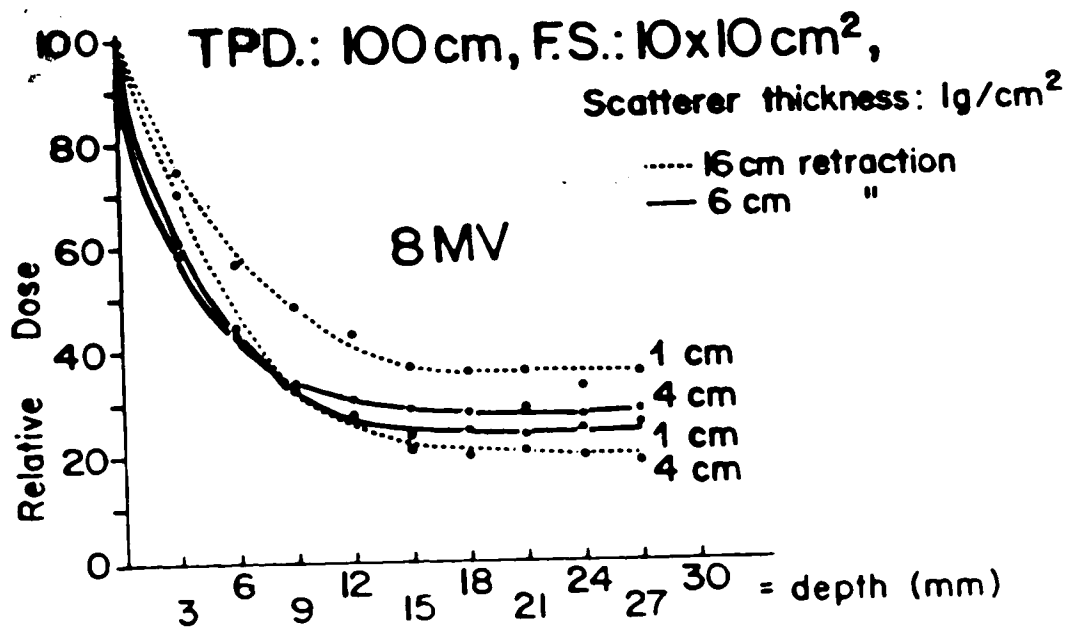
Fig.5.3

Penetration pattern for scattered radiation
outside the beam.

the phantom.

Although the energy distribution of the scattered electrons cannot be obtained from these data, the curves allow for estimation of their mean energy, by evaluating the mean electronic range. This range corresponds to the penetrated thickness of the phantom before the absorbed dose drops to 50 % of its maximum.

The nature of the exponential dose fall-off is very similar for both beam energies and retractions. The mean range is found in the neighbourhood of 5 mm in tissue which corresponds to an energy of 3 MeV.

5.3.2. The Distribution of Scatter Outside the Beam

A. Open Beams

The distribution of the in-air scatter as a function of distance outside the beam, for 8 MV and 6 MV x-rays is shown in figure 5.4. These data are plotted for small and large fields and for a target to phantom distance (TPD) equal to 100 cm. The intensity of the scattered radiation can be seen to decrease as the distance from the edge of the beam increases. For the 6 MV x-rays, the dose at 1 cm outside the field edge reaches a value of as much as 14 % of the mid-field maximum dose, when a large field is employed. The term "mid-field-maximum" in this text refers to the dose at the equilibrium dept, d_{max} , in the phantom for a given set dose in the center of the field.

126
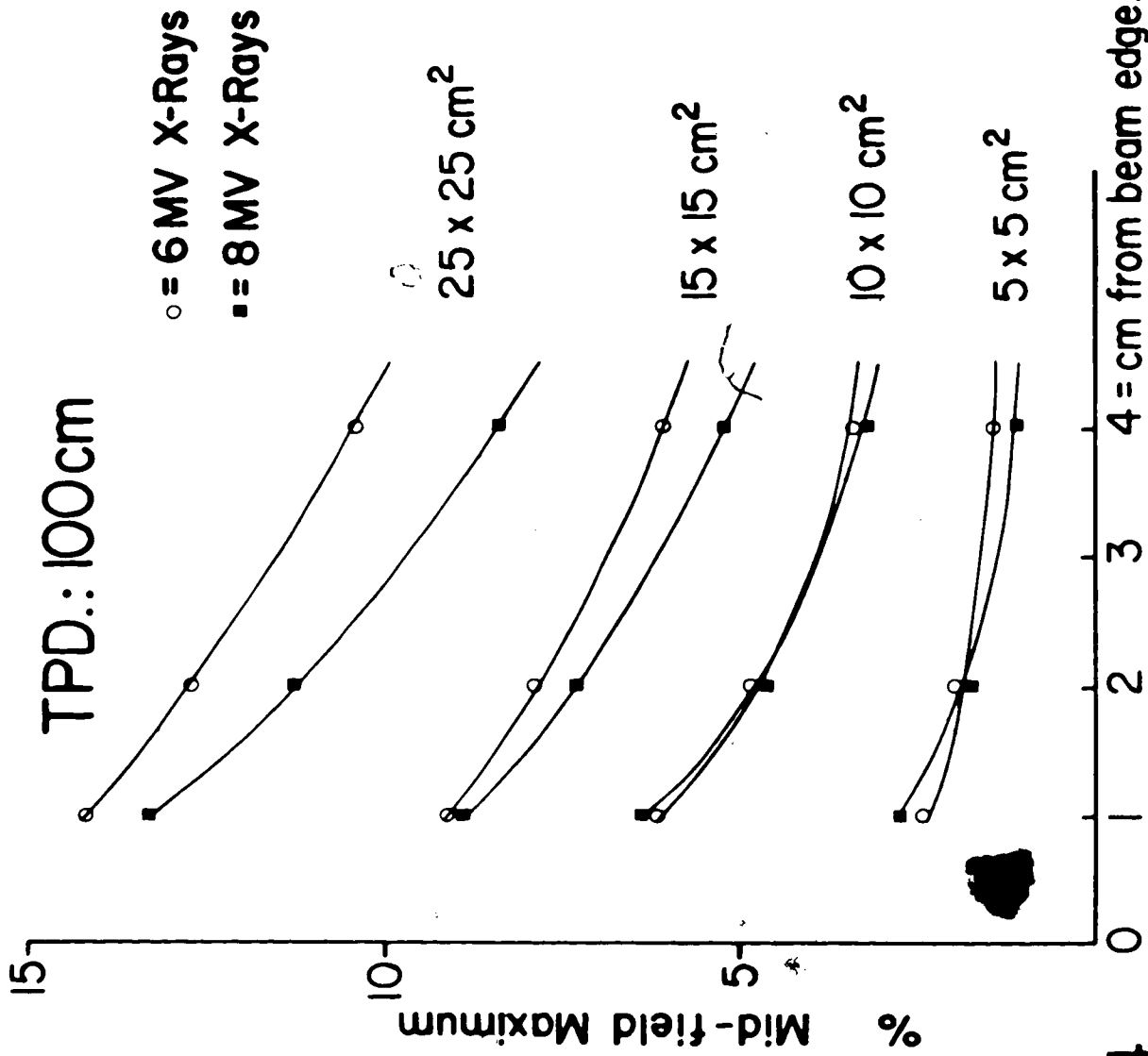
Fig.5.4

In a preliminary measurement, the amount of penetration through the collimators was found to be minimal (0.2 % of the mid-field-maximum) and well below the experimental error. It can therefore be stated that the dose to the points of measurement is exclusively due to scattered radiation arising in the collimators and the intervening air space and to those electrons and low energy photons that emerge onto the surface after suffering multiple scattering within the irradiated volume of the phantom.

The magnitude of the scattered radiation increases substantially with field size as expected since both sources of scattered radiation will increase in size. The plotted data also demonstrate that in air the lower energy photon beam gives rise to scatter at preferentially larger scattering angles, that is, at greater distances from the beam edge. The negative slope of the fall-off is generally steeper for the 8 MV beam, while the magnitude of scatter at points M is not very different from that of the 6 MV beam for small fields and this magnitude becomes smaller for larger fields, where the mean scattering angles defined for points outside the beam are increased.

B. Distributions at the Presence of a Scatterer

Introduction of a scattering material in the primary beam gives rise to an additional scatter component. The dose on the surface of the phantom was measured at varying lateral distances up to 10 cm. from the field edge. Slabs of a high Z material (lead) and a low Z material (wax) 1 g/cm^2 thick, were separately placed in a $(10 \times 10)cm^2$

field at 6 cm. and 16 cm. from the surface of the phantom. During these measurements the scatterer was positioned as shown in figure 5.1 extended over the entire field, but not beyond its edges. The radiation intensity profiles outside the field, shown in figure 5.5, for the two beams, reveal a large increase in the absorbed dose at the points under discussion, which falls rapidly as the detector is moved away from the beam edge out to around 4 cm. After this point the decrease becomes more gradual, the distributions slowly approaching that of the in-air scatter.

The thickness of the scattering slab did not appear to be a significant factor. A 2% increase in the amount of scattered radiation occurred initially but beyond about 3 gm/cm^2 there was no further increase.

The irradiation field during operation was symmetrical in all directions with a maximum permissible variation of $\pm 3\%$ of the dose at the center of the field and at the equilibrium depth. In order to ensure that this size of variation in the radiation intensity across the field would not affect the measurement of scatter, similar distributions were obtained at all four sides of the field. It was found that the distributions were reproducible within the experimental error. The data presented were obtained for points at variable distance from the field edge and in one direction only. However, it is directly applied to all corresponding points around the field.

The magnitude of the scattered radiation generally increases with field size. The distribution of scatter from a wax scatterer
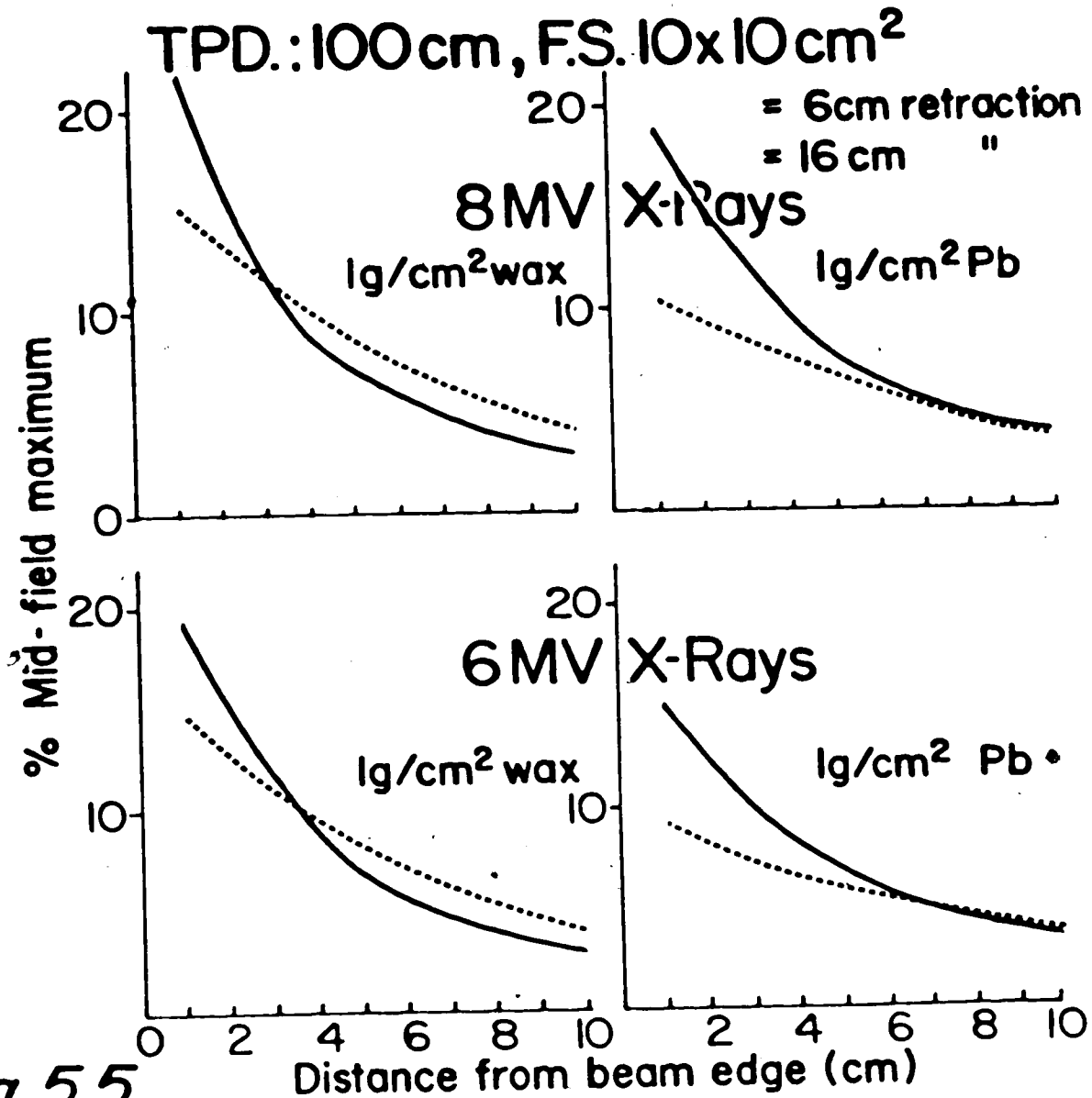
Fig. 5.5 *Scatter distribution as a function of distance from the beam edge.*

.is shown in figure 5.6 for small and large fields and for two retractions. While the in-air scatter increases uniformly with field size, the same is not true in the presence of a scatterer. Indeed, the absorbed dose at the points of interest initially increases rapidly as the irradiation field increases, but for larger fields the dose increase occurs at a slower rate. This suggests that the scattered radiation reaching the detector arises predominantly from one section of the scatterer, rather than its entire irradiated volume.

For small fields, the dose to the points of interest is generally reduced when the scatterer is moved away from the phantom surface. However, the fall-off with distance from the field is slower and, as a result, for points sufficiently distant and for large fields the effect reverses. For very large fields the magnitude of scatter at all points becomes higher when the longer retraction is used.

Figure 5.7 illustrates how the magnitude of scatter changes with retraction. Generally, the surface dose at the various points outside the beam is seen to initially increase with retraction, reaching a maximum value for a particular separation distance between the scattering slab and the phantom. This distance is different for every point and changes with field size and beam energy. Beyond this value the dose falls continuously with increasing retraction up to 30 cm. from the phantom, which is the maximum possible retraction at 100 cm TPD due to restrictions on the
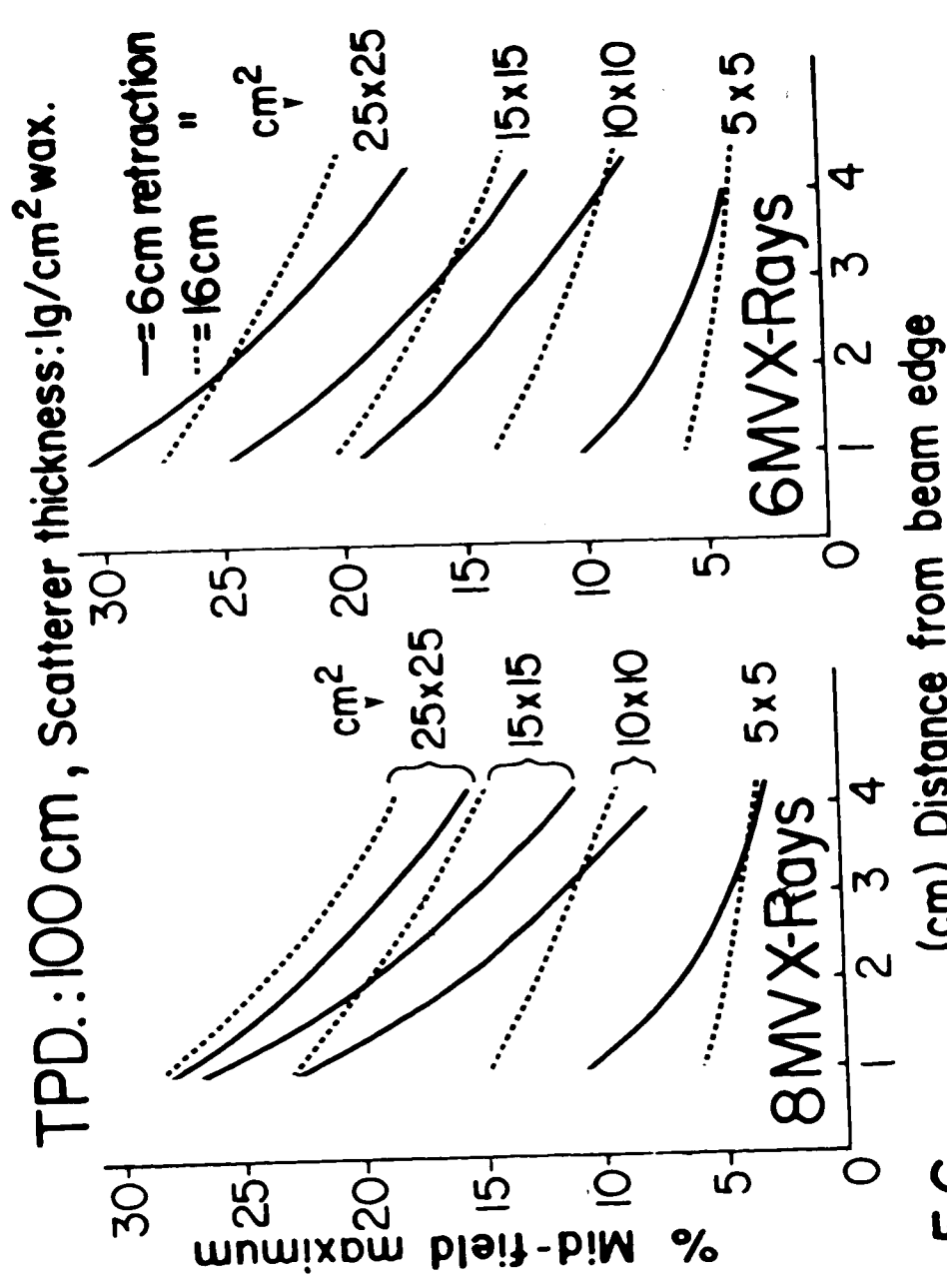
Fig.5.6 Variation of the scatter distribution with field size.
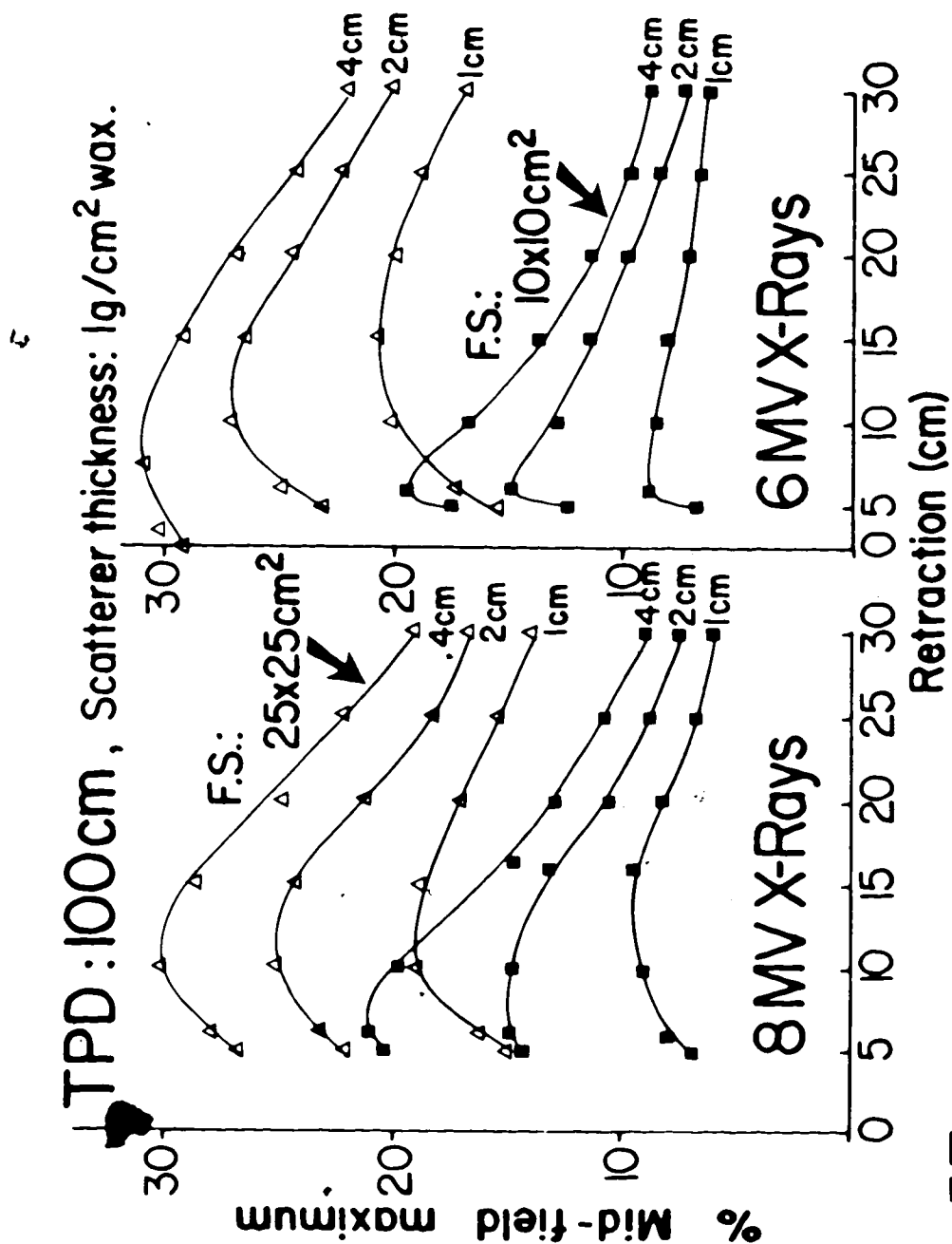
Fig. 5.7 — *Variation of scatter as a function of retraction.*

distance between the machine head assembly and the surface of the phantom. Similar measurements were obtained for an extended TPD and for a single field size. In figure 5.8 the magnitude of scatter is seen to remain constant for all retractions greater than 40 cm.

The effect of the scatterer positioning in the beam was examined by laterally moving the scattering slab, so that a gap was created between the edge of the field and that of the scatterer. The measuring probe was left fixed at one centimeter outside the beam and the scatterer was displaced by 1 cm. intervals. These results are shown in figure 5.9 for a 10 x 10 cm field and a TPD of 100 cm. The magnitude of the scattered radiation falls continuously as the scatterer is drawn from the edge of the field, until at about 5 cm from the edge, it reverts to that for the open beam. This clearly demonstrates the fact that only part of the scattering area contributes significantly to the increase of the dose, absorbed at points outside the field.

The dependance of scatter on the composition of the scattering material is shown in Tables II and III for high, medium, and low atomic number scatterers of equivalent thickness. A higher scatter effect is generally observed with the lower Z materials for both beams. However, this effect appears to reverse for the 8 MV beam, when the point of interest lies at a distance equal to, or greater than, 4 cm from the field edge. It was anticipated that these results reflect the variation of the angular distribution of scattered radiation with atomic number of the scattering material. An
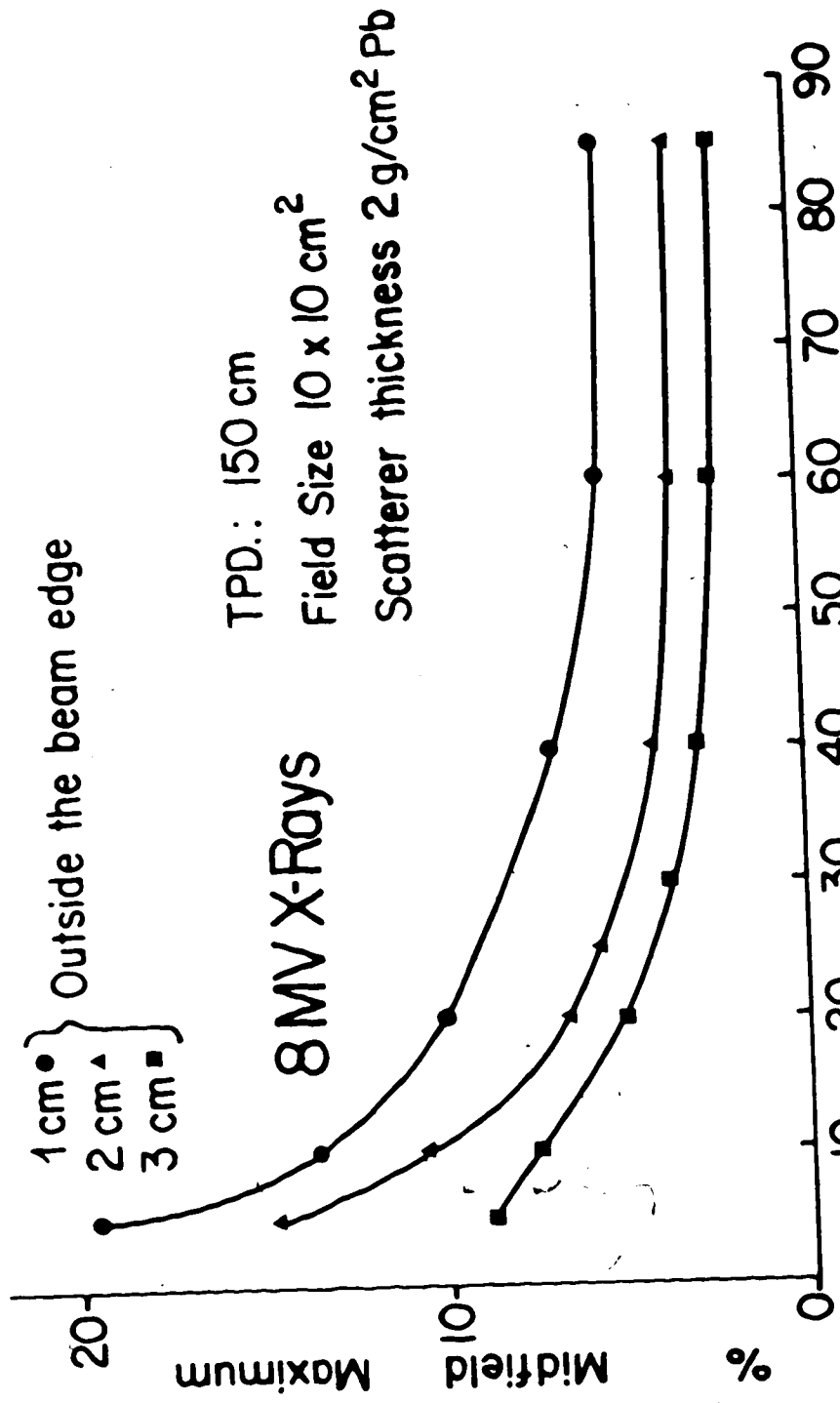
Fig. 5.8

Scatter distribution as a function of retraction for an extended TPD.

135

TPD : 100cm , F.S.: 10×10 cm^2

Scatterer thickness :
..... = 1g/cm^2 wax
——— = 1g/cm^2 Pb.

6 MV X-Rays

8 MV X-Rays

30

20

10

% Mid-field maximum

0 1 2 3 4 5

(cm)   Distance of scatterer from beam edge.
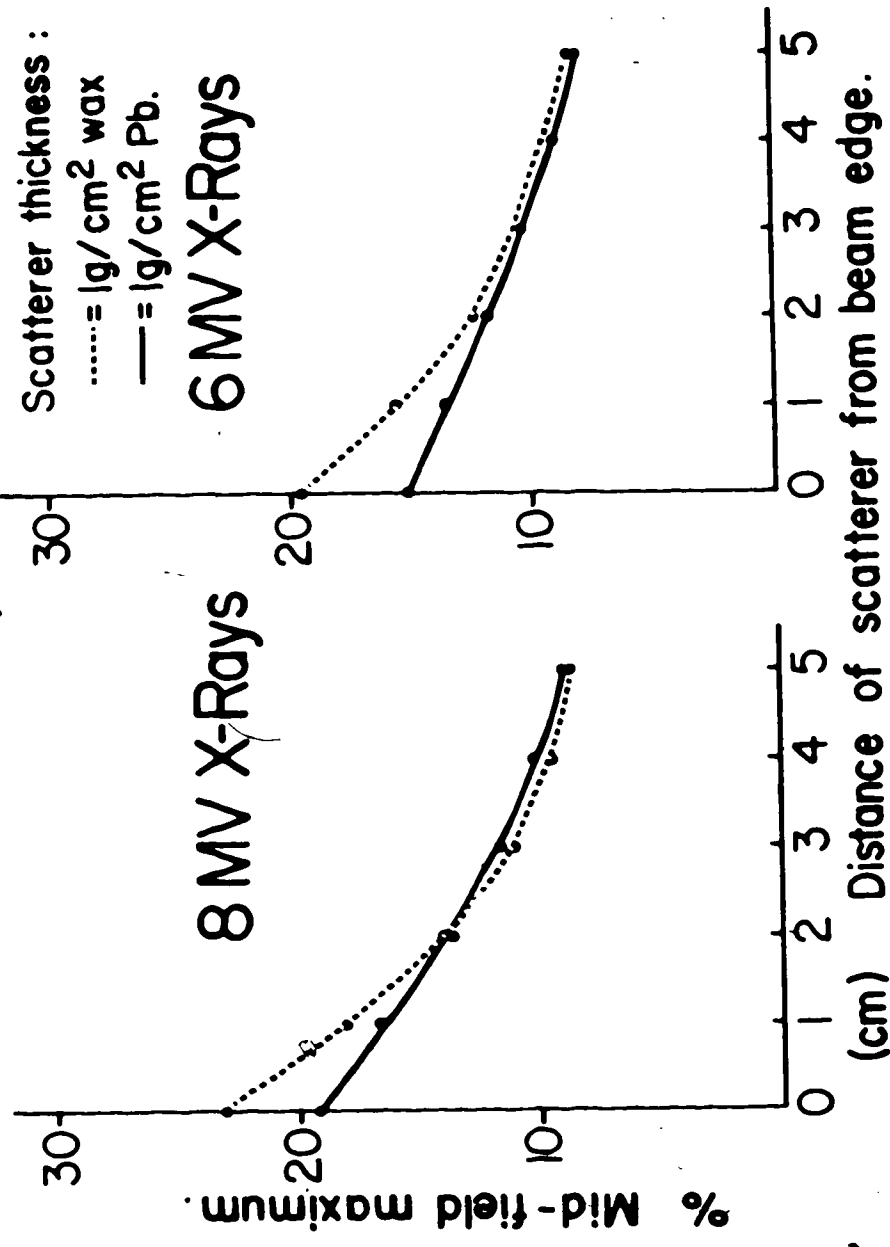
Fig.:5.9 —— *Effect of position of scatterer within the beam.*

TABLE II

Scattering Material	Z	PER CENT MID-FIELD MAXIMUM DISTANCE OUTSIDE BEAM EDGE					
		6 cm Retraction			16 cm Retraction		
		1 cm	2 cm	4 cm	1 cm	2 cm	4 cm
Wax	6	23.0	16.0	8.0	14.8	12.9	9.7
Aluminum	13	20.8	15.6	8.8	13.0	11.1	8.1
Lead	82	19.0	14.2	8.9	10.2	9.1	7.3

8 MV x-rays

Field Size: 10 x 10 cm^2

TPD: 100 cm

Scatterer Thickness: $1g/cm^2$ of wax

TABLE III

Scattering Material	Z	PER CENT MID-FIELD MAXIMUM DISTANCE OUTSIDE BEAM EDGE					
		6 cm Retraction			16 cm Retraction		
		1 cm	2 cm	4 cm	1 cm	2 cm	4 cm
Wax	6	19.4	15.2	9.0	13.8	11.9	8.9
Aluminum	13	18.1	14.0	8.5	11.5	10.1	7.8
Lead	82	14.9	11.7	7.9	9.1	7.9	6.2

6 MV x-rays

Field Size: 10 x 10 cm^2

TPD: 100 cm

Scatterer Thickness: 1 g/cm^2 of wax

experiment was thus designed to measure the amount of scatter as
a function of scattering angle for a low and a high Z absorber.
The distance between the probe and the scatterer was kept constant,
and equal to 5 cm from the center of the field. Measurements were
then performed for a number of angles between 0° and 180° relative
to the beam axis. A "pencil field" 2 x 13 cm^2 was chosen, rather
than a square one, in order to facilitate mean angle definition.
The obtained distributions can be seen in figure 5.10. Minimal
amount of backscattered radiation reaches the probe when a wax
scatterer is used, while the forward scatter contribution is
significant in magnitude, although less than that in the forward
direction. For all positive scattering angles the amount of
scatter arising in the low Z scatterer is seen to exceed that arising
in an equivalent thickness of the heavier material.

5.3.3. Scattered Radiation From a Cobalt-60 Beam

The data presented provide very little information about the
dependance of the scatter found outside the field on the energy of
the photon beam. Indeed, comparison of the scattering properties
of the two high energy beams does not reveal basic differences.
General observations suggest that there is a tendency for scatter
at wider angles with the 6 MV beam, while at small scattering angles
the surface dose remains lower compared to that from the 8 MV beam.
However, these effects are small in magnitude and the nature of the
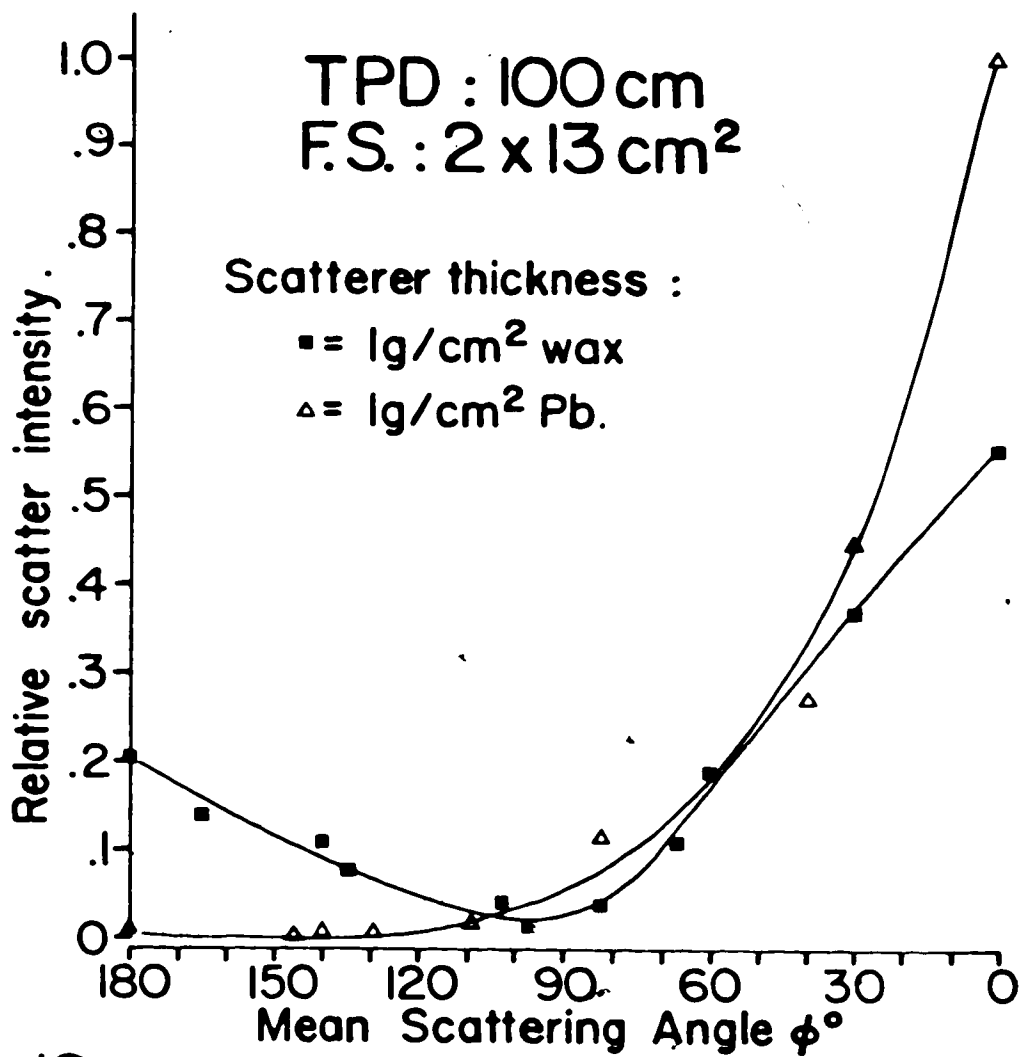scatter distribution as well as the energy of the scattered electrons

Fig.10

—— Angular distribution of scattered radiation for high & low Z scatterers.

are not very different. The fact is not surprising, considering
that both the 8 MV and the 6 MV x-ray beams are characterized by
energy spectra with energies varying continuously from very low
values up to their nominal energies.

In order to investigate the dependence of the scatter effects
on beam energy, a number of measurements were made using the γ-ray
beam from a Cobalt-60 teletherapy unit (Theratron 80). The basic
difference between the Cobalt-60 beam and the above x-ray beams
lies in the fact that the ^{60}Co isotope emits a discrete spectrum of
energies rather than a continuous one, with two peaks occurring at
1.17 MeV and 1.33 MeV.

The penetration pattern of the scattered radiation from a
wax scatterer is shown in figure 5.11 for a point 1.5 cm outside
the beam edge. The mean range of the scattered electrons is about
considerably smaller than that for the linac beams. This range
corresponds to electrons with predictably lower energy of approximately
50 KeV.

In spite of the much lower energy carried off by the ^{60}Co
scattered radiation, the distributions of scatter outside the beam
are not very different than those of the x-ray beams. These are
shown as a function of distance from the beam edge in figure 5.12
and as a function of retraction in figure 5.13. While the in air
scatter for Cobalt-60 is somewhat higher indicating a lower energy
beam, the distributions for high, medium, and low Z scatterers do
not reveal essential differences. In general terms,the magnitude
of scatter for identical experimental arrangements is found to be
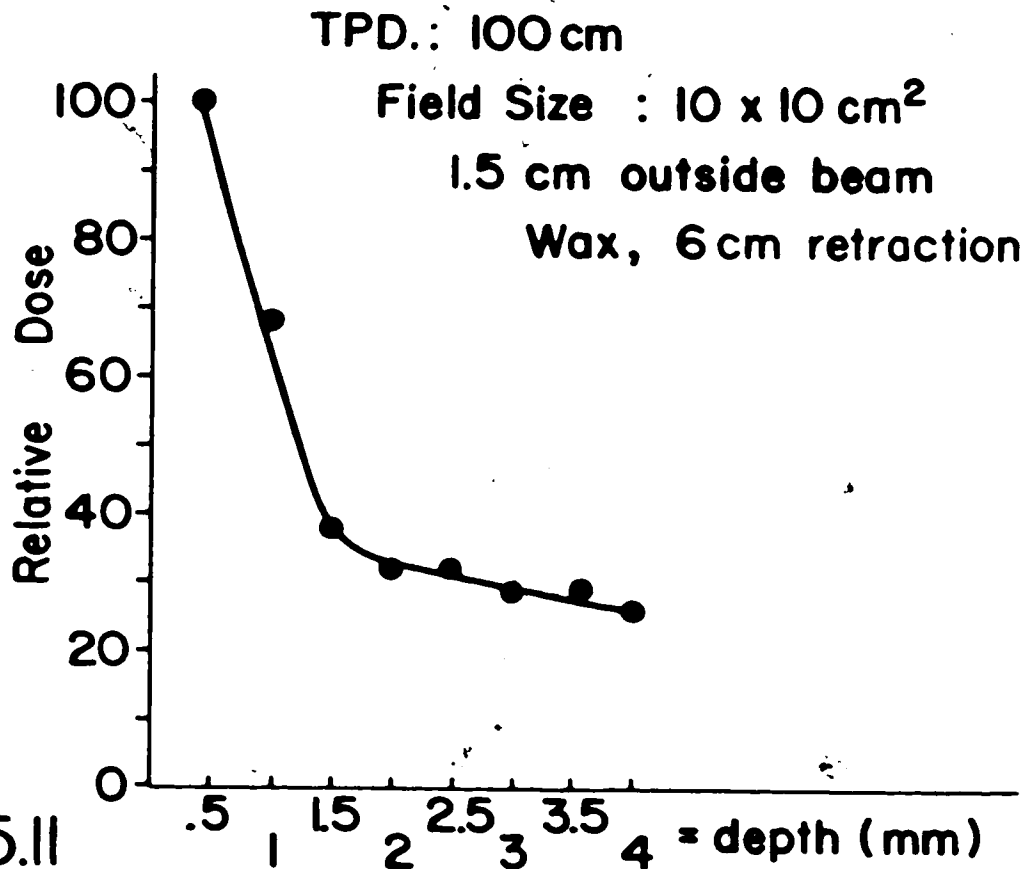
Fig. 5.11

Penetration pattern for scattered radiation outside the ^{60}Co γ-ray beam.
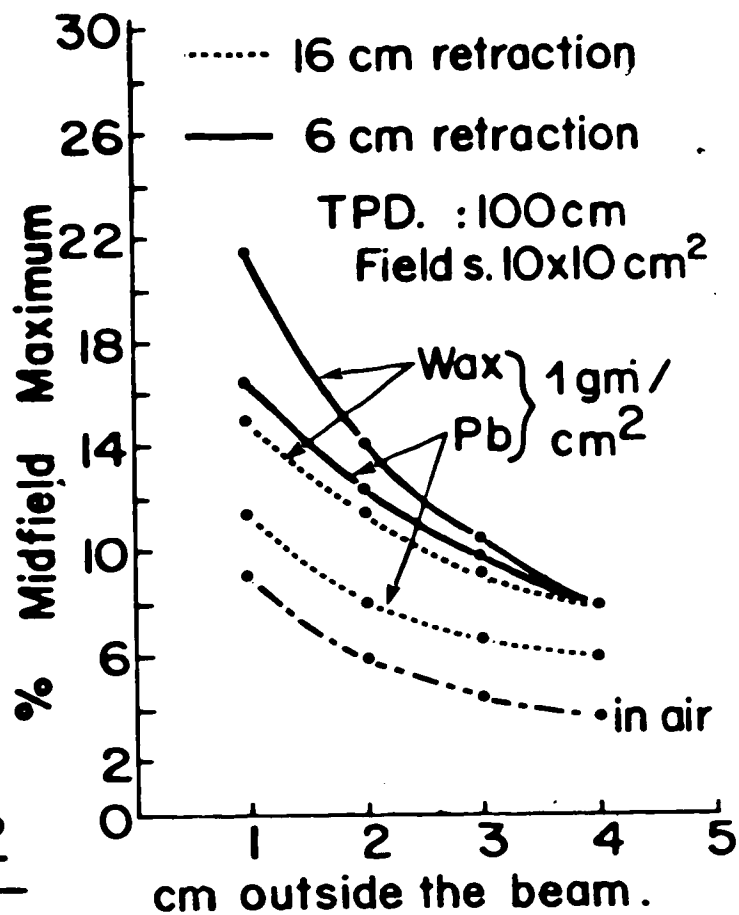
Fig. 5.12

Distribution of scatter as a function of distance from the beam edge for the ^{60}Co γ-ray beam.
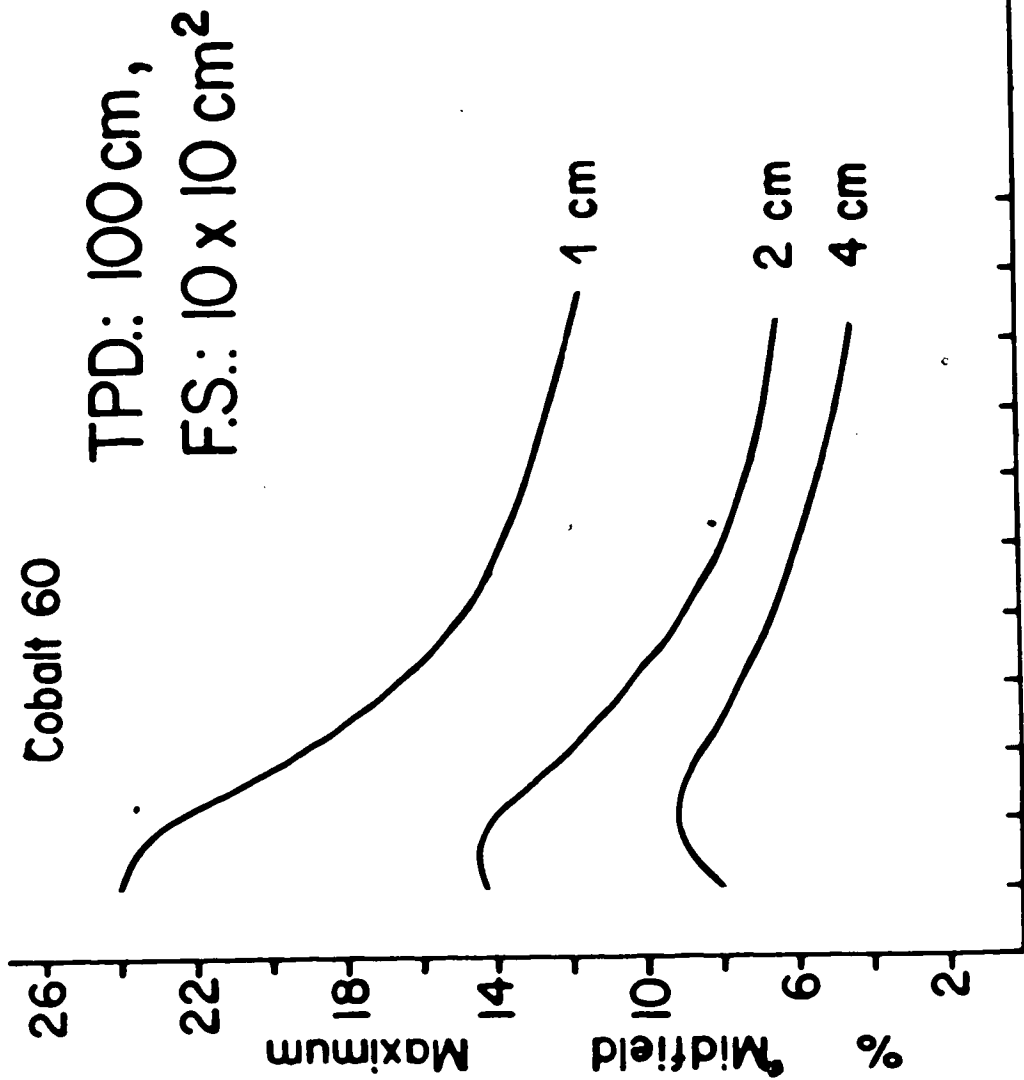
Fig.5.13 — Variation of scatter with retraction in ^{60}Co γ-ray beam.

TABLE IV

Scattering Material	Z	PERCENT MID-FIELD MAXIMUM DISTANCE FROM BEAM EDGE					
		6 cm Retraction			16 cm Retraction		
		1 cm	2 cm	4 cm	1 cm	2cm	4 cm
Wax	6	22.0	14.0	7.8	15.0	11.5	7.8
Aluminum	13	20.5	13.5	7.9	13.0	9.5	6.8
Lead	82	17.5	12.2	7.5	11.5	7.8	5.9

^{60}Co γ-rays

Field Size : 10 x 10 cm^2

TPD : 100 cm

Scatterer Thickness : 1 g/cm^2

essentially the same for all three beams.

5.4   DISCUSSION OF RESULTS

a.   Geometrical factors

The nature of the scatter distributions as a function of retraction and distance from the beam edge is essentially determined by geometrical considerations. The measured intensity of the radiation reaching each point is a function of the following factors:

(i) The mean scattering angle, defined by the beam axis and the straight line between the center of the scattering area Δa and the point of interest (figure 5.14). This angle decreases with increasing retraction and increases with lateral distance from the beam edge. For any particular beam energy and scattering material it determines the total emission probability in the direction it defines.

(ii) The distance "R" of the point of interest from the source of scattered radiation; this distance is also a function of both retraction and distance from the beam edge. It determines the amount of attenuation of the scattered radiation in the intervening air space. However, this attenuation is very small for all the geometries used. A 1 MeV electron has a mean range of 4.5 g/cm^2 in air, equivalent to a distance of approximately 6m.

(iii) The solid angle $d\omega$ defined at each point by the

Beam axis

Δa

R

φ

dΩ

r

M

Phantom
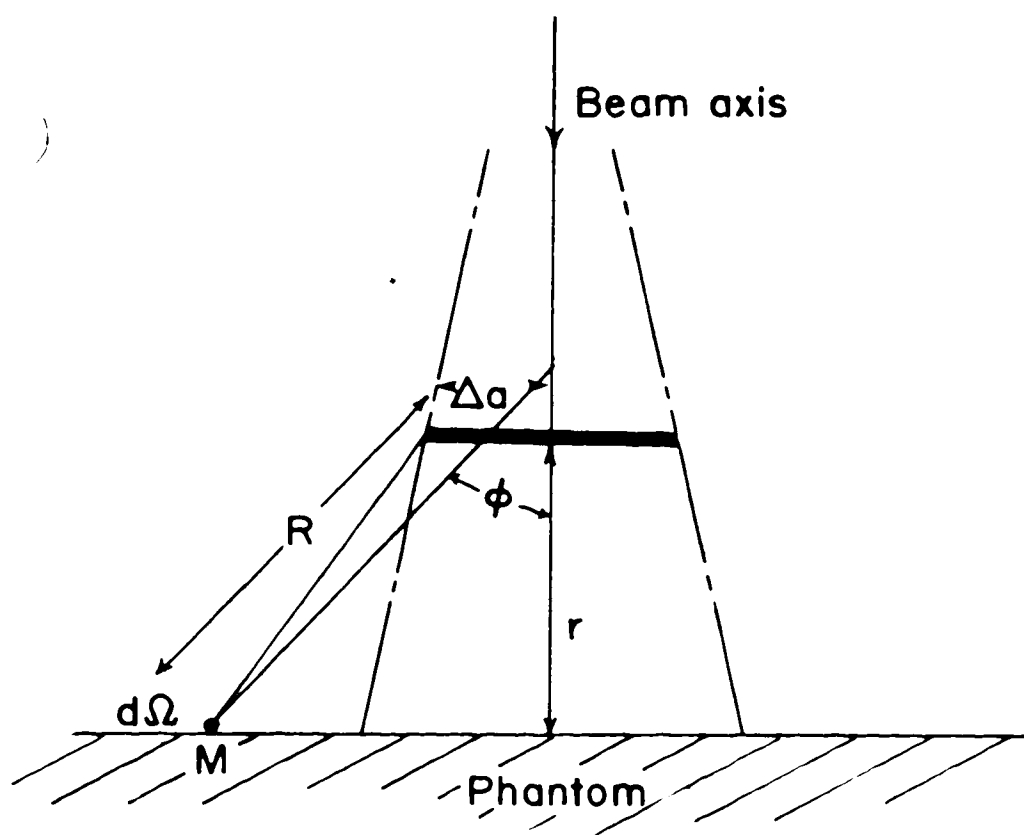
Fig. 5.14

Experimental geometry

scattering area on the surface of the scatterer Δa and the position in space of the particular point. This solid angle describes the volume accepting the emitted scattered radiation Its magnitude varies extensively with the different geometries.

b. Interactions within the scatterer

The Compton scattering theory predicts that the electronic scattering cross-section is independent of the atomic number of the absorber. In addition, electrons generated during Compton events will be scattered at any angle between 0° and 90°, but none will be backscattered. These theoretical predictions are in good agreement with experimental data for photons incident on gases or thin absorbers. When the thickness of the absorber becomes comparable to, or greater than the recoil electron range in that material the scatter distribution is significantly altered (Hine, 1952). This is the case with the data presented in the previous section, where the Z dependence, as well as the existence of probable backscattering angles can not be explained in terms of single Compton scattering processes. In thick absorbers the secondary electrons will undergo multiple nuclear scattering and will emerge from the surface at some angle different from their initial direction. In addition, while traversing the absorber they will suffer a number of collisions with atomic electrons. The absorber then becomes a source of secondary electrons which undergo interactions like any negatron.

The total nuclear scattering cross-section is proportional to $\frac{N_0 \rho Z^2}{A}$ where $\frac{N_0 \rho}{A}$ is the number of atoms per cubic centimeter in the absorber. Similarly, the energy transferred from the electrons to the medium through ionization is proportional to $(N_0 \rho/A)Z$. Consequently, the total scattering probability is proportional to $\frac{N_0 \rho}{A} (Z^2 + Z)$ or $Z/A \ (Z + 1)$. Therefore, while the number of the generated electrons is independent of the composition of the absorber, the emission at any angle is a function of Z.

In low Z absorbers, the amount of nuclear scattering and radiation and ionization losses is too small to seriously affect the expected results. The mean range of the secondary electrons will not be altered and the scattering events are predominently Compton interactions. In higher Z materials, the electronic range is reduced due to enhanced scattering cross-sections and increased energy losses. As a result equivalent thicknesses in g/cm^2 of low and higher Z absorbers will give rise to differing scatter intensities. Also in high Z absorbers a large number of secondary electrons will be absorbed before reaching the surface if the thickness is greater than the electronic range. Since the number of generated electrons through Compton interactions is independent of the atomic number of the material, backscattering in high Z absorbers further reduces the amount of the scattered radiation emitted in the forward direction.

In figure 5.10 the intensity of backscatter is negligible for the low Z scatterer (wax) but becomes considerable when a high atomic number material is used. Due to the multiple nuclear

scattering in lead, exit angles greater than 90° become probable.

The backscattered electrons are degraded in energy and few in

number and the magnitude of the backscattered radiation is small

compared to that in the forward direction. This is expected since

Compton electrons are predominently scattered at shallow angles.

The only electrons that will be backscattered are the ones that

suffered a large number of deflections in the fields of the

atomic nuclei.

c. The energy dependence.

The intensity of the scattered radiation measured at points

on the surface of the phantom is a function of both the energy

of this radiation and the total emission of multiply scattered

electrons at the particular angle. The mean energy of the scattered

radiation from the Cobalt-60 beam was found to be approximately 350

keV, while the energy was in the neighbourhood of 3 MeV for the

higher energy x-rays. This ten-fold difference in energies is

in fact predictable. The energy that an electron acquires during

a single Compton collision with a 1.25 MeV photon, has a maximum

value of approximately 1 MeV, when the photon scattering angle

is 180°. In the case of the 6MV and 8MV x-rays, the ejected

electrons can acquire considerably higher energies through

collisions with the higher energy photons in the beam. On the other

hand the theory of Compton scattering in low density absorbers

predicts that the Klein-Nishina scattering cross-section for recoil

electrons increases with decreasing photon energy for angles greater than around 10^{0} (Nelms, 1953). The total emission of secondary electrons from high Z absorbers is also a function of energy, decreasing as the energy of the incident photons is increased (Hine, 1952). Therefore while the energy of the scattered radiation obtained with the Cobalt - 60 beam is much lower than that for the linac beams, the probability of emission at wide angles is increased.

The intensity distributions of scatter expressed as a percentage of the mid-field maximum for each of the three beams were not found to be substantially different. However the information provided by the reported data does not permit direct comparison of the scattering characteristics of the three beams on the basis of their energies alone. When comparing beams obtained from different radiotherapy machines, the design and construction of the treatment head is an important factor, especially when the properties of the beams in the build-up region are to be considered. It has been shown that both the surface dose and the depth of maximum absorbed dose are dependent on the target and the flattening filter used with medical linear accelerators (Rawlinson et al., 1973; Gray, 1973). The design of the collimation system and the size of the source (or focal spot on the target) predetermine the amount of electron contamination present in the beam and the extent of the penumbral area around the field edges. These factors should thus be taken into consideration.

The "Theratron 80 " unit employs a ^{60}Co source 1.75 cm in diameter. The diaphr_gm (collimator) is placed at 45 cm from the source. Small penumbra would be obtained using a small size source and a long source-to-diaphragm distance (figure 1.2). However, a small source is impractical as the activity is decreased. Also there is a limit in the source-to-diaphragm distance since for large distances the scattered radiation arising in the collimator will reach the patient. Thus the source-collimator arrangement is a compromise between these two extremes. In the linear accelerators, the small size of the focal spot on the target permits small target to collimator distances and therefore the surface scatter is minimized.

The in-air scatter distribution for Cobalt-60 is considerably higher than that for both the linac beams. Also in figure 5.13 the magnitude of scatter is unexpectedly high at 1 cm outside the beam and drops rapidly as the probe is moved out to 2 cm. These effects are mainly attributable to the design of the treatment head and, to a lesser extent, to the differing beam energies.

For clinical applications it is more appropriate to express the surface dose as a percentage of the dose delivered to the target volume, rather than that at d_{max}. In Table V some of the previously reported data is shown, expressed as a percentage of the dose at a depth of 10 cm in the phantom. For the same dose delivered at this depth and for identical experimental parameters, the magnitude of the surface scatter from t·· Cobalt-60 beam exceeds that ing from the high energy x-ray beams.

<u>TABLE V</u>

PERCENTAGE DEPTH DOSE AT d=10 CM

DISTANCE OUTSIDE BEAM EDGE

	6 cm retraction			16 cm retraction		
	1 cm	2 cm	4 cm	1 cm	2 cm	4 cm
^{60}Co γ-rays	38.1	24.2	13.5	26.0	19.9	13.5
6 MV x-rays	28.9	22.6	13.3	20.6	17.8	13.3
8 MV x-rays	32.4	22.5	11.3	20.8	18.2	13.5

F.S. 10x10 cm^2

TPD 100 cm

scatterer 1g/cm^{2}wax.

CHAPTER VI

CONCLUSIONS

The large magnitude of the scattered radiation a few
centimeters outside the beam, arising from beam modifying
devices can, under some circumstances, be a cause for concern.
The surface dose 1 cm outside the beam can reach as much as
30 % of the maximum absorbed dose at the center of the field,
for large fields. For the higher energy beams, the scattered
radiation is of sufficient energy to penetrate to a significant
depth in tissue. This dose amounts to a few hundreds of rads
of dose absorbed by the anatomic site immediately neighbouring
the field, when the total surface dose received during the entire
course of treatment is considered.

The magnitude of the scattered radiation within 4 cm from the
field edge can be reduced by using high atomic number materials,
whenever possible. At any greater distances from the beam edge,
high and low Z scatterers give rise to similar radiation intensities,
due to the particular nature of scattering in high Z materials.

The character of the scatter distributions depends to a
great extent on the geometry of the experimental arrangement.
As a result, it appears that very short retractions would give
minimum surface dose outside the field. Such retractions cannot
be employed since, as published data indicates, severe electron

contamination can occur in the irradiated area. In general,
retractions greater than 20 cm will improve skin sparing outside
the beam edges and the maximum retraction is determined by
considerations of the relative skin dose within the field.

The amount of scattered radiation outside the field was
found to decrease rapidly as the scatterer was withdrawn from
the beam edges. This suggests that tissue compensators and
shields, when placed away from the edges do not largely contribute
to the scattered radiation outside the field. However the use
of extended scatterers i.e., filters and supporting trays for
beam shaping devices may still lead to difficulties . In any
case, when the field is defined within a few centimeters from
superficial radiosensitive structures, the dose due to scattered
radiation arising from scatterers in the beam should be monitored
and appropriately placed absorbers outside the beam can be used to
attenuate the scatter when necessary.

BIBLIOGRAPHY

ATTIX, F.H. (1967)   Basic x-ray dosimetry. Health Physics 15: 49.

BAGNE, F. (1974)   Physical aspects of supervoltage x-ray therapy. Medical Physics, Vol. 1, No. 5: 266

BICHEL, H. (1968)   Charged particle interactions. In Radiation Dosimetry, Vol. I. Edited by Attix, F.H., Roesch, W.C. Academic Press, New York-London, p. 157.

BOAG, J.W. (1966)   Ionization chambers. In Radiation Dosimetry, Vol. II.Edited by Attix, F.H. Roesch, W.C. Tochilin, E. Academic Press, New York-London, p.2.

BOLAND, J. (1957)   Human skin reaction. Brit. J. Radiol, 30:351

BRITISH JOURNAL OF RADIOLOGY (1972) Supp. 11 Central axis depth dose data for use in radiotherapy. Edited by Cohen, M. Jones D.E.A., Greene, D. London.

BURLIN, T.E. (1968) Cavity-ionization theory. In Radiation Dosimetry, Vol. I. Edited by Attix F.H., Roesch, W.C., Academic Press, New York - London, p.382.

CAMERON, J.R., ZIMMERMAN, D., KENNEY, G., BUCH, R., BLAND, R., GRANT, R.(1964) Thermoluminescent radiation dosimetry utilizing LiF. Health Physics 10: 25

CUNNINGHAM, J.R. (1972) Scatter - Air- Ratios. Phys. Med. Biol. 17, No. I: 42

DUTREIX, J., DUTREIX, A., TUBIANA, M. (1965) Electronic equilibrium and transition stages. Phys. Med. Biol. 10: 177

EDELSACK, E.A., KREGER, W.E., MALLET, W., SCOFIELD, N.E. (1960) Experimental investigation of thick target bremsstrahlung radiation produced by electrons of 1.00, 1.50 and 2.00 MeV. Health physics 4:1

ENVIRO-MED. INCORPORATED (1969) Report MPD-12. Specifications for a microwave linear accelerator for radiotherapy.

EVANS, D.R., (1955) The atomic nucleus. Edited by the McGraw-Hill Book Company, Inc., New York-Toronto-London.

EVANS, D.R., (1968)   X-ray and γ-ray interactions.   In <u>Radiation</u>
<u>Dosimetry</u>, Vol. I.   Edited by Attix F.H.,
and Roesch, W.C., Academic Press, New York-
London. p.94

FITZGERALD, J.J., BROWNELL, G.L., MAHONEY, F.J. (1967) <u>Mathematical</u>
<u>Theory of Radiation Dosimetry</u>. Edited by
the Gordon and Breach Science Publishers Inc.,
New York-London-Paris.

FOWLER, J.F., ATTIX, F.H. (1966)   Solid state integrating
dosimeters.   In <u>Radiation Dosimetry</u> , Vol. II.
Edited by Attix, F.H., Roesch, N.C., Tochilin, E.
Academic Press, New York-London, p. 241.

GAGNON, W.F., GRANT III, W.(1975). Surface dose from megavoltage
therapy machines.   Radiol. 117: 705

GRAY, L. (1973)   Relative surface doses from supervoltage
radiation.   Radiol. 109: 437.

HAYBITTLE, J.L. (1955) Physical requirements of beam defining systems
for medium distance teletherapy units.   Acta
Radiologica 44: 505.

HENDEE, W.R. (1966)   Thermoluminescent dosimetry of beta depth
dose.   Am. J. Roentgenol. 97 No. 4: 1045

HENDEE, W.R. (1967)   Radiation response of LiF at low doses - note
Health Physics 13:   1235.

HEW (1976)   Publication (FDA) 76-8027 Report No. I. The
use of electron linear accelerators in
medical radiation therapy: Physical
characteristics.

HINE, G.J. (1951)   Scattering of secondary electrons produced by
γ-rays in materials of various atomic numbers.
Phys. Review 83:   755.

HINE, G.J. (1952)   Secondary electron emission and effective atomic
numbers,   Nucleonics 10:   9

HOLT, G.J., LAUGHLIN, J.S., MORONEY, J.P. (1970) The extension of
the concept of tissue-air-ratios (TAR) to
high energy x-ray beams.   Radiol. 96: 437

HOWARTH, J.L. (1951) Calculation of relative surface ionization ratio.
Brit. J. Radiol 24: 671.

HOWARTH, J.L., JONES, J.C., MILLER, H. (1951) Physical measurements on a 2 MeV x-ray generator. Brit. J. Radiol 24: 665.

HUBBELL, J.H., HAYWARD, E., TITUS, W.F. (1957) Energy and angular distribution of x-rays, scattered in lead. The Physical Review, 108: 1361

HUBBELL, J.H. (1969) Photon cross-sections, attenuation coefficients and energy absorption coefficients from 10 keV - 100 GeV. NRDS-NBS 29.

IBBOTT, G.S., HENDEE, W.R. (1970) Beam shaping platforms and the skin-sparing advantage of Co^{60} radiation. Am. J. Roentgenol., Rad. Therapy & Nuclear Med. 108: 193

ICRU (1938)   Recommendations of the International Commission on Radiological Units, Chicago, 1937. Am. J. Roentgenol, 39: 295.

ICRU (1951)   Recommendations of the International Commission on Radiological Units, London, 1950. Radiol. 56: 117.

ICRU (1954)   Report of the International Commission on Radiological Units, Copenhagen, 1953. Radiol. 63: 106.

ICRU (1957)   Report of the International Commission on Radiological Units and Measurements. NBS(U.S.) Handbook 62.

ICRU (1962)   Report 10.a. Radiation quantities and units, NBS (U.S.) Handbook 84.

ICRU (1963)   Clincial dosimetry. NBS (U.S.) Handbook 87

ICRU (1964)   Report 10b Physical aspects of irradiation. NBS (U.S.) Handbook 85

ICRU (1969)   Report 14. Radiation dosimetry: x-rays and gamma rays with maximum photon energies between 0.6 and 50 MeV.

ICRU (1974)   The new names of SI units in the field of ionizing radiations. Special Report. Radiology, 118: 233.

ICRU (1976)   Report 24. Determination of absorbed dose in a patient irradiated by beams of x or gamma rays in radiotherapy procedures.

JACKSON, W. (1971) Surface effects of high energy x-rays at
                    oblique incidence. Brit. J. Radiol. 44:
                    109.

JOHNS, H.E., EPP, E.R., CORMAC, D.V., FEDORUK, S.O., (1952)
                    Depth dose data and diaphragm design for the
                    Saskatchewan 1000 curie Cobalt Unit. Brit.
                    J. Radiol. 25: 302.

JOHNS, H.E., CUNNINGHAM, J.R. (1974) The Physics of Radiology .
                    Edited by Friedman, M. Charles C. Thomas
                    Publisher, Springfield.

KAHN, F.M., HENDEE, W.R. (1971) Use of electron filter to
                    reduce skin dose in Cobalt therapy. Am.
                    J. Roentgenol. 111: 180.

KARTHA, M., MacDONALD, J.C.F. (1971) LiF surface and depth
                    dose measurements of megavoltage photon
                    and electron beams. Acta Radiologica,
                    Therapy 10:   279.

KARZMARK, C.J., DEUBERT, A., LOEVINGER, R. (1965) Tissue-
                    phantom - ratios - an aid to treatment
                    planning (letter) Brit. J. Radiol. 38: 158.

KARZMARK, G.J., PERING, N.C. (1978) Electron linear accelerators
                    for radiation therapy: History, principles
                    and contemporary developments. Phys. Med.
                    Biol. 18:   321.

KELLER, B., MATHEWSON, C., RUBIN, P. (1974) Scattered radiation
                    dosage as a function of x-ray energy. Radiol.
                    111:   447.

KIJEWSKI, P.K., BENGT, E., BJARNGARD, E. (1978) The use of
                    computed tomography data for radiotherapy
                    dose calculations. J. Rad. Oncol. Biol.
                    Phys. 4:   429.

KNAPP, E.A. (1965) Design, construction and testing of RF structures
                    for a proton linear accelerator. IEEE Trans.,
                    NS 12. No. 3:   118.

KNAPP, E.A. (1969) Resonantly coupled standing wave accelerator
                    structures for electron and proton linac
                    applications. IEEE Transactions, N.S. 16,
                    No. 3 329.

LINAC CODE OF PRACTICE Medical Physics Vol 2, No 3, 1975.

LEUNG, P.M.K., JOHNS, H.E. (1977) Use of electron filters to improve the build-up characteristics of large fields from Cobalt-60 beams. Medical Physics Vol. 4, No. 5: 441.

LIEGNER, L.M., MICHAUD, N.J., (1961) Skin and subcutaneous reactions induced by supervoltage irradiation. Am. J. Roentgenol., Rad. Therapy & Nuclear Med. 85: 533.

LIVINGSTON, S.M. BLEWETT, J.P. (1962) Particle Accelerators. Edited by the McGraw - Hill Book Company, New York-San Francisco - Toronto-London.

MARBACH, J.R., ALMOND, P.R. (1977) Scattered photons as the cause for the observed d_{max} shift with field size in high-energy photon beams. Med. Phys. Vol. 4, No. 4: 310

McCALL, R.C., McINTYRE, R.D., TURNBULL, W.G. (1978) Improvement of linear accelerator depth - dose curves. Med. Phys. 5 No. 6: 518

MURTHY, M.S.S., LAKSHMANAN, A.R., (1976) Dose enhancement due to backscattered secondary electrons at the interface of two media. Rad. Research 67: 215.

NELMS, A.T. (1953) Graphs of the Compton energy-angle relationship and the Klein-Nishina formula from 10 keV to 500 MeV NBS Circular 543.

PODGORSAK, E.B., RAWLINSON, J.A., JOHNS, H.E. (1975) X-ray depth doses from linear accelerators in the energy range from 10 to 32 MeV. Am. J. Roentgenol. 123: 182

PURDY, J.A. (1977) Relationship between tissue-phantom ratio and percentage depth-dose. Medical Physics Vol. 4 No. 1: 67.

RAMO, S., WHINNERY, J.R. (1953) Fields and Waves in Modern Radio. Edited by John Wiley & Sons Inc., New York, Chapman & Hall Ltd., London.

RAWLINSON, J.A., JOHNSON, H.E. (1973) Percentage depth dose for high energy x-ray beams in radiotherapy. Am. J. Roentgenol., Rad. Therapy & Nuclear Med. 118: 919.

RICHARDSON, J.E., KERMAN, H.D., BRUCER, M (1954) Skin dose from a Cobalt-60 teletherapy unit. Radiol. 63:25.

SAYLOR, W.L., QUILLAN, R.M. (1971) Methods for the enhancement of skin sparing in Co^{60} teletherapy. Am. J. Roentgenol. 111: 174.

SCHULMAN, J.H. (1965) Survey of luminescence dosimetry. Proc. of International Conference on Luminescence Dosimetry, Stanford University, Stanford.

SCRIMGER, J.W. (1972) The distribution of scattered electrons from an 8 MeV linear accelerator. Radiol. 105: 421.

SCRIMGER, J.W. (1977) Backscatter from high atomic number materials in high energy Photon beams. Radiol. 124: 815.

SLATER, J.C. (1948) The design of linear accelerators. Rev. Mod. Phys. 20: 473.

STANTON, L. (1969) Basic Medical Radiation Physics. Appleton-Century-Crofts, New York

SUTHERLAND, W.H. (1975) Stability of a linear accelerator with "achromatic" electron beam bending. Brit. J. Radiol. 49: 262.

SVENSSON, H., HETTINGER, G. (1971) Dosimetric measurements at the Nordic medical accelerators. Acta Radiologica 10: 369.

TUBIANA, M., DUTREIX, J., DUTREIX, A. (1956) Dispersion des electrons secondaires mis en mouvement par des rayons-x de 22 MeV. Le Journal de Phys. et le Radium. Phys. Appl. Suppl. 3, 17: 12A-17A.

VARIAN ASSOC. (1965) Radiation Division. Report of Uranium filter.

WILSON, C.W., PERRY, B.J. (1951) Lithium Fluoride thermoluminescence dosimetry. Radiol 87: 938.

ZIMMERMAN, D.W., RHYNER, C.R., CAMERON, J.R. (1966) Thermal annealing effects on the thermolumisescence of LiF. Health Physics 13: 525.